RECENT RESEARCH ACTIVITIES

Wood species identification of ancient Japanese deity sculptures by conventional methods and synchrotron X-ray microtomography

(Laboratory of Biomass Morphogenesis and Information, RISH, Kyoto University)

Suyako Tazuru-Mizuno

In the history of Japanese sculpture, studying the image of Japanese deity sculptures is a neglected field. This is due to the small number of wooden deities remaining. In addition, since many deity images have been enshrined behind closed doors as they are considered as gods, there are fewer opportunities to investigate them in comparison to Buddhist images. Moreover, several historical facts have made it difficult to study deities, such as the god and Buddha separation and the fact that deities have a different structural progress historically compared to Buddhist images. Due to these underlying causes, a systematic approach for investigating wooden deities lags behind studies of other sculpture types. Until now, most studies have only focused on structural survey, historical consideration, and art history. Clarifying the concept of wood selection for deity sculptures would be key to solving the underlying problems in deity studies. How and why these deity sculptures came to be made with certain wood species are important issues for solving the relevance of deity sculptures and Buddhist images. Recently we shed new light on the syncretization of Shinto with Buddhism from the aspect of wood species selection. The fragments fallen and collected from deity sculptures were extremely small and their poor condition was caused by severe degradation. They were too brittle to be sectioned without embedding in resin. Therefore, together with conventional microscopic methods, synchrotron X-ray microtomography was applied.

For this method, the experimental setup of BL20XU at SPring-8 (The world's largest third-generation synchrotron radiation facility) allowed us to image any wood sample at a spatial resolution of 0.5 μm. The result showed that *Torreya nucifera* and *Chamaecyparis obtusa* were predominantly used for making deity sculptures in Shiga prefecture, Japan. In later years, most of the Buddhist images made during the Nara to Heian periods were made of *Torreya nucifera* by several researchers[1)]. Our results lead to our presumption that deity sculptures were also made by sculptors of Buddhist images at that time. Continued investigation of deity sculptures in regard to wood species has potential to reveal the linkage between Buddhism and Shinto around Heian period in Japan.

Acknowledgements

The synchrotron radiation experiments were performed at the BL20XU in SPring-8 (Japan) with the approval of the Japan Synchrotron Radiation Research Institute (JASRI) (Proposal Nos. 2007B1544, 2008B1563, 2009B1093, 2009B1981 and 2011B1239). We would like to thank Drs. Naoto Yagi, Yoshio Suzuki, Kentaro Uesugi, and Akihisa Takeuchi for conducting the experiment. We also wish to thank Shiga Prefectural Azuchi Castle Archaeological Museum for providing the samples and for their kind cooperation and suggestions.

References

[1] Kaneko H, Iwasa M, Noshiro S, Fujii T (2010) Wood types and material selection for Japanese wooden statues of the ancient period, III: Further thoughts on 8th and 9th century sculptures, MUSEUM The Bimonthly Magazine of the Tokyo National Museum, No.625, 61-78（in Japanese with English summary）

RECENT RESEARCH ACTIVITIES

Vanillin-induced cellular response in the white rot fungus, *Ceriporiopsis subvermispora*

(Laboratory of Biomass Conversion, RISH, Kyoto University)

Takahito Watanabe, Hiroshi Nishimura, and Takashi Watanabe

White-rot fungi can mineralize lignin in wood. Some of fragments generated during lignin degradation are putative signal molecules that regulate the mechanism of wood decay. In the well-known white-rot fungus, *Phanerochaete chrysosporium*, its cellular response to vanillin has been analyzed in detail [1]. Vanillin is one of the key intermediates found during lignin biodegradation. *P. chrysosporium* exposed to vanillin drastically changes the metabolic flux from the glyoxylate cycle to the tricarboxylic acid cycle and then activates the heme biosynthesis pathway. Moreover, one of the lignin-degrading enzymes, manganese peroxidase, which contains a heme, is highly expressed in the presence of vanillin. Therefore, it is likely that the effective heme biosynthetic system, branching the tricarboxylic acid cycle, contributes not only to supply a manganese peroxidase with a heme but also to promote lignin degradation in *P. chrysosporium*.

Based on these observations in *P. chrysosporium*, we now focus on the cellular response of a white-rot fungus, *Ceriporiopsis subvermispora*, to vanillin. *C. subvermispora* has very different characteristics from *P. chrysosporium*: i) selective ligninolysis without serious damage to cellulose; ii) secretion of large amounts of fatty acids and their peroxidation at an early stage of wood decay; iii) high resistance to growth inhibition by vanillin; iv) no activity of lignin peroxidase; v) possession of a suppression mechanism of cellulolytic hydroxyl radical; vi) no activity of cellobiohydrolase. Therefore, *C. subvermispora* would behave differently in response to vanillin from *P. chrysosporium*. Indeed, we have demonstrated that a gene involved in the biosynthesis of linoleic acid is inducibly transcribed in the presence of vanillin [2]. This observation is not reported in *P. chrysosporium*.

In order to investigate the cellular response of *C. subvermispora* to vanillin, we quantitatively analyzed fungal growth, glucose consumption, production of lipid-related metabolites, and activities of lignin-degrading enzymes using cells grown on a synthetic liquid medium supplemented with vanillin. Unlike *P. chrysosporium*, no growth inhibition was detected in *C. subvermispora* exposed to vanillin. The production of lipid-related metabolites was remarkably increased in culture supernatant fluid of *C. subvermispora* exposed to vanillin. Moreover, we successfully obtained many gene clones that are up-regulated in the presence of vanillin by suppression subtractive hybridization. We are now trying to predict the function of these genes using various genome databases.

Using two intracellular proteins from *C. subvermispora* grown with and without vanillin, on the other hand, we are also performing fluorescence two dimensional difference gel electrophoresis (2D-DIGE). In this method, we can co-separate and visualize two different protein samples on a single two-dimensional gel. Because the expression ratio from each of the protein spots obtained in 2D-DIGE are quantitatively calculated, we can easily select the protein spots that are positively or negatively expressed in the presence of vanillin. If 2D-DIGE works well, these proteins of interest will be identified by mass spectrometry. Furthermore, we will be able to compare the cellular response of *C. subvermispora* with that of *P. chrysosporium* against exogenous addition of vanillin.

References

[1] Shimizu, M., Yuda, N., Nakamura, T., Tanaka, H., and Wariishi. (2005) Metabolic regulation at the tricarboxylic acid and glyoxylate cycles of the lignin-degrading basidiomycete *Phanerochaete chrysosporium* against exogenous addition of vanillin. *Proteomics* **5,** 3919-3931.

[2] Watanabe, T., Tsuda, S., Nishimura, H., Honda, Y., and Watanabe, T. (2010) Characterization of a Δ12-fatty acid desaturase gene from *Ceriporiopsis subvermispora*, a selective lignin-degrading fungus. *Appl. Microbiol. Biotechnol.* **87,** 215-224.

RECENT RESEARCH ACTIVITIES

Characterization of lignocellulose in *Erianthus arundinaceus* and identification of the genes that encode antitumor lignan biosynthetic enzymes (Laboratory of Metabolic Science of Forest Plants and Microorganisms, RISH, Kyoto University)

Masaomi Yamamura, Safendrri Komara Ragamustari, Shiro Suzuki, and Toshiaki Umezawa

Wood biomass is the most abundant renewable resource on the earth, and therefore, the better utilization and efficient production of wood biomass are the key factors to establish a sustainable society. In this context, our laboratory is involved in analyzing metabolic functions of forest plants from a wide variety of aspects, including organic chemistry, biochemistry, molecular biology, and metabolomics, aiming at the elucidation of mechanisms of lignocellulose formation of biomass plants and their biotechnological application. Here we describe some of the recent research topics of our laboratory.

1. Characterization of lignocellulose in *Erianthus arundinaceus*

Lignin is a major component of the secondary cell walls of vascular plants, and an obstacle in the enzymatic saccharification of cell wall polysaccharides. *Erianthus* spp. are large gramineous plants of interest as potential feedstock. However, lignocelluloses of the species have not been chemically characterized. In this study, we analyzed lignins, related compounds, enzymatic saccharification efficiencies (ESEs), and minerals in the ash of the inner and outer parts of the internode, leaf blade, and leaf sheath of *Erianthus arundinaceus*. Lignins in the four organs consisted of guaiacyl, syringyl, and *p*-hydroxyphenyl units. The ratios of syringyl to guaiacyl lignins and lignin contents ranged from 0.43 to 0.79 and 20 to 28%, respectively, with values highest in the outer part of the internode. The amounts of ferulic acid unit were similar (7.3–11.8 mg g^{-1} dry weight of cell-wall material) in all four organs, while there was more *p*-coumaric acid units in the inner part of the internode (44.7 mg g^{-1} dry weight of cell-wall material) than in other organs (25.7–28.8 mg g^{-1} dry weight of cell-wall material). The ESE (24 h reaction time) of the leaf blade was 21.6%, while those of the other organs ranged from 10.0 to 15.2%. The inner part of the internode did not show a negative correlation between lignin contents and ESEs, suggesting that enzymatic saccharification of inner part was reduced by not only lignin but also other factors. The leaf blade had the highest ash content (17.1%); the main inorganic element was silicon. This study provides the first fundamental knowledge of *E. arundinaceus* lignins [1].

2. Identification of cDNAs that encode antitumor lignan biosynthetic enzymes

There have been a number of reports on the isolation and characterization of cDNAs encoding enzymes involved in lignan biosynthesis. In our research, we isolated and characterized three cDNAs that encode *O*-methyltransferases (OMTs), which are involved in lignan biosynthesis of *Anthriscus sylvestris* and *Forsythia koreana*. The first OMT, AsTJOMT, is responsible for the first *O*-methylation step in yatein biosynthesis from matairesinol in *A. sylvestris* [2]. Yatein is a precursor to podophyllotoxin, an aryltetralin lignan used for semi-synthesis of cancer-treating drugs. The other OMTs, each from *A. sylvestris* and *F. koreana*, catalyzed the *O*-methylation of matairesinol into arctigenin and isoarctigenin, respectively. Arctigenin is known to have high pharmacological significance such as: being a lead structure for inhibitors of human immunodeficiency virus type-1 integrase, having immunomodulatory effect on tumor necrosis factor-α and nitric oxide production, and lymphocyte production, and as an activator of AMP-activated protein kinase, which controls whole-body glucose homeostasis.

References

[1] M. Yamamura, S. Noda, T. Hattori, A. Shino, J. Kikuchi, K. Takabe, S. Tagane, M. Gau, N. Uwatoko, M. Mii, S. Suzuki, D. Shibata, T. Umezawa, "Characterization of lignocellulose of *Erianthus arundinaceus* in relation to enzymatic saccharification efficiency." *Plant Biotechnology* 30, 25-35, 2013.

[2] S. K. Ragamustari, T. Nakatsubo, T. Hattori1, E. Ono, Y. Kitamura, S. Suzuki, M. Yamamura, T. Umezawa, "A novel *O*-methyltransferase involved in the first methylation step of yatein biosynthesis in *Anthriscus sylvestris*," *Plant Biotechnology*, in press.

RECENT RESEARCH ACTIVITIES

Tissue-specific transcriptome analysis in nodules of *Lotus japonicus* identified a novel transporter, LjMATE1, that assists the Fe translocation to nodules by providing citrate

(Laboratory of Plant Gene Expression, RISH, Kyoto University)

Kojiro Takanashi, Akifumi Sugiyama, and Kazufumi Yazaki

Legume plants can establish symbiotic nitrogen fixation (SNF) in nodules as a plant-microbe collaboration, where the nutrients between host plant cells and their resident bacteria (rhizobium) are actively exchanged. As such major molecules nitrogen compounds and carbohydrates are known, while various minerals are also transported; however knowledge about the molecular basis of plant transporters mediating exchange of those metabolites is still very limited. To elucidate the metabolite dynamics relevant for SNF in nodules, three cell types were isolated from a nodule of a model legume, *Lotus japonicus*, using laser microdissesction (LM) (Figure 1), and one-color microarray analysis was done. In our cell type-specific profiling, many genes were identified as being expressed in nodules in a spatial-specific manner. For example, a number of metabolic genes for a phenylpropanoid pathway were found as being highly expressed in the nodule cortex accompanied by those encoding putative transporters for organic metabolites.

Among them, a MATE-type transporter (LjMATE1) was identified as an infection zone-specific gene. Reporter gene experiments indicated that *LjMATE1* expression was restricted to the infection zone of nodules. To characterize the transport function of LjMATE1, we conducted a biochemical analysis using *Xenopus* oocyte as a heterologous system, and found that LjMATE1 is a citrate-specific transporter. The physiological role of LjMATE1 was analyzed with *L. japonicus* RNA interference (RNAi) lines, which revealed limited growth only under nitrogen deficient conditions with inoculation of rhizobia compared with the controls. It was noteworthy that Fe localization was clearly altered in nodule tissues of knock-down line and the Fe content in nodules was significantly lower than that in wild-type. These results strongly suggest that LjMATE1 is a nodule-specific transporter that assists the Fe translocation from the root to nodules by providing citrate.

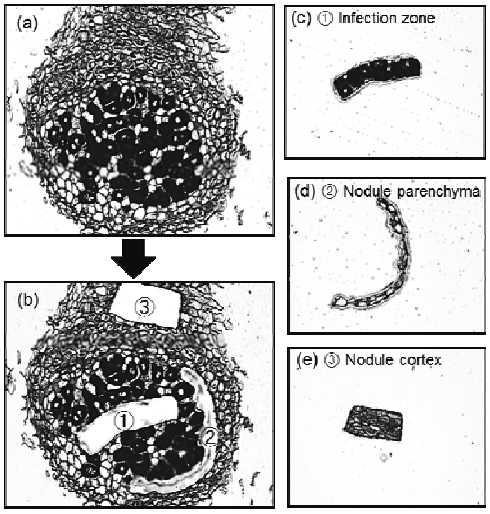

Figure 1. Isolation of three tissues from cross section of *L. japonicus* nodule using laser microdissection (LM). Cross section of a nodule; (a) before, and (b) after, LM. (c-e) Sectioned three cell-types; (c) infection zone, (d) nodule parenchyma; and (e) nodule inner cortex.

Acknowledgements

We thank Ms. H. Kamakura (The University of Tokyo, Japan) for her technical assistance in preparing LM samples, Dr. Y. Nagamura and Ms. R. Motoyama (National Institute of Agrobiological Sciences, Japan) for the microarray experiment. We thank Mrs. M. den Dulk-Ras (Leiden University, Netherlands) and Dr. T. Nakagawa for the gift of *A.rhizogenes*, and pGWB vectors, respectively. *L. japonicus* seeds were provided by the National BioResource Project.

References

[1] Takanashi K., Takahashi H., Sakurai N., Sugiyama A., Suzuki H., Shibata D., Nakazono M., Yazaki K., "Tissue-specific transcriptome analysis in nodules of *Lotus japonicus*", *Molecular Plant-Microbe Interaction*, vol. 25. pp. 869-876, 2012.

[2] Takanashi K., Yokosho K., Saeki K., Sugiyama A., Sato S., Tabata S., Ma J.F., Yazaki K., "LjMATE1 - a citrate transporter responsible for iron supply to nodule infection zone of *Lotus japonicus*", *Plant and Cell Physiology*, vol. 54. pp.585-594, 2013.

RECENT RESEARCH ACTIVITIES

Long-term Observations of Mesosphere and Lower Thermosphere (MLT) Dynamics with Meteor and Medium-frequency (MF) Radars in Indonesia

(Laboratory of Atmospheric Sensing and Diagnosis, RISH, Kyoto University)

Toshitaka Tsuda

Based on its temperature profile, the atmosphere can be separated into the troposphere (surface to 10–15 km altitude), stratosphere (10–50 km), mesosphere (50–90 km), and thermosphere (90–1,000 km), with the region above 60 km being partially ionized owing to absorption of solar radiation. The lower atmosphere is involved in various meteorological phenomena, including atmosphere–land–ocean interactions and anthropogenic effects, and global warming occurs primarily in the troposphere. Conversely, the thermosphere is the region most affected by solar activity, including 11-year solar variations and abrupt flare events. The region spanning altitudes of 60–150 km is referred to as the mesosphere–lower thermosphere (MLT); this region acts as an interface between the atmosphere near the earth's surface and interplanetary space. Moreover, a prominent change in the dominant physical and photochemical processes occurs in the MLT region, making this region of particular interest in terms of atmospheric dynamics.

We observed atmospheric dynamics in the MLT region during 1977–1990 at Shigaraki using a meteor radar, which determines wind velocity at altitudes of 80–110 km and with temporal and spatial resolutions of 1 h and 2 km, respectively. A group at the University of Adelaide in Australia operates a medium-frequency (MF) radar to observe MLT dynamics, located at conjugate point relative to the equator. We have been continuing a collaborative study with this group to investigate the behavior of atmospheric waves, atmospheric diurnal and semidiurnal tides, planetary waves, and atmospheric gravity waves. Our results demonstrate similarities and hemispheric differences in the seasonal variations of wave activity.

Radar observations have been expanded toward the tropics. In close collaboration with the Indonesian Institute of Aeronautics and Space (LAPAN), we installed meteor radars at Koto Tabang (western Sumatra), Jakarta (western Jawa), and Biak (Papua) and MF radars at Pameungpeuk (western Jawa) and Pontianak (west Kalimantan) (Fig. 1). The University of Adelaide group has operated MF radars on Christmas Island and helped to establish a number of MLT radars in India, China, and the eastern Pacific.

We used long-term continuous radar observations in 1990-2013 to analyze the characteristics of MLT dynamics. Our results demonstrate that the zonal wind exhibits a semiannual oscillation (SAO) and a westward maximum in March–April that is enhanced considerably every two or years. This peculiar phenomenon appears to be related to dynamical forcing due to breaking of atmospheric waves, tides, gravity waves, or Kelvin waves. The mean meridional wind is characterized by an annual oscillation (AO) with air flow from summer to winter hemispheres. A long-term trend in the meridional winds is also apparent and appears to be more dominant in summer at a particular station in India. However, radar results from Indonesia suggest a decadal oscillation of the meridional winds; such long-term variations may be induced by global warming and/or solar variations.

The MF/meteor radar data have been archived in a database at RISH and are available for use by any research community that may be interested in studying equatorial atmospheric dynamics.

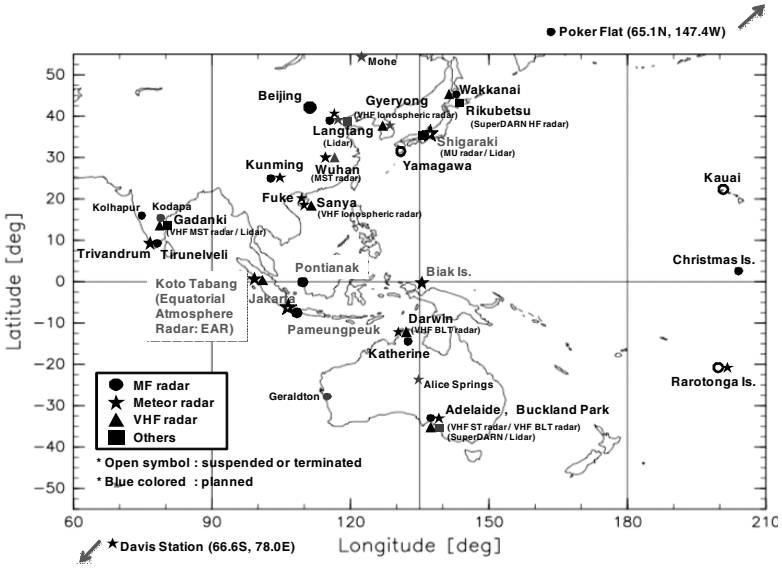

Figure 1. MLT radar network in the Asia–Oceania region

RECENT RESEARCH ACTIVITIES

Do Japanese cypress trees emit methane significantly into the atmosphere ?

(Laboratory of Atmospheric Environmental Information Analysis, RISH, Kyoto University)

Kenshi Takahashi

Recent experiments conducted by Keppler *et al*. [1] suggested that CH_4 emissions from terrestrial plants under aerobic conditions could be a significant source of atmospheric CH_4. However, since the mechanisms underlying CH_4 emission are still largely unknown, any extrapolations to the global scale are highly speculative. In Japan, artificial plantations of Japanese cypress (*Chamaecyparis obtusa* Sieb. et Zucc) cover up to 10% of the total Japanese forest area. Investigating whether *C. obtusa* emits CH_4 significantly is thus important to develop an emission inventory of CH_4 in Japan and to understand its impact on the atmospheric CH_4 budget.

In this study, we for the first time made an attempt to estimate CH_4 fluxes from intact leaves and trunk, which are rather than detached tissues, of *C. obtusa* over the whole season using an automated, closed-chamber system coupled to a laser-based instrument that allowed in situ real-time detection of CH_4 [2]. Continuous *in situ* measurements of methane (CH_4) fluxes were conducted in the Kiryu Experimental Watershed in Shiga Prefecture, from August 2009 to August 2010. The closed-chamber system, which was used to evaluate CO_2 exchange between the atmosphere and forest ecosystems, was coupled to a laser-based instrument to monitor CH_4 concentrations. Temporal changes in CH_4 concentrations from the foliage and trunk were measured at one-second intervals during chamber closure to determine CH_4 fluxes between the leaf and trunk surfaces and the atmosphere. While recent studies have suggested that some plants emit CH_4 under aerobic conditions (References are cited in [2]), emission or uptake of CH_4 in detectable amounts with our experimental system, by intact leaves or the trunk of *C. obtusa*, was not significantly observed throughout the measurement period. We note that at KEW CH_4 exchange between the atmosphere and forest has also been measuring based on a relaxed eddy accumulation technique coupled to the laser spectroscopy instrument, indicating that CH_4 emission from leaves and trunk are insignificant, as consistent with the results of the closed chamber study [3].

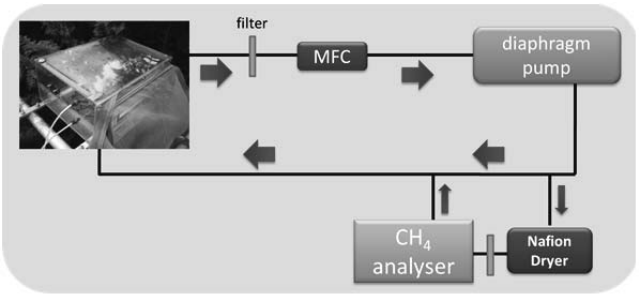

Figure 1. An automated closed chamber system for measureing the CH_4 exchange flux between plant leaves and the atmosphere.

References

[1] Keppler, F., Hamilton, J.T.G., Brass, M., Röckmann, T., "Methane emissions from terrestrial plants under aerobic conditions" *Nature, 439*, 187-191, **2006**.

[2] Takahashi, K., Kosugi, Y., Kanazawa, A. and Sakabe, A., "Automated closed-chamber measurements of methane fluxes from intact leaves and trunk of Japanese cypress" *Atmos. Environ., 51*, 329-332, **2012**.

[3] Sakabe, A., Hamotani, K., Kosugi, Y., Ueyama, M., Takahashi, K., Kanazawa, A. and Ito, M., "Measurement of methane flux over an evergreen coniferous forest canopy using a relaxed eddy accumulation system with tuneable diode laser spectroscopy detection", *Theor. Appl. Climatol*, *109*, 39-49, **2012**.

Acknowledgements

The author is grateful to Dr. Yoshiko Kosugi (Kyoto Univ.) for collaboration.

RECENT RESEARCH ACTIVITIES

Sounding Rocket/Ground-based Observation Campaign for Medium-Scale Traveling Ionospheric Disturbances (MSTID)

(Laboratory of Radar Atmospheric Science, RISH, Kyoto University)

Mamoru Yamamoto, Gopi Seemala, Tomohiro Kato, and Kornyanat Wtthanasangmechai

We have been studying ionospheric irregularities in mid-latitude region by using radars, GPS receiver network, and airglow imagers/Fabry-Perot interferometers. The mid-latitude ionosphere was considered much stable than those in the equatorial or polar region in the past, but our studies have revealed that there are much active variabilities in the region. An interesting phenomenon is medium-scale traveling ionospheric disturbance (MSTID) in the F-region. The MSTID is the wave structure with a wavelength of 100—200 km). These horizontal structures can be observed by using the total electron content (TEC) from GEONET, Japanese dense network of GPS receivers. We planned to study generation mechanism of the MSTID by the combination of sounding rockets and ground observations (Fig. 1). The experiment was just recently succeeded on July 20th, 2013. We monitored horizontal structures of the MSTID by using GPS-TEC real-time monitor system. While active MSTID region appeared over south Kyushu, Institute of Space and Aeronautical Science of JAXA (JAXA/ISAS) launched sounding rockets S-310-42 and S-520-27 from Uchinoura Space Center (USC) at 23:00 JST and 23:57 JST, respectively. Ionospheric parameters, i.e., plasma density, electric field, density fluctuations, were measured by in-situ instruments on board of the S-520-27 rocket. TMA (Tri-Methyl Aluminum) and Lithium were released from the S-31-42 and S-520-27 rockets, respectively, for measurement of the neutral winds. Their luminescent clouds were imaged from the JAXA experimental jet "Hisho" and from three ground sites. The Lithium experiment under the moonlight was the world first trial, and was successful. Both rockets transmitted dual-band beacon signal which was received at five ground sites and one boat over the sea.

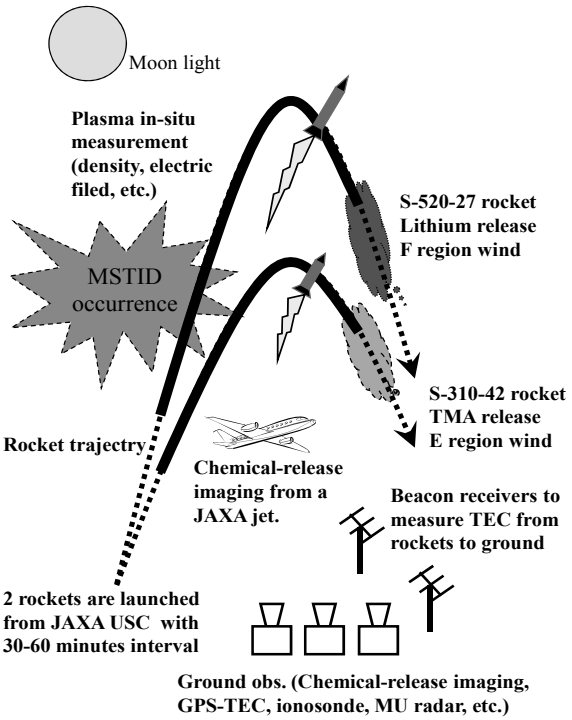

Fig. 1. Schematic of the MSTID experiment conducted on July 20th, 2013. We launched two sounding rockets from JAXA USC at 23:00 JST and 23:57 JST, respectively. All instruments on the rockets worked as scheduled. Neutral wind was measured by using the TMA and Lithium releases.

Acknowledgements

We thank all institutions that joined this experiment. They are JAXA/ISAS, Kochi Univ. of Tech., Hokkaido Univ., Toyama Pref. Univ., Tohoku Univ., Tokai Univ., Univ. of Tokyo, NICT, ENRI, Clemson Univ., and NRL. The experiment was partly supported by the Grant-in-aid for Scientific Research (B) 24340120.

RECENT RESEARCH ACTIVITIES

Preparation of tough hydrogels based on β-chitin nanofibers via NaOH treatment

(Laboratory of Active Bio-based Materials, RISH, Kyoto University)

Kentaro Abe and Hiroyuki Yano

Cellulose and chitin are some of the most abundant renewable polymers on earth. A key characteristic common to both is that they exist naturally in the form of highly crystalline nanofibers. They provide both rigid and flexible structural support in plant cell walls and in the exoskeletons of arthropods such as crustaceans and insects. Because of inferior mechanical properties such as low weight, very large surface-to-volume ratios and high aspect ratios, cellulose and chitin nanofibers have recently attracted significant interest for wide potential application in polymer reinforcement, flexible display, medical devices, separation membranes and many other areas.

The stable crystal structures in cellulose and chitin, however, prevent their molecules from dissolving in most common solvents. When hydrogels and aerogels are prepared from cellulose and chitin, for example, use of specific solvents such LiCl/DMSO and aqueous alkaline systems such as NaOH/urea (for cellulose), and calcium chloride dihydrate-saturated methanol and LiCl/NMP (for chitin) are essential. Not surprisingly, cellulose and chitin nanofibers do not dissolve in water. However, because the entanglement of their nanofibers creates a large hydrophilic surface area and high aspect ratios form a stable network in water, they are homogeneously dispersed. The result is very high viscosity, even with 1 wt% nanofiber. Their nanofibers appear to behave in water as if dissolved, maintaining good crystallinity.

In previous studies, we found that an aqueous suspension of cellulose nanofibers was easily transformed into stable and tough hydrogels through alkaline treatment [1, 2]. The nanofiber hydrogels had two different kinds of cellulose crystal forms (cellulose I and cellulose II) in response to increasing concentrations of NaOH(aq) solutions, and both gels consisted of a highly porous and crystalline nano-network. In particular, the nanofiber gel with cellulose II demonstrated high tensile strength due to the continuous and strong nano-network formed by the interdigitation of nanofibers during the mercerization process in the crystal conversion from cellulose I to cellulose II. Based on these results, the present study applied the gel preparation to chitin nanofibers. Like cellulose, the crystal structure of β-chitin is converted to α-chitin by NaOH(aq) treatment. We studied the gelation behavior of β-chitin nanofibers and investigate the physical and morphological properties of the hydrogels.

The crystal structure of chitin nanofibers (Figure 1), which were extracted from purified squid pen powder, was transformed from β-chitin to α-chitin by NaOH(aq) treatment above 30 wt%. The crystal conversion involving the interdigitation among adjacent nanofibers caused the formation of stable hydrogels with a α-chitin nanofiber network (Figure 2). The use of ethanol voided the dissolution during neutralization and enabled preparation of a highly crystalline hydrogel with high mechanical strength. It achieved a Young's modulus of 16.6 MPa, a tensile strength of 7 MPa and a strain at break of 52.2%, on average. Finally, we note that the shrinkage of the cellulose I and β-chitin nanofibers in aqueous NaOH solutions was caused by the release of residual stress due to the intracrystalline swelling in NaOH solutions.

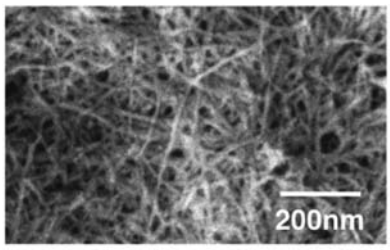

Figure 1. FE-SEM micrograph of β-chtin nanofibers.

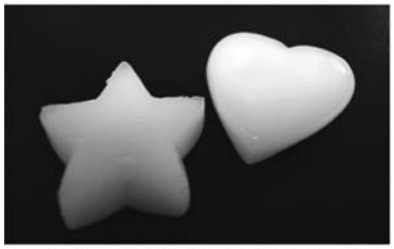
Figure 2. Chtin nanofiber-based hydrogels prepared at 35 wt% NaOH.

References

[1] Abe, K., Yano, H., "Formation of hydrogels from cellulose nanofibers", *Carbohydrate Polymers* 85, 733–737, 2011

[2] Abe, K., Yano, H., "Cellulose nanofiber-based hydrogels with high mechanical strength" *Cellulose* 19, 1907–1912, 2012

RECENT RESEARCH ACTIVITIES

Comparison of mechanical properties of wood-based materials manufactured from plantation and natural woods

(Laboratory of Sustainable Materials, RISH, Kyoto University)

Kenji Umemura and Shuichi Kawai

Recently, natural forests have been decreased significantly due to excessive deforestation. To preserve natural forests and to perform sustainable forest management, plantation forests are expanding gradually in Asia region. Broadleaf trees such as *shores spp.* have been afforested in Indonesia. Our laboratory took part in the research project which is Creation of the paradigm of sustainable use of tropical rainforest by the intensive forest management and advanced utilization of forest resources as part of Japan Science and Technology Agency Special Coordination Funds for Promoting Science and Technology (SCF) Program. In this project, we tried to compare the mechanical properties of wood-based materials manufactured from plantation and natural woods. Each *Shorea leprosulla* tree was cut down from natural and plantation forests in Indonesia. The logs were peeled out into veneers (300×300×3mm).

Manufacture and evaluation of particleboard

In case of using polymeric diphenylmethane diisocyanate (PMDI), ten percent acetone was added to the PMDI, and the solution was sprayed on to the particles at 8% solid content based on the oven-dried weight particles. The particles were mat-formed and hot-pressed at 160˚C for 10min. The size of the board was 300×300×9mm, and target density was 0.8g/cm^3. When citric acid and sucrose were used as an adhesive, both chemicals were dissolved with water at the ratio of 1 to 3. The concentration of the solution was adjusted to 59wt%, and the solution was sprayed on to the particles at 20% solid content based on the oven-dried weight particles. After mat-forming, the mat was hot pressed at 200˚C for 10min. The board size and target density were the same as described above. According to JIS A 5908 for particleboard, bending properties, internal bond strength and dimensional stability were evaluated.

Manufacture and evaluation of 3-ply plywood

Commercial PF resin with the solid content of 45.5% including some additives was applied onto both sides of the middle veneer. The spread rate was 233g/m^2 according to the instructions. The three veneers were assembled together by hand, and hot pressed at 130˚C and 1MPa for 6min. The plywood fabricated was cut into standard tensile share test specimens following Japanese Agricultural Standard (JAS). The normal and the repeated boiling tests were performed.

In case of using PMDI as an adhesive, the strength of particleboard made from natural wood was obviously higher than that of particleboard made from plantation wood. The particleboard bonded with citric acid and sucrose indicated also similar trend although whole values were low. Comparing plantation wood and natural wood in plywood, the bond strength of using natural wood was a little superior to that of using plantation wood. Judging from results obtained, it was clarified that natural wood brings rather good wood-based materials as compared with plantation wood. However, further research is necessary to clarify the differences of using plantation and natural trees.

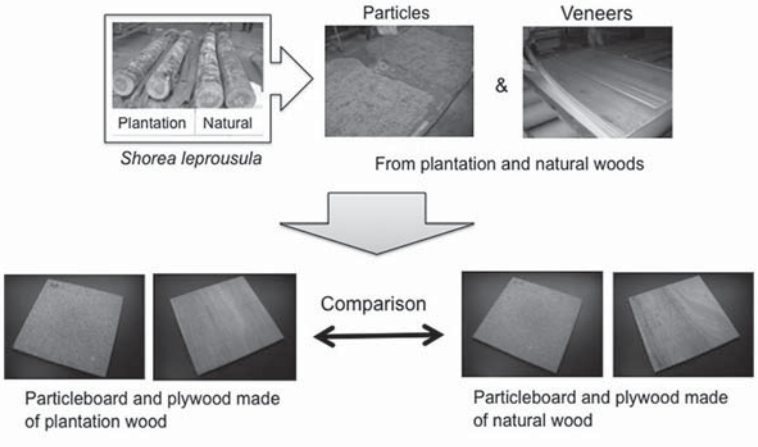

Figure 1. Scheme of experiment.

RECENT RESEARCH ACTIVITIES

Evaluation of Load-Carrying Properties of Asian Traditional Timber Structures.

(Laboratory of Structural Function, RISH, Kyoto University)

Akihisa Kitamori and Kohei Komatsu

There still exists unique and important culture of traditional timber buildings in Asian countries, including earthquake prone area like Japan. Since the viewpoints based on such culture gives important suggestions for realization of the sustainable society, it is important to preserve and inherit them. Their characteristic feature is timber frame structure, so the joints play important role to resist against earthquake attack. The load-carrying performance of joints is generally depending on the wood-to-wood interlocking without using any metal fasteners. This makes it difficult to predict their strength performance due to influence of complicated shape and enormous number of combination of different wood materials. Recently, in response to the rise of a sense of crisis to a large-scale earthquake disaster, the project which establishes the design method of tradition timber structures is advanced. For exact estimation of a proof strength of the building, the calculation formula which predicts load-displacement relations of joint is demanded. Our laboratory is doing experimental and analytical research to find solutions to evaluate the structural performance of some of main wood-to-wood joints or structural components, from the viewpoint of materials properties, the proposal of allowable strength based on mechanical model analysis to an application of the practical behavior of traditional buildings.

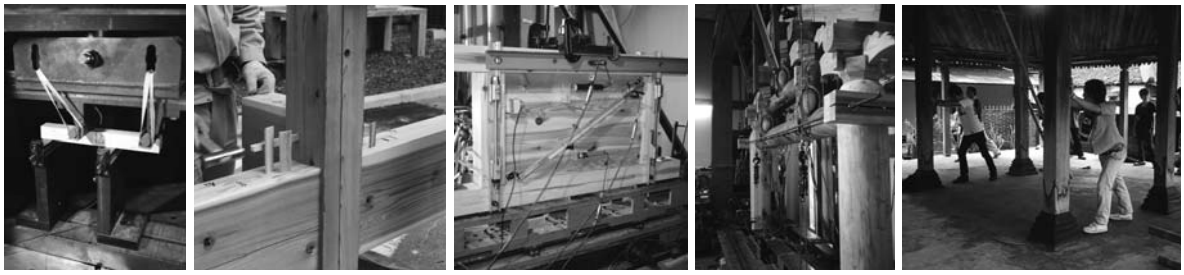

Figure 1. The photo of the experiment. From left to right: Material test of hardwood used as fasteners of the joint; Complicated Japanese traditional joint specimen; Small scaled in-plane shear test of plank shear wall with hardwood shear key; The racking strength test of Taiwanese traditional frame; In-situ measurement of dynamic vibration property of Indonesian traditional building.

Figure 2 shows an example of the comparison between estimated and experimental moment-rotation curves of one of the most popular Japanese traditional spline-shear key column to beam joint. The predicted curve was illustrated by considering two different resistance mechanisms which can be calculated from material properties and size parameters, so that the calculation formula can be applied to any different combination/size of joint. We are proposing easy design formulas for several kind of structural elements of traditional building which is composed of complicated shaped members. It is expected that this kind or research approach will contribute to the expanded possibility of timber structures.

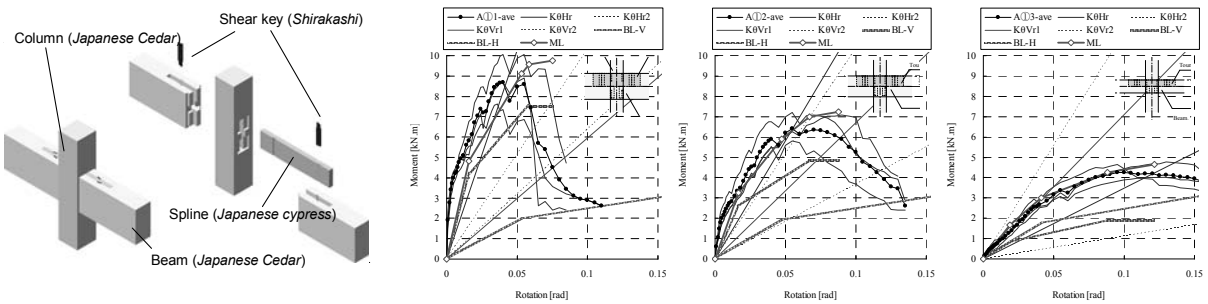

Figure 2. Comparison of experimental and estimated result of rotation property of Japanese traditional joint with spline and shear keys.

RECENT RESEARCH ACTIVITIES

Selective liquefaction of wood biomass by pulse current heating

(Laboratory of Innovative Humano-habitability, RISH, Kyoto University)

Sensho Honma, Toshimitsu Hata, Takashi Watanabe, and Tsuyoshi Yoshimura

1. Products from fast pyrolysis of wood biomass with pulse current heating

Useful products were obtained from bio-oil and char by fast pyrolysis of wood biomass. Developing technology is relevant for the effective utilization of char and for production of chemicals from bio-oil. On the other hand, shape-controlled porous carbon and catalyst carrier are interesting examples of the potential application of pulse current heating method in order to obtain value added products from residue(char) obtained by fast pyrolysis as Kurosaki reported. [1, 2]

Fast pyrolysis of wood biomass with pulse current heating was examined in order to get useful co-products from bio-oil and to know the optimum pyrolysis conditions of the compositions in bio-oil and structural properties of the co-products. The maximum yield of bio-oil was obtained at around 500ºC. GC-MS, FT-IR and elemental analysis made clear the effects of reaction temperature on mass balance, chemical structure of bio-oil compositions, the organics and ammonia adsorbed by char [3].

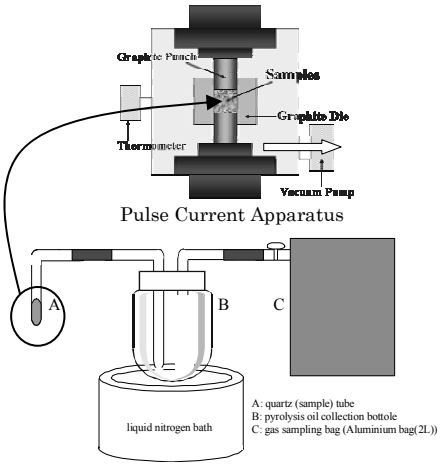

Figure 1. Aparatus and method for collection of pyrolysis products

2. Utilization of Biomass Resources by Selective Liquefaction with Pulse Current Heating Method

Pyrolysis conditions and basic components of woody biomass, plant biomass were studied. The composition of products, bio-oil and the characteristic of char were also studied. The effects of pyrolysis temperature on the compositions of products showed that the maximum yield of bio-oil was obtained at 500ºC for rice husks and at 600ºC for cellulose. The effects of pyrolysis temperature on the ammonia adsorption capacity of char was acquired. High amount of levoglucosan was contained in bio-oil at 400 - 800ºC during pyrolysis of cellulose [4].

3. Investigation of Selective Liquefaction with Pulse Current Heating for Development of Alternatives based on Renewable Resources

The influence of catalyst conditions was studied on the characteristics of char and bio-oil used in the fast pyrolysis with pulse current heating. The micro graphite layer was observed in the char on a condition in the products prepared by using catalysts. The increasing tendency was found on the composition ratio of some aromatic compounds for the bio-oil. Accordingly, catalyst used in the pyrolysis contributes to selective liquefaction and char functionalization [5].

References

[1] Kurosaki F, Koyanaka H, Hata T, Imamura Y, “Macroporous carbon prepared by flash heating of sawdust”, *Carbon* 45, 668-689, 2007

[2] Kurosaki F, Koyanaka H, Tsujimoto M, Imamura Y, “Shape-controlled multi-porous carbon with hierarchical micro-meso-macro pores synthesized by flash heating of wood biomass”, *Carbon* 46, 850-857, 2008

[3] Honma S, Hata T, Ohashi Y, Watanabe T, “Products from fast pyrolysis of wood biomass by pulse current heating”, Proceedings of 56 th Lignin Symposium, 152-153, 2011

[4] Honma S, Hata T, Marumoto S, Watanabe T, “Utilization of biomass resources by selective liquefaction with pulse current heating”, 197th Symposium on Sustainable Humanosphere, 145-156, 2012

[5] Honma S, Hata T, Watanabe T, “Investigation of selective liquefaction with pulse current heating for development of alternatives based on renewable resources”, 223rd Symposium on Sustainable Humanosphere, 169-170, 2013

RECENT RESEARCH ACTIVITIES

Simulations and Modeling of Geospace Environment

(Laboratory of Computer Space Science, RISH, Kyoto University)

Yoshiharu Omura and Yusuke Ebihara

We study space environment surrounding the Earth (geospace) using a large scale computer simulations. Concerning the generation mechanism of whistler-mode chorus emissions and triggered emissions through interaction with energetic electrons, we have confirmed the nonlinear wave growth theory and the saturation mechanism at the optimum wave amplitude [1], the nonlinear theory has also been confirmed by a recent spacecraft observation [2]. The nonlinear theory has been extended for interpretation of falling-tone emissions [3]. As a numerical model of chorus emissions, we have constructed a numerical model of a chorus emission evolving in space and time [4]. We have made a review of the theoretical achievements related to whistler-mode chorus emissions [5]. Electromagnetic Ion cyclotron (EMIC) waves also observed in the same inner magnetosphere as chorus emissions. Through interaction with energetic protons, EMIC triggered emissions are generated, inducing proton precipitation [6]. We also studied interaction of relativistic electrons with the EMIC triggered emissions, which cause very effective precipitation of relativistic electrons [7].

For the purpose of understanding the global structure and dynamics of energetic particles in geospace, we have performed a simulation of 4-dimensional Fokker-Planck equation under the time-dependent electric and magnetic fields provided by a global magnetohydrodynamics (MHD) simulation. When a substorm occurs, a stretched magnetic field line becomes dipole-like. The dipolarization does not proceed smoothly because of significant force imbalance. Consequently, the electric field oscillates with a period of 2–3 min, resulting in multiple injections of low-energy electrons (<50 keV) [8]. We have conducted all-sky auroral observation at the South Pole Station in collaboration with National Institute of Polar Research, Japan, Siena College, and National Science Foundation, USA. With numerical simulation, we found that poleward moving auroral forms that are frequently observed on the magnetically dayside can be explained by field line resonance [9]. By comparing signal from the GPS satellites and the multi-wavelength auroral images taken at the South Pole station, the GPS signal is found to undergo phase scintillation associated with auroral precipitation of hard electrons [10].

References

[1] Hikishima, M., and Y. Omura, Particle simulations of whistler-mode rising-tone emissions triggered by waves with different amplitudes, J. Geophys. Res., 117, A04226, 2012. [2] S. Kurita, Y. Katoh, Y. Omura, V. Angelopoulos, C. M. Cully, O. Le Contel,and H. Misawa, THEMIS observation of chorus elements without a gap at half the gyrofrequency, J. Geophys. Res., 117, A11223, 2012. [3] Nunn, D., and Y. Omura, A computational and theoretical analysis of falling frequency VLF emissions, J. Geophys. Res., 117, A08228, 2012. [4] Summers, D., Y. Omura, Y. Miyashita, and D.-H. Lee, Nonlinear spatio-temporal evolution of whistler mode chorus waves in Earth's inner magnetosphere, J. Geophys. Res., 117, A09206, 2012. [5] Omura Y., D. Nunn, and D. Summers, Generation processes of whistler-mode chorus emissions: Current status of nonlinear wave growth theory, AGU Monograph "Dynamics of the Earth's Radiation Belts and Inner Magnetosphere", 2012. [6] Shoji, M., and Y. Omura, Precipitation of highly energetic protons by helium branch electromagnetic ion cyclotron triggered emissions, J. Geophys. Res., 117, A12210, 2012. [7] Omura Y., and Q. Zhao, Nonlinear pitch-angle scattering of relativistic electrons by EMIC waves in the inner magnetosphere, J. Geophys. Res., 117, A08227, 2012. [8] Ebihara, Y., and T. Tanaka, Fundamental properties of substorm time energetic electrons in the inner magnetosphere, J. Geophys. Res. Space Physics, 118, 1589–1603, 2013. [9] Tanaka, Y. M., Y. Ebihara, S. Saita, A. Yoshikawa, Y. Obana, and A. T. Weatherwax Poleward moving auroral arcs observed at the South Pole Station and the interpretation by field line resonances J. Geophys. Res., 117, A09305, 2012. [10] Kinrade, J., C. N. Mitchell, N. D. Smith, Y. Ebihara, A. T. Weatherwax, and G. S. Bust, GPS phase scintillation associated with optical auroral emissions: First statistical results from the geographic South Pole, J. Geophys. Res. Space Physics, 118, 2490–2502, 2013.

RECENT RESEARCH ACTIVITIES

Development of a Wideband Electromagnetic Irradiation Applicator for Chemical Processing

(Laboratory of Applied Radio Engineering for Humanosphere, RISH, Kyoto University)

Tomohiko Mitani and Naoki Shinohara

Microwave heating has been attracting attention from the viewpoint of rapid, efficient and selective chemical reaction. Microwave absorption rate of a material depends on its structure, temperature, and microwave frequency. However almost all the microwave chemical processing experiments were conducted at the frequency band of 2.45 GHz, which is legally allocated for microwave heating as one of ISM (Industrial, Scientific and Medical) bands. The objective of the present study is development of an electromagnetic irradiation applicator which makes various types of chemical processing effective in not only the ISM band but also a wide frequency band.

Figure 1 shows our developed applicator. Electromagnetic waves propagate from the coaxial connector at the input port through the applicator using coaxial cable structure. The coaxial cable does not limit the irradiation frequency theoretically. Distilled water is poured into the applicator as reference. Teflon is installed to prevent the water from leaking. Tapering structure plays an important role in reducing reflection of electromagnetic waves at the boundary between the water and Teflon. There is a punching metal on the end plate of the applicator to relieve pressure without leaking electromagnetic waves.

We conducted numerical simulation by using 3D electromagnetic simulator, and practical experiments, as shown on the left-hand and right-hand sides of Figure 1, respectively. The experimental results were well matched to the numerical simulation results. We successfully developed the applicator with a low reflection rate of less than 10 % from 1.2 GHz to 2.7 GHz. We will conduct chemical processing by electromagnetic irradiation using the developed applicator at various frequencies as future works.

Acknowledgements

This work is supported by JST, CREST. We deeply thank Mr. Yoshihiro Nozaki and Mr. Tsukasa Chikata, Japan Chemical Engineering & Machinery Co., Ltd., for manufacturing the applicator. Also we sincerely appreciate Professor Takashi Watanabe, the leader of the CREST project.

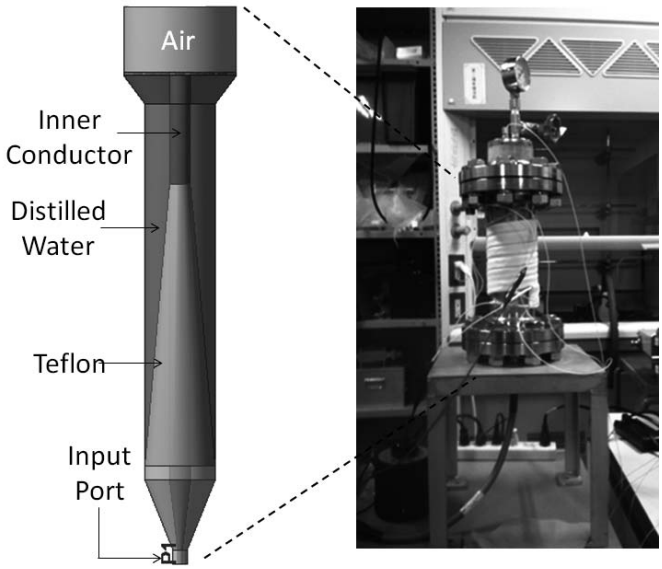

Figure 1. A conceptual image (left) and a photograph (right) of a wideband electromagnetic irradiation applicator.

RECENT RESEARCH ACTIVITIES

Novel Space Environment Monitor, Instrument, and Space Mission Concepts

(Laboratory of Space Systems and Astronautics, RISH, Kyoto University)

Hiroshi Yamakawa, Hirotsugu Kojima, and Yoshikatsu Ueda

Lorentz Force Spacecraft Formation Dynamics

Dynamics and control aspects of a charged satellite using the Lorentz force were investigated. The concept of the Lorentz-augmented charged satellite realizes propellant-less electromagnetic propulsion, using the interaction between an electro-statically charged satellite and the Earth's magnetic field. Charging of satellites can be controlled by devices like ion or electron gun. The devices are smaller and lighter than conventional chemical thrusters and suitable to be carried by small-size satellites. We investigated relative dynamics of two satellites orbiting around the Earth. One is a non-charged satellite called a target satellite, and the other is a charged satellite located near the target satellite on a circular orbit. We studied the effect of the Lorentz force on the relative motion of the chaser satellite with respect to the target satellite on an elliptic orbit or on a circular orbit as a special case.

Magneto-Plasma Sail (MPS) Space Propulsion System

An MPS (Magneto-Plasma Sail) is a unique propulsion system, which travels through interplanetary space by capturing the energy of the solar wind, which inflates a weak original magnetic field made by a super-conducting coil of about 2-10 m in diameter with an assistance of a high-density plasma jet. From our theoretical estimations, momentum transfer from the solar wind to a spacecraft with a coil is large enough if the plasma source is operated to inflate only the magnetic field away from the spacecraft. Our activities in 2006 are as follows: (a) Sizing (mass, dimension, current, etc.) of the super-conducting coil to produce magnetic field around the spacecraft, (b) Preparation of the experiment facility to measure magnetic field, temperature, current etc. around super-conducting coil.

Miniaturization of plasma wave receiver system

To meet the recent requirements on the size, mass and power budgets in constellation missions or planetary missions, the miniaturization of plasma wave receiver is inevitable. The attempt to realize the extremely miniaturized plasma wave receiver have been made using analogue ASIC technology in the lab. The main activity in 2012 is the success in the development of the tiny waveform capture receiver, which is one of the typical types of plasma wave receivers. The size of the developed tiny waveform receiver is about one tenth of the conventional waveform receiver. Moreover, we also succeeded in implementing the preamplifier and the calibration system on the same analogue chip of the waveform receiver.

Use of water containing ultrafine bubbles for remediation of radioactive contamination and in horticultural applications

Recently, ultrafine bubbles (UFBs) have found applications in various fields. We have reported the effectiveness of water containing UFBs (UFB water) of approximately 100 nm diameter for removal of radioactive cesium from soil and gravel conglomerate and nonwoven cotton. In Fukushima, this method of radioactive contamination removal using UFB water is currently under trial. We also investigated the UFB water for its ability to retain freshness and for its coloring effect on cut flowers such as a gentian. The detailed mechanism underlying the performance of UFB in the above-mentioned application is yet not well understood, although the relevance of ions (proton (H^+) and hydroxide (OH^-) ion) in solution has already been discussed by many researchers. Therefore, we are investigating the mechanism underlying the performance of UFB water through electrochemical measurements.

ABSTRACTS (PH D THESIS)

Study on Accurate Ranging and Positioning System with UWB-IR Technology

**(Graduate School of Engineering,
Laboratory of Space Systems and Astronautics, RISH, Kyoto University)**

Ryosuke Fujiwara

In this work, a low-power UWB-IR transceivers for wireless sensor networks as well as wireless positioning systems were developed.

We first explained conventional positioning methods with radio signals in Chapter 2, followed by presentation of the proposed TOA/TDOA hybrid relative positioning system based on UWB-IR technology. The proposed system design reduces the complexity of the system infrastructure when compared to the conventional TDOA systems and also reduces the number of wireless transmissions in a positioning sequence compared to conventional TOA systems. In particular, the proposed method eliminates the need for accurate synchronization among the APs and the target nodes. Additionally, it enables node-position detections with less number of access points compared to the conventional methods leading to low communication overhead at the target nodes. Through computer simulations, we confirmed that the proposed method can achieve better performance compared to the conventional TOA method with the same number of transmissions from the target node. These results validate that the proposed TOA/TDOA hybrid relative positioning system can detect the position of the target nodes with a better accuracy compared to the conventional TOA systems and with less access points compared to the conventional TDOA systems.

In Chapter 3, a novel design of the impulse-based DS-UWB system for low-power wireless applications such as wireless sensor networks was discussed. The proposed system is based on direct-sequence impulse radio with low duty cycle that enables energy efficient precise positioning. We propose several schemes in order to realize a low-cost and low-power coherent-based UWB-IR transceiver with features such as differential encoding, 2-step spreading at the transmitter, PRF sampling and initial acquisition with a combination of a serial search method and a MF method at the receiver. This system has potential to realize a lower-power transceiver LSI by reducing the sampling rate and the complexity of the digital signal processing. Towards the end of this chapter, we showed link budget calculation to conclude that our proposed system can provide enough performance for long range communications.

Chapter 4 discussed detailed system specifications of the proposed system along with simulation as well as measurement results. First of all, we investigated the permissible implementation loss of each block by considering deteriorating factors of the receiver. As a result, we found out that the total implementation loss can be within the link margin of 10.7 dB. We then performed computer simulations in which all the deteriorating factors were incorporated. The results showed that the target performance was satisfied even in the worst case conditions.

Finally, we developed a test bed and confirmed that our developed system satisfied the target performance of 250-kbps and 30-m communication. As the conclusion of this investigation, the experimental results support the feasibility of our proposed system, which has a potential to realize a lower power transceiver LSI and precise positioning systems.

Chapter 5 explained the developed UWB-IR receiver with an accurate TOA measurement capability for ranging/positioning systems for wireless sensor network applications. The developed system provides a simple architecture for coherent-based receivers and was designed to allow for transceiver implementation in a general 0.18-micrometer CMOS technology. For a rapid initial acquisition and low complexity of the coherent-based receiver, a combination of the serial search method with multiple-step search for the pulse-synchronization and the matched filter method for the code-synchronization was proposed. Furthermore, a first-path-detection algorithm that enables accurate measurements of the arrival time of the first-path signal in a multipath environment was presented. This algorithm also utilizes a combination of the serial search method for the pulse synchronization and the characteristics of the matched filters for the code synchronization as well as the initial acquisition scheme discussed above. The proposed approach can reduce both the speed of analog digital converters in the receiver and the amount of memory required to estimate received waveforms for the first-path detection.

Furthermore, the proposed system allows 20-ppm frequency error of transceiver's clocks by utilizing a

characteristic of coherent-based transceivers. These features enable a ranging-capable transceiver with simple, low-power, and low-cost implementation.

Furthermore, full UWB transceiver chips and modules for ranging and positioning systems with the proposed algorithms were developed. A highly-precise ranging system with the developed modules was set up and used to test the proposed algorithm. The experimental results verified that (i) the proposed algorithm achieves ranging accuracy of 18.5 cm on an average in a closed space, and (ii) the developed transceiver has a good enough receiver sensitivity to enable 30-m distance communications. These performances are thought to be sufficient enough for systems used in real sensor network applications.

Finally, the TOA/TDOA hybrid relative positioning system based on UWB-IR technology was developed. As discussed in Chapter 2, the system reduces the complexity of the system infrastructure compared to conventional TDOA systems, and reduces the number of wireless transmissions in a positioning sequence compared to conventional TOA systems. In particular, the system can eliminate the need of accurate synchronization among the APs and the target nodes. The proposed system was then implemented with the developed UWB transceivers. The measurement results cofirmed that the developed TOA/TDOA hybrid system can detect the relative positions of target nodes with a measured-distance accuracy of 0.31 m and a measured-angle accuracy of 8.6 degrees under the condition that the distance between two APs are 4 m. It also achieves a measured-distance accuracy of 0.18 m and a measured-angle accuracy of 16.2 degrees under the condition that the distance between two APs is 1 m. These results support that the developed system has positioning capability even when the distance between APs is shorter than the distance from the APs to the target node.

The presented research and development work is one of the earliest work in the world which realizes UWB-IR ranging/positioning systems with in-house single-chip UWB-IR transceivers in CMOS technology. We believe this research work can be a promising solution for realizing current and future ubiquitous societies.

ABSTRACTS (PH D THESIS)

Miniaturization and Integration of Measurement Systems for Space Electromagnetic Environments

**(Graduate School of Engineering,
Laboratory of Space Systems and Astronautics, RISH, Kyoto University)**

Hajime Fukuhara

Our exploitation of space is increasing and space systems such as GPS and climate satellites have become indispensable in our lives. It is hence very important to understand physical phenomena that occur in space. Space is filled with collisionless plasmas generated by the solar wind and the ionized upper atmosphere. The interaction between the solar wind and the Earth's magnetism forms the region called the magnetosphere. Space plasmas show different characteristics in the solar wind and the magnetosphere. The magnetosphere is divided into several regions depending on the plasmas' characteristics. The radiation belt region is the part of the magnetosphere that lies typically at geocentric distances of around 2 to 4 Earth radii. Highly energetic plasmas of protons and electrons exist in the radiation belts and can negatively influence space systems and human health. However, the mechanism of the generation and disappearance of the radiation belts is not yet clearly understood.

Plasma waves are an important physical phenomenon for understanding the behavior of space plasmas since the kinetic energy of the plasmas is transferred through the plasma waves. The phase of a plasma wave is related to the plasma's velocities and is important in the interaction between plasma waves and particles. The present thesis focuses on instruments for investigating plasma waves and wave--particle interactions.

A plasma wave consists of only an electric field or electromagnetic field. Sensors for plasma waves include dipole antennas for the electric field components and search coils or loop antennas for the magnetic field. The signals detected by the sensors are input to the electronics of the receiver for signal processing and data transmission through the telemetry. The electronics of the plasma wave receiver has been highly integrated and miniaturized by replacing analog components with digital hardware and software. This has been very effective for integration, though there is a trade-off between power consumption and processing speed. However, analog electronics are still used at the front-end of the receiver due to high performance requirements i.e., low noise, high sensitivity, wide-dynamic range, and wide-band frequency. Recently, multiple exploration missions have been planned and high performance miniaturized analog electronics would greatly benefit these missions.

In this thesis, the analog electronics for plasma wave observations are developed with application specific integrated circuit (ASIC) technology in order to greatly reduce the size and mass of the instruments. A plasma wave receiver can be either a waveform receiver or a spectrum analyzer. A waveform receiver observes instant electric and magnetic fields while a spectrum analyzer provides the time evolution of the intensity in each frequency band. Only a waveform receiver contains phase information of the plasma waves. The target components for miniaturization of the waveform receiver are a band-limiting filter, a variable gain differential amplifier with low, medium, and high gains, and an anti-aliasing filter. The Gm-C filter is a commonly used active filter for communication front-end with low noise and can be applied to the band-limiting filter. A multi-gain differential amplifier is realized with switching resistors to obtain each appropriate gain. Since the anti-aliasing filter must be manufactured accurately, a switched capacitor filter is suitable. However, extra Gm-C filters are necessary in the front and back of the switched capacitor for noise elimination. The spectrum analyzer has an advantage in that it can provide an overview of plasma waves and their variations. The sweep frequency analyzer (SFA) is one type of spectrum analyzer which sweeps the observation frequency range finely. The SFA has poor time resolution and fine frequency resolution. The target SFA in the present thesis has an improved time resolution without losing frequency resolution. The SFA is a double super heterodyne receiver. Because of frequency conversion, unnecessary signals at image frequency is to be rejected. Thus, a frequency synthesizer, mixer, and band pass filter must be developed for the ASIC. These circuits for both receivers are tested after manufacturing and their

feasibility is evaluated.

The developed components are integrated into one chip. For the waveform receiver, a six-channel circuit of filters and amplifiers is laid on the chip. After the layout design, the chips are manufactured using the TSMC 0.25μ CMOS process. A circuit board is also designed for mounting the chip. A power supply, clock generator, divider, and six A/D converters are implemented on the circuit board. The area of the analog components is reduced to a twentieth the size of previously developed instruments.

Applications using the miniaturized plasma wave receiver are proposed. A sensor network for plasma wave observation is introduced, consisting of a distribution of several sensor nodes with small plasma wave receivers where observation data are collected at each node. This application can obtain the spatial distribution of plasma waves. The second application consists of a constellation of satellites, used to determine the position of the plasmapause with Faraday rotation. One satellite in the constellation actively emits radio waves of linear polarization. The other satellites receive the emitted radio waves with small wave receivers and detect the variation of the polarization direction from the expected value. The principle and system design of the satellites are discussed.

Moreover, a direct measurement system for energy transfer between plasmas and plasma waves is presented. The calibration of the waveform data and time correction for synchronization of the particle data with the waveform are described. The one-chip system is realized in the FPGA with real-time processing.

ABSTRACTS (PH D THESIS)

Earthquake Resisting Timber Structure System Composed of Indonesian Engineered Wood Products

(Graduate School of Agriculture, Laboratory of Structural Function, RISH, Kyoto University)

Maryoko Hadi

Some special considerations need to be taken care of when designing earthquake-resistant houses for low-income people in Indonesia. When designing tough and ductile earthquake-resisting houses, it is important to pay attention to construction cost low so that the local people could afford to purchase.

Prediction of Nonlinear Cyclic Behaviors of Shear Wall Composed of Fast Growing Tree Framing and Fiber Cement Board Sheathing

Research on the use of engineered wood product frame as a structural element, and Fiber Cement Board (FCB)-cum-steel nail as sheathing materials for a typical Indonesia house type has been made. A general calculation method for estimating shear performance of nailed on sheathing shear walls has derived. Hence, existing design formula developed for ordinary shear walls with regular nailing patterns cannot be applied in this case. Thus, in order to predict the total behavior of shear walls with nailing patterns either V-shape or arbitrary, modification of existing formula was necessary.

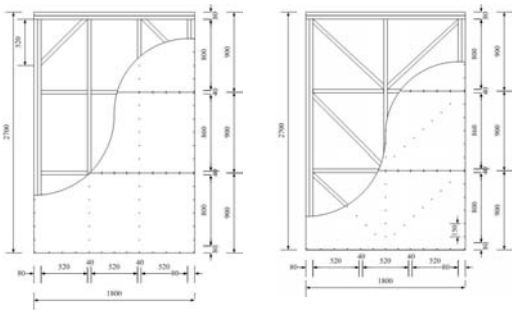

Fig. 1. Conventional shear wall frame (SWC) and Braced Shear wall frame (SWB) specimens.

In addition to this, consideration on the nonlinearity due to elasto-plastic characteristics of steel nails is also important. A step-by-step calculation method for predicting shear performance of shear walls with arbitrary nailing patterns was derived. This is followed to looking for the Normalized Characteristic Loop (NCL) model from the experiment (Fig.1) results obtained from the cyclic static test of the shear walls.

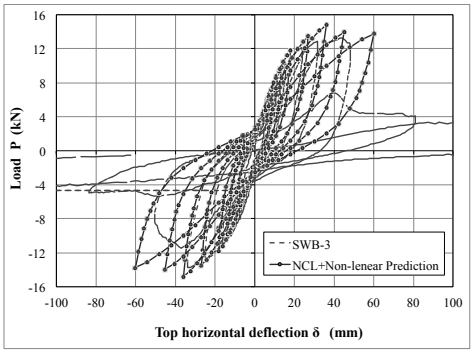

Fig. 2. Comparison between predicted load deformation curve and experimental ones for SWB specimen.

These comparisons (Fig.2) might suggest that better prediction will be obtain by paying careful attention to nail shear data to be reflected by insufficient edge distance effect.

Dynamic and Static Behaviors of Shear Wall with Openings Composed of LVL and Fiber Cement Board Sheathing

It is also worth noting on the influence of the openings has on a shear wall. To determine the trends in the behavior of shear walls with and without openings, theoretical and experimental studies are conducted through the implementation of cyclic static testing. In this study, as regular nailing pattern was used, hence equations for ordinary design calculations were applied to predict the behavior of shear walls with or without opening when subjected to horizontal push-pull static cyclic load. Shear wall specimen shown in Fig 3.

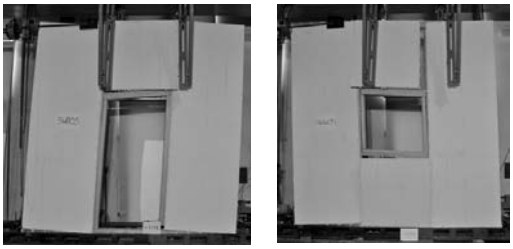

Fig. 3. Door (SWDOS) and window (SWWOS) opening of shear wall specimens.

ABSTRACTS (PH D THESIS)

All of the specimen test results show a reduction trend in the maximum load that reached by the specimen SWS, SWWOS and SWDOS (Fig. 4.). This happens due to the reducing of the sheathed area of shear wall that significantly contribute to the rigidity level.

Dynamic tests using a small shake excitation machine were also carried out to obtain the relationship between the initial stiffness and natural periods of the shear walls. The natural frequency of wall-type specimens was 4.31 Hz and it was the highest among three specimens as expected. The natural frequency of window-type was 3.86 Hz, it was middle among three, that of door-type was 3.14 Hz, and it was the lowest as expected.

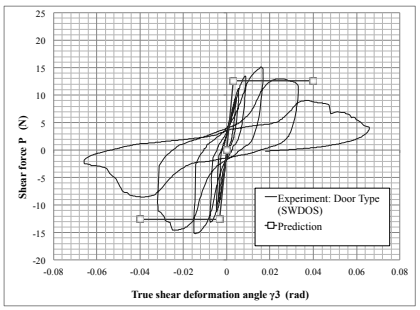

Fig. 4. Comparison between calculation and experimental result on door type (SWDOS)

Performance of Shear Wall Composed of LVL and Cement Fiber Board Sheathing

In order to find out whether the strength performance of a simple 3-D test specimen (design based on ordinary design procedure) could meet with the Indonesian standard requirement, both theoretical and experimental studies on a full-size earthquake-resisting house were studied. Comparisons between experimental result and calculated result showed that the mechanical model developed in this study could predict not only the stiffness of the system but also the yielding strength of the simple 3-D test specimen (Fig 5.)

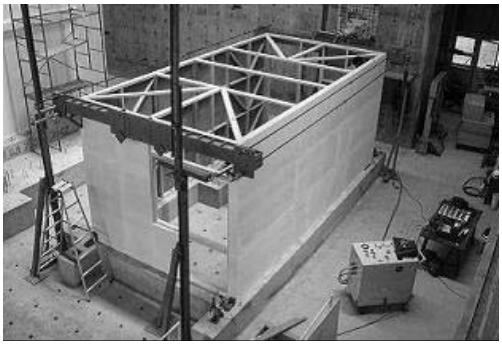

Fig. 5. The Full-scale 3-D specimens for destructive test.

Fig. 6. shows the capacity of the structures and comparisons between the observed load-deformation angle relationship of the 3-D specimen and that predicted by the theoretical models derived previously. The dot-dash line in Fig. 6. indicates the calculated stiffness and yielding load of the sheathing panel predicted by derived equations. The continuous line with diamonds ends indicates the predicted stiffness of the bracing system, which was result from the 2-D FEM analysis. The bold continuous line with triangle ends indicates the total predicted stiffness and the yielding load by summing up two individual components.

In Fig. 6., the horizontal bold line indicates the design value calculated using the Indonesian standard. (Ministry of public works of Indonesia, 2002) Comparing the ultimate strength with the required strength reveals that the safety factor is almost three, this is to be satisfactory for Indonesian standards.

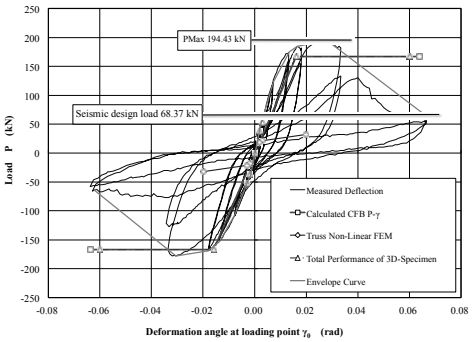

Fig. 6. The comparison between envelope curve and prediction.

Acknowledgements

This study was funded by JSPS Ronpaku, Ph.D. Program 2008-2012, and all activities were done in RISH, Kyoto University, Japan and in Research Institute for Human Settlements, Research and Development Agency, Ministry of Public Works, Indonesia.

ABSTRACTS (PH D THESIS)

Satisficing Nonlinear Spacecraft Rendezvous Under Control Magnitude and Direction Constraints

**(Graduate School of Engineering,
Laboratory of Space Systems and Astronautics, RISH, Kyoto University)**

Shinji Mitani

We treated the satellite formation and reconfiguration problem subject to constraints on control magnitude and direction. Firstly, the necessary condition of the optimal controller under these constraints was derived using a sequential smoothing method, in which a sequence of unconstrained optimal control problems was solved according to Pontryagin's Minimum Principle by introducing multiple barrier functions to the original performance index. By introducing the proposed additional barrier function concerning the constraints on control direction, the derived equations for the necessary condition with respect to optimal control magnitude and direction became decoupled, thereby facilitating their solution. The solutions converged toward solving the original problem and strictly satisfied the treated constraints as the perturbation coefficients of the barrier functions approached zero. Optimal controllers were successfully formulated in the $L1$- and $L2$-norm problems, and both solutions for the optimal control direction had the same form. These solutions are a natural extension of the solution with only the magnitude constraint. As the perturbation coefficients of the barrier functions approach zero, the smoothed optimal controller approaches the boundary of the inequality constraint near Lawden's primer vector, while the control, the primer, and the admissible direction vectors are coplanar. This extremal property is completely consistent with the result whereby the optimal thrust is directed along the projection of the primer vector onto the boundary of the restricting set. Numerical simulations demonstrated that the sequential optimal controller subject to such mixed constraint was obtained by solving the two-point boundary value problem with the shooting method in non-coplanar circular and coplanar eccentric orbits. In addition, the control angles of the derived solutions were confirmed as suppressed within the control direction constraint.

Secondly, we examined how to maintain a small-magnitude thrust angle based on continuous optimal feedback control for the problem of satellite rendezvous. Consider-ing the constraints on the parameters set in the general quadratic performance index, a control design process was proposed using modal analysis to make the thrust angle small at the initial and final phases. Using a candidate control Lyapunov function (CLF) by solving the Riccati equation for the performance index considered, a new control applying the satisficing method was devised to meet the constraints strictly from start to finish. If the limitation angle is small, the devised control may become null transiently because the candidate CLF is not strictly defined. However, this paper showed that thrust angle can be practically maintained and that the control law leads to convergence at the origin in some simulations. Extending the theory to an eccentric orbit and time-varying system was explained and numerical calculations showed effectiveness.

Although the application of two-dimensional plane motion was discussed, this technique can be extended to the design method, including out-of-plane motion. This method can also be applied to nonlinear control problems and extended to multiple control constraints, such as sensor field of view sun direction. In addition, we took steps to improve satisficing theory under input constraint. A constraint-satisficing scheme was newly proposed by introducing two barrier functions and it was shown that when the positive coefficients of both barrier functions approach zero, the constraint-satisficing set smoothly attained the intersection of the unconstrained satisficing and input constraint sets. A simple and effective nonlinear controller was proposed with the projected control as member of the constraintsatisficing set. By adopting the value function in the constraint-free case as a constraint control Lyapunov function, and choosing appropriate weight matrix parameters, the state trajectory converged to the origin; strictly satisfying the input constraint in the final phase. For the proposed controller, linearized stability analysis was investigated using a graphical description plot used to assist in designing certain practical rendezvous trajectories. It was found that when starting periodic orbit, the local subspace was widely covered by the region of attraction, provided highly

damped modes were stable.

Although the effectiveness of the proposed design was verified in the nonlinear affine system, the same satisficing approach can be easily extended to a time-varying system when the target orbit is elliptic.

ABSTRACTS (PH D THESIS)

Application of axial performance of pulled-out screw for joint of wooden structure

(Graduate School of Agriculture, Laboratory of Structural Function, RISH, Kyoto University)

Satoru Murakami

A screw is one of the most used fasteners in wooden structure recently. Since the joint with screws has high joint performance and is easy to be dismantled and repaired, it attracts timber engineers' attentions. Especially, nowadays, by using screws improved on its thread shape and size for higher shear and pull-out performance, many joint methods have been developed. However, the performance of the stiffness, maximum strength and failure property of the joint changes variously by not only the shape or number of fasteners, but also the cross-section of a wooden member where the load is applied and the shape of steel plates used around the fasteners. The structural design method corresponding to these conditions has not been established at present. The relationship between the load and displacement of pull-out screw is essential factor to establish the design method, however, it has not been explained well yet. So the design equations are inadequate.

The shear and pull-out performance of the screw have not been evaluated by accounting the shape and diameter of the screw. There are not the suitable equations of stiffness and strength corresponding to the case that the screw with any shape was pulled out from the wood member. Therefore, aiming to apply screws into the joint of the wooden structure more easily, the quantitative evaluation of the screw performance had been conducted in this study considering the case they are sheared or pulled-out. And as an application, the evaluation method for the joints of the wooden structure with screw was established.

As the first step of analysis, estimation by the finite element method (hereinafter called "FEM") was conducted to compare with the experimental results. Fig.1 shows the elastic FEM model for pull-out tests of screws, which was inserted into perpendicular to the grain of wood. The stiffness of the results of FEM were much higher than that of the experimental results. The peculiar deformation of wood under contacting surface with screws was considered as reason. Therefore, the surface deformation was evaluated by the compression tests in the direction of perpendicular to the grain of wood. The surface deformation is quantitatively derived from the difference between the apparent young's modulus obtained from the total strain and the true young's modulus obtained from the strain gage put at the center of the wood surface. By combining the deformation with the result of FEM, the stiffness of the test result was expressed well.

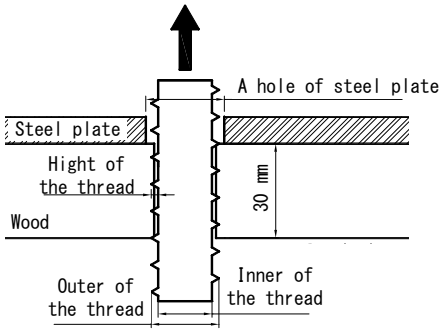

Fig. 1 Outline of test of pull-out screw

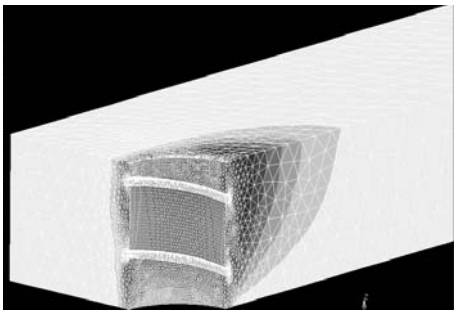

Fig. 2 Deformation distributions in radial direction in FEM

The calculated yield strength derived from the design method on the yield strength by Madsen [1] and Embedment Theory [2] showed good accordance with the test results of the pull-out tests. Therefore it was concluded that the yield strength can be decided by the projected area of the thread, the interval of the thread and the embedment-yield stress of the wood. The maximum strength could be estimated by the reduction of the multiplication of the shear area by shear strength. It was suggested that the ultimate displacement is equal with the interval of the screw thread.

As the next step, by using the characteristic values of pull-out performances of the screw, the method to improve the compression performance in the direction of perpendicular to the grain of the wood was

investigated. Here, the pull-out performances of the screws was regarded as the push-in performance of them. It was considered that the screws can reinforce wood by embedding together. Fig.3 shows the models of the area where the screws are to be inserted. The performance of the joint on the wooden structure becomes much higher by improving embedment performance. It is because that the strength of the joint is decided by the wood deformation perpendicular to the grain. The equations to predict the reinforcement effect of a screw were derived. Then, the performance of the joint was predicted. The predicted results showed good agreements with the experimental results as shown in [3] and [4].

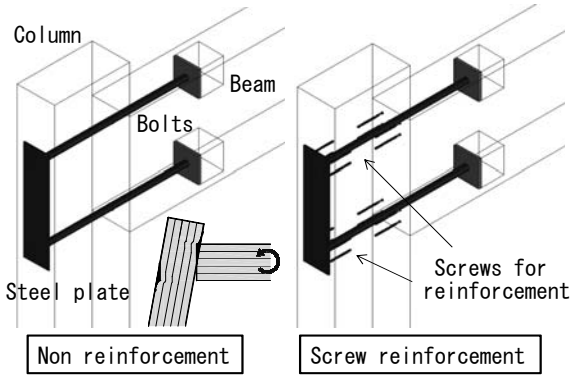

Fig. 3 The models of area where the screws are to be inserted

Finally, by taking the equation of the pull-out screw mentioned above into considerations, the performance of the screw deformed in the wood by shear force was estimated until reaching at the maximum strength. Thus, the performance of structural components of the building such as shear wall is also predicted by using the equation. Fig.4 shows a single-braced shear wall system composed of the joint with the screws. To improve the performance of the end joint of the brace, thick and short screws were effective in terms of transmitting the force into brace-steel-plate. The shear performance of the developed brace system was improved in both loading directions. Consequently, the shear wall showed 3.5 and 3.8 of the shear resistance factor against compression and tension force respectively as indicated in [5].

Fig. 4 Appearance of Shear wall test and its joint

The above-mentioned findings caused not only the improvement of the reliability on the design of the joints with the screws, but also the significant information to promote the more desirable joints.

References

[1] B. Madsen, R. F. Hooley and C.P. Hall, "A design method for bearing stresses in wood", *Canadian J of Civil Engineering*, Vol. 9, 338-349, 1982

[2] A. Kitamori, K. Jung, Y. Kataoka and K. Komatsu, "Effect of Additional Length on Partial Compression Perpendicular to the Grain of Wood: Difference among the Supporting Conditions," *Journal of Structural and Construction Engineering*, Vol. 74, No. 642, 1477- 1485, 2009 (In Japanese)

[3] S. Murakami, A. Kitamori, K. Jung, I. B. Hassel, K. Komatsu, "Evaluation of Screw Reinforcement on Bearing Performance of Wood Depending on Screw Position", *OJCE*, Vol 2, No.3, 160-166, 2012, DOI: 10.4236/ojce.2012.23021

[4] S. Murakami, A. Kitamori, K. Jung, W. Chang, K. Komatsu, "Prediction of Reinforcement Effect by Screw on Triangular Embedment Perpendicular to the Grain with Variation of Screw Locations", *OJCE*, Vol 2, No.3, 167-173, 2012, DOI: 10.4236/ojce.2012.23022,

[5] S. Murakami, T. Tamaoka, H. Kadowaki, K. Komatsu, "Improvement of Single-braced shear wall system having the same performance for push and pull load", *AIJ journal of technology and design*, Vol. 30, 421-426, 2009 (In Japanese).

ABSTRACTS (PH D THESIS)

Variability in the temperature structure around the tropical tropopause and its relationship with convective activity

(Graduate School of Science, Laboratory of Atmospheric Environment Information Analysis, RISH, Kyoto University)

Eriko Nishimoto

Temperature around the tropical tropopause is one of the most important factors controlling the aridity of air in the stratosphere. Low temperatures generally occur to the east of tropical active convection around the equator and to the west in the subtropics, forming a horseshoe-shaped structure. This structure resembles a stationary wave response known as the Matsuno-Gill pattern, which is induced by the heating generated by the convective activities. This study investigates the variability of the horseshoe-shaped temperature structure and its relationship with the convective activities by using contemporary reanalysis and outgoing longwave radiation (OLR) data.

In the first part of this study, an index representing a zonally asymmetric temperature structure in the tropical tropopause has been established, and then its variability associated with convective activity has been investigated using ERA-40 and NOAA/OLR data. Particularly during the northern and southern summers, low temperatures persist over the tropics and extend north-west and south-west. These low temperatures form a horseshoe-shaped structure that resembles the Matsuno-Gill pattern, which consists of the Rossby response in the western part and the Kelvin response in the eastern part. Regarding the horseshoe-shaped structure, two preliminary indices were defined. As a representative of the Rossby response, an index HSI-R($x; t$) was calculated from a curvature of the 100-hPa temperature along the meridional circle at the equator; as a representative of the Kelvin response, an additional index HSI-K($x; t$) was calculated from a zonal gradient of the 100 hPa temperature along the equator. The two indices were then combined into one index HSI-1 as a result of the EOF analysis using HIS-R and HSI-K values. The index HSI-1 projected a positive linear relation between HSI-R and HSI-K; hence, its negative value should suggest clear existence of the horseshoe-shaped temperature structure.

The negative value of HSI-1 is frequently observed in the Eastern Hemisphere, and its seasonal cycle is closely related to convective activities in and adjacent to the monsoon areas, including the Southern Asian monsoon (SoAM) and the North Pacific monsoon (NPM) domains during the northern summer and the Australian monsoon (AUM) domain during the southern summer. Convective activities in the SoAM and NPM domains may induce two horseshoe-shaped structures individually, and a superposition of the two structures can produce a longitudinally elongated horseshoe-shaped structure during the northern summer. The El Niño-Southern Oscillation (ENSO) cycle is shown to greatly affect variations in HSI-1 values and convective activities, particularly during the southern summer. As discussed in previous studies, low temperatures form the horseshoe-shaped structure over the equator in the western Pacific during the southern summer for the non-El Niño years, while low temperatures shift eastward and becomes more zonally elongated and meridionally narrow for the El Niño years. The longitudinal phase difference between the OLR and HSI-1 minima in the El Niño years is larger than that observed in the non- El Niño years.

During the northern summer, the interannual variability in HSI-1 in the NPM domain is affected by the ENSO cycle in the previous winter, which is consistent with a previous study on convective activities in the NPM area. In the SoAM domain, interannual variation in HSI-1 values is not significantly related to convective activities in the monsoon domain. It was detected that the HSI-1 value in the SoAM domain is mainly controlled by the isolated high temperatures observed around 60°E over the equator during July-August, which are surrounded by the horseshoe-shaped structure. The interannual variation in the HSI-1 values is related to the ENSO cycle. The variation in the high temperature may be related to an anticyclone in the upper troposphere over the Tibetan Plateau. However, further discussion is necessary on the detailed mechanism of formation and variability of the isolated high temperatures.

To summarize the first part of this study, it has been clearly revealed the seasonal and interannual variability of the temperature structure around the tropical tropopause and its relationship with convective activities over the monsoon regions with respect to the horseshoe-shaped temperature structure. Relations to shorter time scale oscillations such as intraseasonal oscillation, traveling Kelvin waves and active/break

cycles in the Asian monsoon circulation are interesting topics for further investigation. Moreover, numerical experiments are required to validate the use of the index representing the horseshoe-shaped temperature field with respect to convective activities.

In the second part of this study, space-time variations of the tropical convective activity and temperature around the tropical tropopause has been investigated associated with the intraseasonal oscillation (ISO), such as the Madden-Julian Oscillation (MJO), by using NOAA/OLR and ERA-Interim data. In the case study of the 1984/85 southern summer, which is during the weak (normal) ENSO period, various types of the convective propagation features associated with the ISO are observed in the unfiltered OLR field. These convective activities accompany low temperatures to their east in the tropics and to their west in the subtropics around the tropical tropopause. These low temperatures form a horseshoe-shaped structure, which resembles the Matsuno-Gill pattern. The 72 ISO events that occur during the southern summer from January 1979 to December 2011 were first selected with respect to the time series at the reference point (102.5°E) where variations of the band-pass-filtered OLR averaged over 5°N-15°S are largest. Cluster analysis was then performed with Ward's method by using the locus of the unfiltered OLR minima in the ISO events, and the propagation features were categorized into five clusters, which consist of 20, 20, 18, 12, and 2 events.

Most of the events in Clusters 1 and 2 occur during the La Niña and El Niño periods, respectively, and those in Clusters 3 and 4 during the weak ENSO periods. In association with the ISO, the convective activities observed in the unfiltered OLR field in Clusters 1 and 3 have a relatively slow speed (<2 m/s) and propagate to 120°E and 135°E, respectively. The faster (~ 4 m/s) convective activities in Clusters 2 and 4 propagate into the central Pacific. The composite SST field reveals the following facts about the convective propagation. During the weak ENSO periods (Clusters 3 and 4), the propagation speed is slow when the SSTs over the western Pacific are relatively low. During the El Niño periods (Cluster 2), as the eastern edge of the warm pool extends over the date line, so does the active convection. To investigate space-time variability in the horseshoe-shaped temperature structure associated with the ISO, the horseshoe-shaped structure index (HSI-1) was used; the index was defined in the first part of this study. The composite HSI-1 fields have similar features to those of OLR, located about 10°-20° degrees west of the active convective area. Both the ISO life cycle and event-to-event variation in the HSI-1 values are significantly correlated with those in the unfiltered OLR values. Those results imply that the convective heating associated with the ISO induces the horseshoe-shaped temperature structure around the tropical tropopause.

Low temperatures at 100 hPa change accordingly with the HSI-1 minima at least in the ISO life cycle. Furthermore, the strength and location of the temperature minima at 100 hPa are different among the ISO clusters. These results could suggest that the different types of the ISO would be different impacts on the troposphere-stratosphere exchange such as the dehydration process depending on their types, considering the previous studies which investigated the possible influence of the ISO and horseshoe-shaped structure on the troposphere-stratosphere exchange process in the TTL. Diagnostic interpretation of reanalysis data and model simulations revealed that much of the upwelling in the TTL is forced by the dissipation of tropical waves such as the Rossby waves. Therefore, the upwelling in the TTL may occur over the horseshoe-shaped temperature structure associated with the ISO.

In the second part of this study it has been clearly revealed the intraseasonal variability in the convective activities and temperatures around the tropical tropopause during the southern summer by employing cluster analysis according to the propagation features of the convective centers. A better understanding of lower troposphere conditions that would induce variations in the propagation features of the convective activities is needed.

Throughout this study it is clearly confirmed that the horseshoe-shaped temperature structure around the tropical tropopause is induced by the heating generated by the convective activities. These results could improve the understanding on the TTL dynamics and, consequently, the troposphere-stratosphere exchange process. The methodologies developed in this study are expected to contribute to future tropical studies. The horseshoe-shaped structure index should become a powerful diagnostic tool for investigating the temperature distribution in the tropical tropopause. As the future work, it would be interesting to compare the tropical tropopause temperatures derived from some reanalysis data sets and climate models by using the horseshoeshaped structure index. The method to categorize the ISOs should be a very helpful to study convectively coupled tropical dynamics. Relationship to the intraseasonal oscillation during the northern summer is an interesting topic for further investigation.

ABSTRACTS (PH D THESIS)

Development of High Rigidity Joint and its Application to Wooden Frame Structure

**(Laboratory of Structural Function, RISH, Kyoto University,
Present: Forest Products Research Institute, Hokkaido Research Organization)**

Yasunobu Noda

According to the act for promotion of use of wood in public buildings, small-scale constructions are desired to be built of wooden materials. In addition, considering the act about long life quality housing, future wood constructions should have easy-renovation system. In those social situations, it could be said that wooden frame structure has an advantage in the room re-arrangement like steel constructions. Therefore several moment resisting joints developed for heavy timber structures have been improved and put to practical usages in recent detached houses and small-scale constructions.

In practical structural design, the horizontal stiffness of wooden portal frame structure tends to be insufficient when it is designed with general-produced medium-sized glulams. One of the reasons is that most mechanical joints have low rigidity. According to the annual meeting reports of Japanese Architecture Institute for the past ten years [1], the studies on moment resisting joints of which cross section sizes of the beam were ranged from 120 x 300 to 150 x 450 mm, reported that the rigidity of mechanical joints were less than 2000 kN･m/rad, on the other hand, that of several glued joints achieved more than 5000 kN･m/rad. Then requirements for rigidity and strength of joint were simulated by an imaginary three-story wooden structure consisting of 6 m span portal frame at 2 m interval in the first floor. In the case that the member of the cross section of more than 120 x 360 mm is used for column and beam, the mechanical joints with rigidity of at least 1800 kN･m/rad are available when the column-leg joint in the portal frame have the same rigidity of the bema-column joint. When the column-leg joints are pin node, however, it is impossible to satisfy the requirement of the Japanese design code even if beam-column joints were fully rigid. In case of more than 120 x 480 mm member, about 5000 kN･m/rad rigidity is required when the beam-column joints are pin node. It is natural that using heavier timber gives higher rigidity and strength to the joint of portal frames, however, it is worth giving an available option of improving joint rigidity for small scale constructions to be composed of minimum size members. Therefore, this study aspired for fully rigid and full strength joint for wooden frame constructions.

First, I focused on the improvement of the Large Finger Joints (LFJ) made of karamatsu (*Larix kaempferi*) glulam of intermediate-member-installed type which is one of adhesive type joints. The plywood laminated member of karamatsu, OSB laminated member or Cross Laminated Timber of karamatsu were employed to replace the intermediate member of a glulam to improve the joint performance. The result of full scale joint tests (Figure.1) suggested that plywood type shows the best performance in terms of the strength and ductility. The strain measurements of the intermediate member of plywood type showed that the shear strength of the intermediate member would be higher than the bending strength. However the sufficient strength value was not obtained due to occurrence of the bending crack to 45 degree direction against the fiber direction of the surface layer which is the weakest direction of plywood bending strength. Moreover, it was thought that triangular pyramidal voids of the finger joint inside of the intermediate member were the weak points [2].

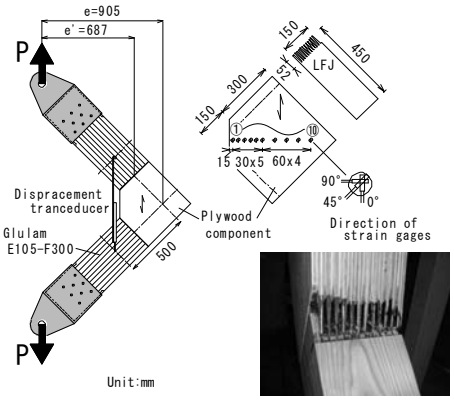

Figure 1. Improved LFJ corner joint test and finger joint inside of plywood type.

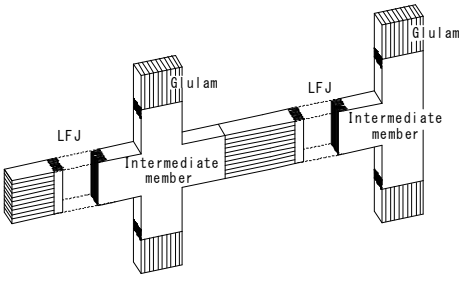

Figure 2. Concept of invented new joint.

Therefore, it was found that achieving the joint of higher

performance is possible by applying more strengthened intermediate member and putting the LFJ part distantly from the intersection area of the column and beam. The concept of the invented new joint system is shown in Figure. 2. On this concept, a technology of compressed wood was applied to strengthen the intermediate member. And the longitudinal joint performance of the LFJ between the intermediate member and the glulam was also verified.

The strength of the LF-Jointed glulam of karamatsu was estimated using results of small scale tensile and bending tests of LF-jointed laminae. The 5th percentile lower limit value of bending strength of glulam connected by the LFJ of 120 mm width was estimated by an equation for modulus of rupture (MOR) using observed tensile and bending strength of the LF-jointed laminae of 30 mm thick and 120 mm width. The strength values of LF-jointed glulams (E105-F300) of different cross sections (120×120, 120×180 and 120×300 mm) were measured by bending test. The estimated value of 5th percentile lower limit of 14.0 N/mm^2 in the case of infinity depth of beams was lower than the LF-jointed glulam test results. It was concluded that the joint efficiency of this LFJ was 46% [3].

Figure 3. Developed joint method of compressed cross-lapped joint.

The developed joint method named a compressed cross-lapped joint (CCLJ) for the intermediate member is shown in Figure. 3. Rectangular veneers with phenol formaldehyde (PF) resin impregnation were arranged at right angles to adjacent layers, aligned at each layer's corners and compressed by a hot-press machine. The moment resisting performance of the CCLJ was tested. The L-shaped specimens of 120 × 180 mm in cross-section made of PF-treated todomatsu (*Abies sachalinensis*) veneer were employed. They were connected to karamatsu glulam (E105-F300) by the LFJ to elongate the moment arms for the test. The bending failure of the L-shaped specimens occurred at the boundary of the cross-lapped part and the arm part, or the LFJ. The bending strength of the boundary was more than 30 N/mm^2. Material property test results of cross-lapped and arm parts suggested that the CCLJ could be regarded as a rigid joint. Also, the strain distribution on the cross-lapped area showed that the shear strength of the cross-lapped area would be higher than the bending strength of the boundary [4].

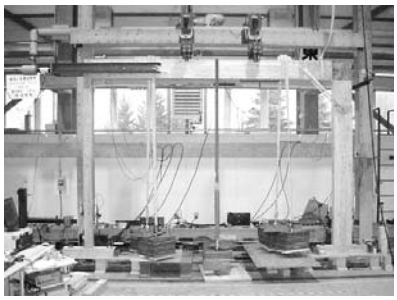

Figure 4. Portal frame racking test with dead load.

And also, the racking performance of the full scale portal frame with the CCLJ was verified in un-symmetrical L-shaped test condition with 3910 mm in span and 2730 mm in height (Figure. 4). The beam and column member of karamatsu glulam (E105-F300) of 120×300 mm in cross-section were jointed to the L-shaped member made of todomatsu veneers by wooden dowel joints with hard maple (*Acer saccharum*). A support column of 120×120 mm in cross-section of karamatsu glulam (E85-F300) was attached at the left side of the frame, connected with a template metal connector (HOWTEC BH255) as semi-rigid node. The horizontal stiffness and the strength of the frame with and without dead load were predicted by explicit formulas for the moment and horizontal displacement relationship introduced from the compatibility of rotation angles at the semi-rigid nodes. The obtained horizontal stiffness of the frame subjected to horizontal load with and without dead load of 20 kN were higher than the predicted results. The strength with dead load was 19% smaller than without dead load. It was concluded that the reduction of the rotational rigidity of template metal connector joint by dead load caused a change of the moment distribution on the beam, which resulted in the moment concentration at the L-shaped member part.

References

[1] *Summaries of Technical Papers of Annual Meeting Architectural Institute of Japan*, Structures III, Timber Structure, 2002-2012.
[2] Y. Noda, T. Mori, K. Komatsu, *Mokuzai Gakkaishi*, vol. 59, No. 1, pp34-44, 2013.
[3] Y. Noda, T. Mori, K. Komatsu, Journal of the Society of Materials Science, vol. 62, No.4, pp.274-279, 2013.
[4] Y. Noda, N. Furuta, K. Komatsu, *Mokuzai Gakkaishi*, vol. 58, No. 6, pp.309-317, 2012.

ABSTRACTS (PH D THESIS)

Investigation of "Joglo" Structure Damaged by Earthquake and Development of Technical Conservation Method for Damaged Structural Members

(Graduate School of Agriculture, Laboratory of Structural Function, RISH, Kyoto University)

Yulianto Purwono Prihatmaji

A post-earthquake survey and experimental evaluation were performed on Joglo Javanese wooden houses. Aims of study are to preserve Joglo as a tangible culture through study on seismic vulnerability, timber mechanical properties, structural performances and repair-strengthening methods.

An Investigation of Traditional Javanese Wooden Houses 'Joglo' Damaged During the May 2006 Yogyakarta Earthquake, Indonesia

Investigations on 20 damaged Joglo buildings reveal that the structure's damage can be classified into three categories: slip between columns and stone foundation, broken joints between outer ring beam and column, and collapse of core structure. Four damage levels were defined: I) damage on the base joint of side structure, II) fatal damage on the side-structure, III) destroyed core structure, and IV) totally collapsed core structure. The dimensional proportion of the joint at the main column and its position in height follows traditional carpenter's common rule, while they have nothing to do with the scale of the building in plane. A strong relationship exists between the ratio of the vertical section area of the main columns and horizontal area of the core structure and level of damage; the smaller the ratio, the higher the damage is extensive. A distinct relationship was identified between the levels of structural damage and the area ratio of core structure and the main column projection. It was verified that structural proportion significantly contributes to the assessment of damage.

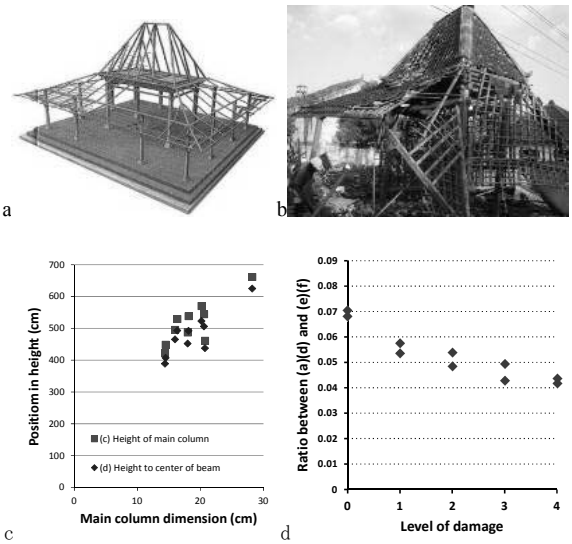

Figure 1. a. Joglo wooden structure; b Joglo damage by earthquake; c. Position in height against main column dimension; d. Ratio between column width/column height and short span/long span of core structure against level of damage.

In Search of Substitution Material for Traditional Javanese Wooden Houses

Due to preserve beautiful wooden art, lack of big Teak stock, and high price of Teak, searching of substitution material for repairing, reinforce and reconstruction of Joglo by compression test, 3 PB test, 4 PB test and 4 PS test for 9 tropical timbers have been done (Fig. 2.a, b and c). As traditional joint construction use mortise and tenon system, the yield stress at intersection of members is important.

From compression test, all of tropical timber species showed that MOE and Yield stress has strong relationship with densities (Fig. 2d). There were clear tendency that the smaller density indicates the smaller MOE. Acacia, Teak, Ketepeng and Jackfruit has similar trend of increasing MOE and yield stress (Fig. 2.e). From 3 PB test, 4 PB test and 4 PS test, all

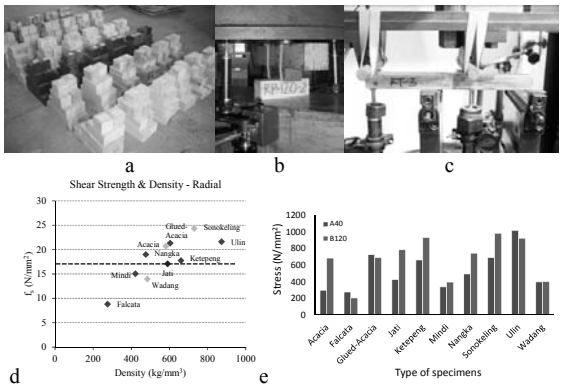

Figure 2. a. Small scale tropical timber hardwood specimens; b. partial compression test; c. 4 PB test; d. Relationship between Shear strength and density; e. Difference of increase ratio among the specimens.

specimen showed that MOE and MOR has no relationship with densities. Shear strength and shear modulus showed quite strong relationship with densities. In terms of shear modulus, Ketepeng, Acacia, Teak and Jackfruit have quite similar mechanical properties. Considering those results, Ketepeng, Acacia, Teak and Jackfruit are considered to substitute Jati (Teak) to be used in Javanese wooden house reconstruction.

Mechanical Analysis of Rotation Performance of Javanese Traditional Timber Joint

To confirm the most effective criteria on strength of the building, the static characteristic of these structural components has been investigated experimentally for each joint (Fig. 3.a and b). A total of 12 full-scale specimens made of glued *Acacia-mangium* were tested. The horizontal cyclic load was applied on the specimen placed in pin joint frame from two mutually perpendicular directions. As the test result, columns and beams located in perpendicular to the loading plane have few influences on the rotational property by cyclic loading. Failure modes were caused by embedment, crack, and split in beams parallel to the load direction. From the curve of load and rotational relationship, occurrence of initial slackness leaded to the larger deformation.

The curve of moment-rotational angle relationship between long beam with mortise and long beam with tenon didn't show a significant difference as a result (Fig. 3.c, d, e and f). It indicates that traditional carpenters have chosen a proper ratio of dimension of two-directional joint to achieve uniform structural behavior against lateral force. Assuming the rotation center is located at geometrical center view of each member, the prediction meets fairly good experimental results.

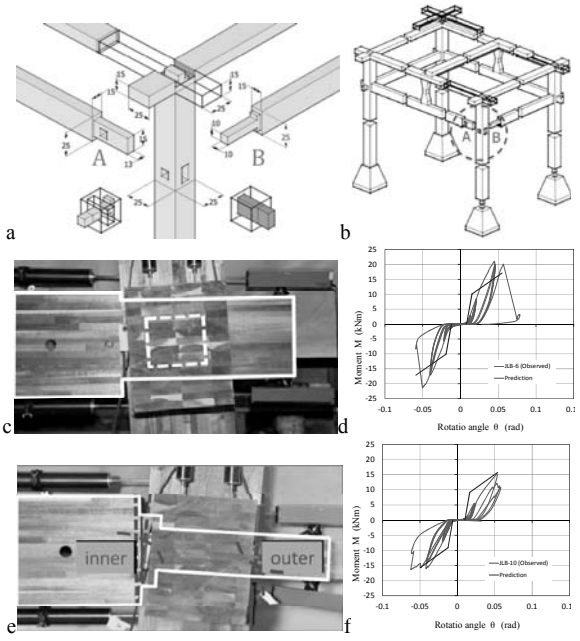

Figure 3. b. Joglo joint construction; b. Core structure of Joglo; c and d. Joint detail type A and it's curve deformation; e and f. Joint detail type B and it's curve deformation.

Repair Technique of Damaged Timber Beam by Insertion of Compressed Wood Plate and Adhesive-Vacuumed Method

To provide an appropriate technical conservation method for damaged structural members, we purpose repair technique by insertion of compressed wood plate and adhesive-vacuumed method (Fig.4.a). There was relationship between strength of Falcata compressed wood (FCW) and their compression ratio. Bigger compress ratio of FCW leads higher strength. Vacuumed method shows the highest recovery ratio of apparent MOE and MOR. Insertion of FCW plate increased the P_{max} and the stiffness. Application of triple compressed wood plate insertion cover 83 % of original strength (Fig.4.b).

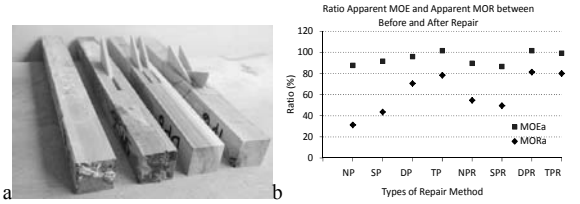

NP: no plate, SP: single plate, DP: double plate, TP: triple plate, R: re-bending action

Figure 4. a. Repair technique by insertion of FCW; b. Comparison ratio apparent MOE and apparent MOR between before and after repair among repair methods applied.

Acknowledgements

The study was funded by the Directorate of Higher Education, Ministry of National Education Republic of Indonesia under DIKTI Scholarship Batch 3a (2009). This work was supported also by Islamic University of Indonesia, Yogyakarta, Indonesia.

ABSTRACTS (PH D THESIS)

Studies on Structural Analysis, Self-Organizing Capacity and Disassembly of Nanocelluloses

**(Graduate School of Agriculture,
Laboratory of Active Bio-based Materials, RISH, Kyoto University)**

Kojiro UETANI

Cellulose is naturally provided as the crystalline nanofibers with a high tensile stiffness, a high elastic modulus and a low coefficient of thermal expansion (e.g., in the case of cellulose I crystalline, 3~6 GPa,[1] 140~150 GPa,[2] and 10^{-7} K^{-1},[3] respectively). Since various methods and techniques have been developed to produce "nanocelluloses (NCs)", the potentials of NCs for various materials were accordingly developed. Still, there are several major but fundamental issues arising in utilization of NCs as nanomaterials: the length and shape estimation of long and coiled nanofibers having bundles or branches, the shape-dependent self-organizing capacity for fibrous materials, and so on. In this thesis I developed the novel approach by introducing the evaporation induced self-assembly (EISA) techniques to analyze the structures and self-organizing behaviors for nanocelluloses.

"Coffee ring method": Semiquantitative structural analysis for nanocelluloses[4]

A coffee ring (a ring-shaped deposition of colloidal particles) is readily observed when a coffee drop dries on a table. This EISA occurs largely because of the pinning of the contact line of the droplet by the deposited particles, and the outward capillary flow to the contact line generated by the regional change in the evaporation flux.[5] I focused on the differences in the excluded volume effects induced by the anisotropy of nanocelluloses during enrichment, which produced the different packing fractions in the rings.

Three kinds of cellulose nanoparticles (CNPs) were prepared; cotton nanowhiskers (CNWs), tunicin nanowhiskers (TNWs), and sugi nanofibers (SNFs). Both whiskers were produced via acid hydrolysis using H_2SO_4, and sugi pulp was fibrillated using a grinder to obtain SNFs. Transmission electron microscope (TEM) observation was able to measure the precise size distribution for CNWs and TNWs, whereas the long and coiled SNFs were unable be measured. To estimate the length of SNFs, I thus formed the coffee rings for each CNP suspensions on the cleaned glass plates.

Each ring exhibited the obviously different width in the same concentration of nanocelluloses, as shown in Figure 1. To detect the excluded volume effects for nanocelluloses, I measured the ring width normalized by the ring radius (w/R) against the suspension concentration (Figure 1d). The plots had the logarithmic relation for each sample, showing the different excluded volume effects. I analyzed these plots by computing the ring volumes, and developed the theoretical method to simultaneously estimate the shape and length. The method revealed that the SNF units were coiled in a steric structure with a small apparent aspect ratio and with the same volume as a sphere of

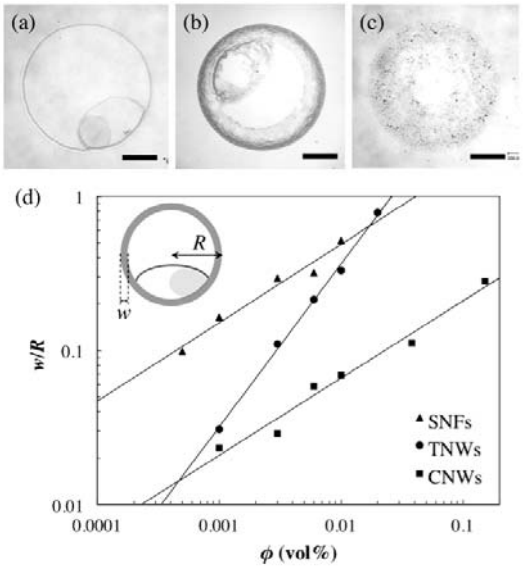

Figure 1. Optical micrographs of (a) CNW, (b) TNW, and (c) SNF stains left on the substrate after the evaporation of a 1 μL droplet of a 0.01 vol% suspension. Note 500 μm scale bars in lower right corners. (d) The width of the ring (w) at depinning normalized by the droplet radius ($R \approx 1$ mm) vs the concentration ( ). A best fit to a power law gave an exponent of 0.51±0.01 for the SNFs, 0.50±0.01 for the CNWs, and 1.06±0.01 for the TNWs. The inset shows the schematic illustration of a typical CNW coffee ring, with twice depinning.

ABSTRACTS (PH D THESIS)

radius 693.22 nm, with 1.08 wt %; the length was estimated as 11.33 μm. This coffee ring method allows semiquantitative volume information to be determined, owing to the excluded volume of particles; this permits a semiquantitative estimation to be made of the length of highly anisotropic colloids, as long as the Debye length is determined for the colloids in question. This method also allows the effective size and the conformational structure of colloids in different systems to be compared.

Self-organizing capacity of nanocelluloses via droplet evaporation[6]

The great potential of nanofibers, for applications to functional materials, provides a strong motivation to understand the relation between the shape and the self-organizing capacity of these particles, and the processes by which they can be made to form higher-order structures. Since the fibril-like shape can be determined through the coffee ring method, I then explored the self-organizing behavior for different shaped nanocelluloses.

I succeeded in producing the semi-flexible nanofibers (TNFs) and rod-like nanowhiskers (TNWs) from the same origin of tunicate cellulose. Both nanocellulose suspensions were subjected to the EISA system in 2D (coffee ring formation) for determining the shape and length, and in 3D (spray drying) to form the microparticles to observe the autonomously-expressed assembly.

EISA results in 3D were found to be consistent with those in 2D for both TNWs and TNFs. The rod-like TNWs formed unexemplied curved discotic MPs by self-organized nematic bundles during spray drying, as displayed in Figure 2, whereas the semi-flexible TNFs formed flattened MPs, albeit with multiple sharp kinks and rough contours. The rod-like nanocelluloses exhibited the self-organizing capacity of the phase transition and left-handed chirality to form MPs with nematic rings along the contours. On the other hand, the semi-flexible nanofibers with a w/R value of 0.91 failed to align or to undergo a phase transition by EISA system. The expression of the self-organizing capacity of rod-like particles was found to be independent of initial droplet shapes and sizes via surface tension measurements.

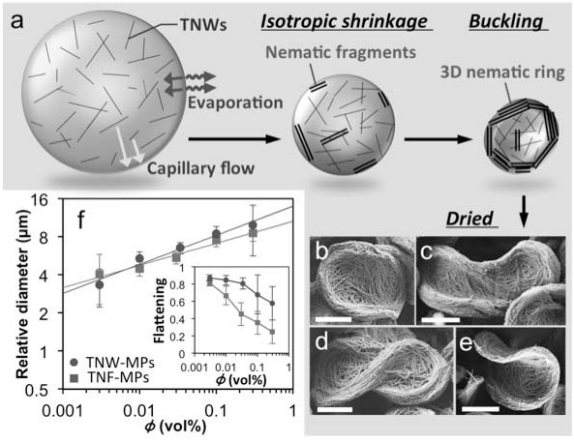

Figure 2. (a) Schematic illustration of the EISA process in 3D during spray drying for rod-like TNWs. Nematic rings in TNW-MP sprayed at ≤ 0.034 vol% formed circular discs (b), "peanut-shaped" (c) or "figure-eight-shaped" (d) structures, and curved discotic shapes (e) (scale bars: 1 μm). The relation between the size and concentration ( ) showed a power-law dependence (f). The inset shows the flattening of MPs decreased (became closer to the spherical) as the particle size increased. Data are means ± SD of ~20 measurements.

Acknowledgements

The author thanks Dr Yoshiki Horikawa, of the Research Institute for Sustainable Humanosphere (RISH), Kyoto University, for the TEM observation. This research was supported by a Grant-in-Aid for Scientific Research (Grant 224452) from the Japan Society for the Promotion of Science (JSPS).

References

[1] Saito, T.; Kuramae, R.; Wohlet, J.; Berglund, L. A.; Isogai, A. *Biomacromolecules.* **2013**, *14*, 248–253.
[2] Sturcová, A.; Davies, G. R.; Eichhorn, S. J. *Biomacromolecules* **2005**, *6*, 1055–1061.
[3] Nishino, T.; Matsuda, I.; Hirao, K. *Macromolecules* **2004**, *37*, 7683–7687.
[4] Uetani, K.; Yano, H. *ACS Macro lett.* **2012**, *1*, 651–655.
[5] Deegan, R. D.; Bakajin, O.; Dupont, T. F.; Huber, G.; Nagel, S. R.; Witten, T. A. *Nature* (London) **1997**, *389*, 827–829.
[6] Uetani, K.; Yano, H. *Soft Matter* **2013**, *9*, 3396–3401.

ABSTRACTS (MASTER THESIS)

Development of configurable software-defined receiver for atmospheric radars

**(Graduate School of Informatics,
Laboratory of Radar Atmospheric Science, RISH, Kyoto University)**

Toshiyuki Fujita

In the study, a new digital receiver for atmospheric radars was developed. The digital receiver comprises a general-purpose software-defined radio receiver referred to as Universal Software Radio Peripheral 2 (USRP2) and a commercial personal computer (PC), and the purchase price of USRP2 is less than USD 2000. The receiver is able to collect received signals at an intermediate frequency (IF) of 130 MHz with a sample rate of 10 MS s^{-1}. The USRP2 digitizes IF received signals, produces IQ time series, and then transfers the IQ time series to the PC through Gigabit Ethernet. The PC receives the IQ time series, performs range sampling, carries out filtering in the range direction, decodes phase-modulated received signals, integrates the received signals in time, and finally saves the processed data to the hard disk drive. Because only sequential data transfer from the USRP2 to the PC is available, the range sampling is triggered by the transmitted pulse leaked to the receiver. In order to perform range imaging with multiple frequencies, the digital receiver executes real-time signal processing for each of the time series collected at different frequencies. Further, in order to implement oversampling, the receiver is able to decode phase-modulated oversampled signals by interleaving oversampled signals in the range direction. Because the program code for real-time signal processing at the PC is written in the C++ language, the signal processing executed by the digital receiver is easy to implement, reconfigure, and reuse.

Using the measurement result from a 1.3-GHz range imaging atmospheric radar, we demonstrate that the digital receiver, which is capable of performing real-time signal processing for range imaging and oversampling, is useful for resolving fine-scale structure of atmospheric turbulence with a vertical scale as small as 100 m.

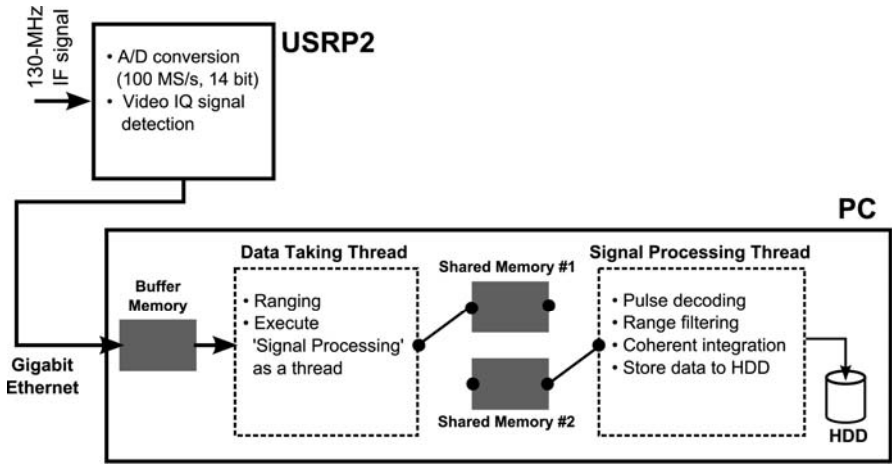

Figure 1. Signal flow diagram of the digital receiver.

Acknowledgements

This research was supported by Adaptable and Seamless Technology Transfer Program through Target-Driven R&D (A-STEP) Exploratory Research (Research No. AS232Z00186A) funded by Japan Science and Technology Agency and the research grant for Mission Research on Sustainable Humanosphere from the Research Institute for Sustainable Humanosphere (RISH), Kyoto University.

ABSTRACTS (MASTER THESIS)

A study on development of statistical analysis system for variations of atmospheric environment

**(Graduate School of Informatics,
Laboratory of Atmospheric Sensing and Diagnosis, RISH, Kyoto University)**

Ryota Hamaguchi

Integrated data analysis of various observations is important to understand the atmospheric environment, which requires cross-reference of data-base archived at different institutes/universities. The Inter-university Upper atmosphere Global Observation NETwork (IUGONET) project has been conducted in FY 2009-2014 in order to enhance data exchange among the Japanese universities and research institutes. This project aims at establishing a metadata-database (MDDB) system for ground-based observations as well as the iUgonet Data Analysis Software (UDAS).

This thesis is concerned with development of the statistical analysis system as a part of UDAS, consisting of five functions as follows: (1) A test for the difference in the mean values between the two data distributions. (2) Cross-correlation coefficient and a test for non-correlation. (3) Analysis of coherence and phase for each frequency component. (4) S(Stockwell) transform analysis: Temporal variations of spectral density and dominant frequency for transient phenomena. (5) Trend test for the slope of a linear regression. Because the sampling interval of observations is not always constant and missing data are sometimes included, a linear interpolation is adopted on the data before applying the statistical analysis system.

We applied this analysis system for the two meteor radars in Indonesia. The same radar systems are operated on the equator in west Sumatra and west Papua, Indonesia in 2003-2013. These data-sets are unique and useful to study longitude variations of the wind fields. First, we test the altitude distribution of meter echoes, and found no difference in the mean altitude, but a slight long-term trend. Frequency spectrum indicated that the quasi-two day wave is dominant at 90 km altitude for the meridional wind component, where the long-term envelope of the wave amplitudes correlated well between the two radars. This statistical analysis system can clarify trends and variations of atmospheric conditions. Therefore, it is expected to advance our understanding on the global changes as well as the effects of solar activities on the lining environment.

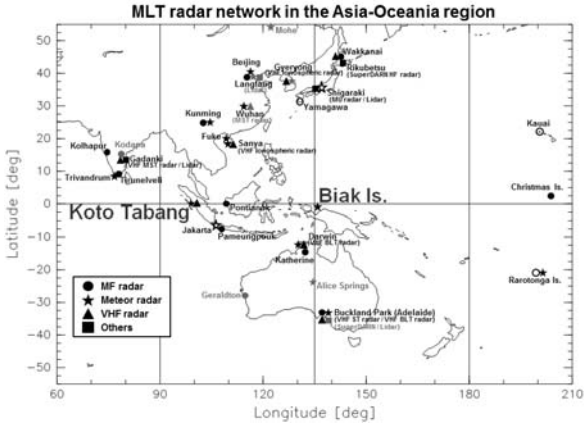

Figure 1. Mesosphere and lower thermosphere (MLT) radar network in the Asia-Oceania region.

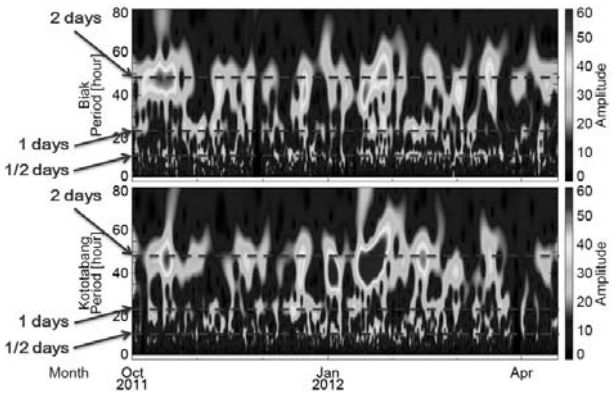

Figure 2. Dynamic spectra of meridional winds at 90 km over Biak and Kototabang for Oct.-Apr., 2011, derived from the S-transform analysis. The color bar indicates the amplitude ranging from 0 to 60 m/s.

ABSTRACTS (MASTER THESIS)

Study and Development of Microwave Irradiating System for a Woody Biomass Refinery

(Graduate School of Engineering, Laboratory of Applied Radio Engineering for Humanosphere, RISH, Kyoto University)

Naoki Hasegawa

Woody biomass consists of cellulose, hemicellulose, and lignin. In the woody biomass, lignin coats on the cellulose and hemicellulose which call lignocellulose. This thesis presents improvement of a microwave irradiating launcher for lignocellulose pretreatment for creating bioethanol. It also presents study and design of a container which is irradiated with electromagnetic wave for reactive tests of a catalyzer in order to create a functional polymer from lignin. First of all, the permittivity of materials was measured with temperature. The measured permittivity data is useful for designing the microwave irradiating system. From measurement results, the microwave penetration depth and absorbed power in the materials were calculated. Secondly, a simplified launcher of pretreatment system was designed by 3D electromagnetic simulator. The simplified launcher design was conducted by adjusting the input impedance of the metal pipe filled with the woody-biomass mixture. As a result, the launcher without the tuners provided the reflected power of less than 1 %. Next a multi-port microwave-irradiating system was developed for a bench-scale plant. Figure 1 shows designing of a multi-port microwave-irradiating system by 3D electromagnetic simulator. From practical measurement results, the absorption efficiency of the apparatus realized about 80 %. Thirdly, a coaxial reaction container irradiated with electromagnetic wave was developed in a wide frequency range from 80MHz to 2.7 GHz. The coaxial container was designed in the 3D FEM simulator and a prototype was developed. As a result, the coaxial container provided the reflected power of less than 10 % above the frequency of 0.85 GHz when the container filled with distilled water at 30 ºC. From the heating test with a high power amplifier, distilled water was heated above the 100 ºC by both 915 MHz and 2.45 GHz electromagnetic waves in the container.

Acknowledgements

A part of this thesis was supported by the New Energy and Industrial Technology Development Organization (NEDO) project, “Development of Technology for High-efficiency Conversion of Biomass and Other Energy”, and JST, CREST.

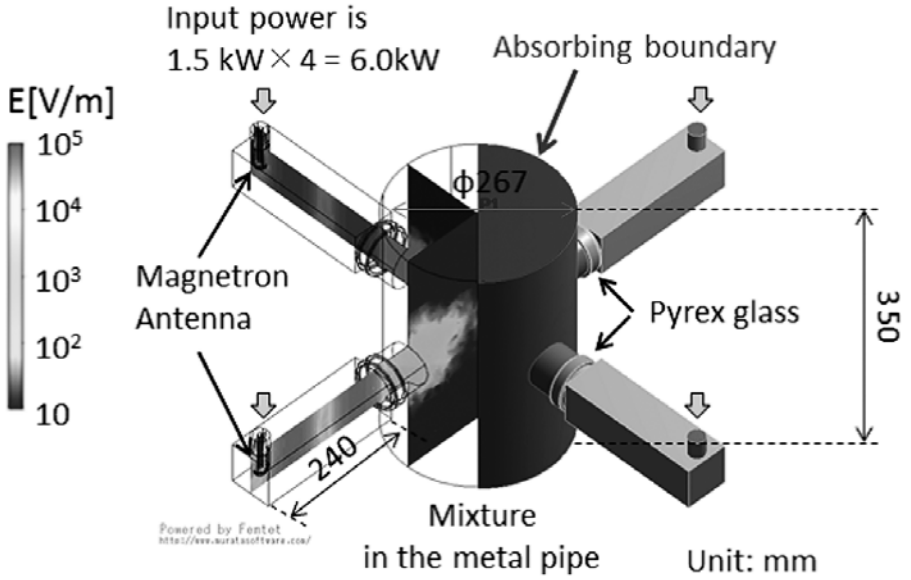

Figure 1. Designing of a multi-port microwave-irradiating system by 3D electromagnetic simulator.

ABSTRACTS (MASTER THESIS)

Development of 24 GHz-Band Rectenna and Study on its MMIC Integration

**(Graduate School of Engineering,
Laboratory of Applied Radio Engineering for Humanosphere, RISH, Kyoto University)**

Ken Hatano

Microwave Power Transmission (MPT) in high frequency is essential to broaden a range of MPT applications. In higher frequency, however, the RF-dc conversion efficiency of rectennas decreases. Moreover, modeling errors of connectors, diodes, and propagation loss in a transmission line provide disagreement between simulated results and measured results. The objective of the present thesis is to design and develop highly-efficient 24 GHz-band rectennas with high accuracy. We adopted a microstrip line as a transmission line. We selected the Teflon substrate of 0.1mm thickness and set the width of the center conductor narrow in order to suppress the effect of the surface wave which causes a radiation loss. In a real microstrip line, a conductor loss increases because of the edge effect and the roughness of the center conductor. Thus, we estimated the conductor loss in the real microstrip line. Additionally, we modeled the end launch connector which was mounted to the rectifier. We also fabricated jig circuits for diode modeling, and fitted the simulated results to the measured results. We finally determined the elements of diode equivalent circuits which include parasitic elements. We developed a new-type rectifier which included the propagation loss in the real microstrip line, the connector equivalent circuit, and the diode equivalent circuit. The new-type rectifier achieved the efficiency of 56.0% in the simulation and 51.8 % in the measurement when the input power was 130 mW and the load resistance was 50 Ω. We obtained the highest efficiency of 57.4 % in the measurement at 297 mW and 60 Ω. We also succeeded to develop a monolithic microwave integrated circuit (MMIC) rectifier whose size was 1mm x 2.3 mm, as shown in Figure 1. The MMIC rectifier produced the efficiency of 48.0 % in the measurement at 194 mW and 120 Ω. We designed a patch antenna for the MMIC rectifier, and fabricated a MMIC mounted rectenna. We conducted a 24 GHz MPT experiment with the 2 x 2 MMIC mounted rectenna array, and succeeded motor drive by 24 GHz MPT.

References

[1] K. Hatano, N. Shinohara, T. Mitani, T. Seki, and M. Kawashima, “Development of Improved 24GHz-Band Class-F Load Rectennas”, IEEE MTT-S International Microwave Workshop Series on Innovative Wireless Power Transmission: Technologies, Systems, and Applications (IMWS-IWPT 2012), FRI-F-14, Proceedings pp.163-166, Kyoto, Japan, May 10-11, 2012.

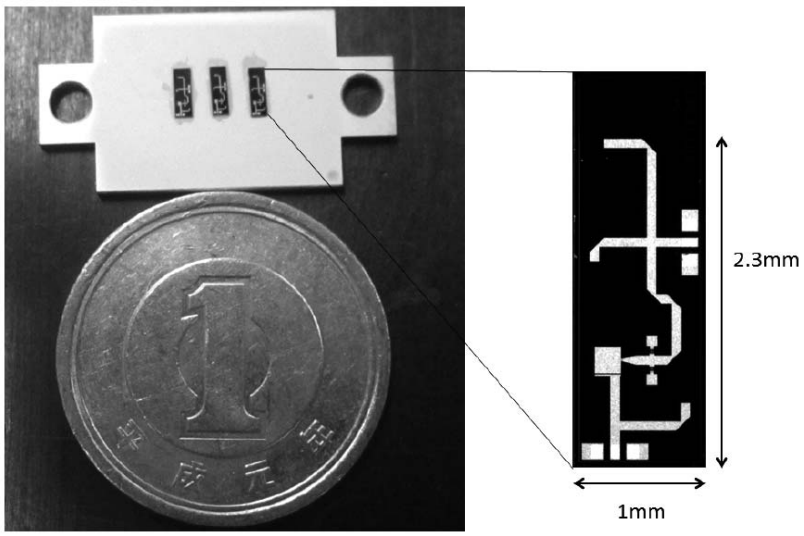

Figure 1. Photograph of a developed 24 GHz-band MMIC rectenna.

ABSTRACTS (MASTER THESIS)

Development of the miniaturized waveform receiver system with the built-in preamplifier and onboard measurement system

**(Graduate School of Engineering,
Laboratory of Space Systems and Astronautics, RISH, Kyoto University)**

Hiromune Ishii

Plasma waves in space plasma transport kinetic energies of plasma particles through wave-particle interactions, because the space plasma is collisionless. Since plasma wave receivers onboard scientific satellites provide significant information on energy exchange processes between waves and particles, they are the essential onboard instruments in science missions, which target the exploration of electromagnetic environments in space. The present paper introduces the development of the very small waveform receiver system with the built-in preamplifiers. The necessary analogue components of the system were realized inside a small chip with the size of 5mm x 5mm using the ASIC (Application Specific Integrated Circuits) technology. The developed system also has the onboad calibration circuit. The low noise preamplifier is very significant for plasma wave receivers. It decides the sensitivity of the waveform receiver system. Since the target frequency range is below 100 kHz in the waveform receiver system, the flicker noise is dominant in the MOSFET relative to the thermal noise. In order to overcome the MOS disadvantage on the flicker noise, we designed the operational amplifier having the input MOS with a large gate area. The preamplifier manufactured under our design shows that the noise level is 25nV/$\sqrt{}$Hz at 1kHz. The D/A converter takes a role in converting model waveform data stored on the onboard memory into analogue waveforms. We designed the 10-bit D/A converter inside a chip. The output signal of the D/A converter is fed into the input of the preamplifier in order to execute the calibration of the receiver system including the effect of the impedance of the electric field sensor. After the function and performance tests of each component implemented inside a chip, we conducted the comprehensive tests under the combination of the preamplifier, waveform receiver, and onboard calibration system. The results showed that the system has the high performance enough for future science missions.

ABSTRACTS (MASTER THESIS)

Study on generation of Electron Cyclotron Harmonic waves around the Moon

**(Graduate School of Engineering,
Laboratory of Space Systems and Astronautics, RISH, Kyoto University)**

Yumiko Katayama

The present paper discusses the generation of Electron Cyclotron Harmonic (ECH) waves observed around the moon. Plasma wave data obtained by the KAGUYA satellite show the existence of two kinds of ECH waves. They are: the ECH waves with lower order harmonics and ones with higher order harmonics which frequencies are close to the upper hybrid resonance frequency. ECH waves can be observed only when the moon is inside the terrestrial magnetosphere. They never appear in the solar wind. The configuration of local magnetic fields is also important. KAGUYA observes the both types of ECH waves along the magnetic field lines which are connected with magnetic anomalies which are scattered on the moon's surface. Furthermore, while the lower order harmonics are observed in the nightside of the moon in the plasma sheet and lobe regions, the higher order harmonics are observed in the dayside of the moon in the lobe region. The correlation studies between waves and particles show that the existence of two components of electrons is essential for the observation of the both types of ECH waves. Two components of electrons mean hot electrons with the loss cone velocity distribution and cold electrons. The formation of cold electrons is classified into two mechanisms. One is the acceleration over the nightside moon surface which is negatively charged and the other is the emission of photo electrons while the spacecraft gets sunlight.

To understand the relation of ECH waves and electron distribution, we conducted the linear dispersion relation analysis and particle simulation using the realistic plasma parameters of electromagnetic environment based on the KAGUYA observation. The results clearly showed the parametric dependence of the ECH wave growth under the co-existence of the loss cone distribution of hot electrons and cold electrons. We discuss the generation of ECH waves consulting the parametric dependence and explain the relation of the observing ECH waves with the moon location in the magnetosphere.

ABSTRACTS (MASTER THESIS)

Study on Transmitting Antennas in Microwave Wireless Power Supply System to Vehicle Roof

**(Graduate School of Engineering,
Laboratory of Applied Radio Engineering for Humanosphere, RISH, Kyoto University)**

Yuta Kubo

The thesis presents microwave wireless power supply systems for electric vehicles using a new charging method unlike the conventional methods adopted in our previous studies. In the new method, receiving antennas are mounted on the roof of vehicles, and they receive microwave power radiated downward from transmitting antennas, which are located at several meters in height. Three requirements have to be met when we apply this method to the charging system: (i) the transmission efficiency should be high, (ii) the undesired radiation should be well suppressed under 1 mW/cm^2, and (iii) flat-topped uniform power distribution should be on the surface of receiving antennas. In this thesis, transmitting antennas are studied by computer experiments in order to meet these three requirements. First, electromagnetic analyses of six kinds of single element antennas and a two-dimensional array antenna comprising 169 horn elements were conducted at the 5.8 GHz ISM band by using HFSS. Single element antennas were unable to meet any of those requirements; on the other hand, a two-dimensional array antenna with the tapered amplitude excitation showed good results in achieving high transmission efficiency of around 99% and lowering side lobe levels. Then, we designed one/two dimensional transmitting array antennas comprising patch elements at the 2.45 GHz/5.8 GHz ISM bands. The excitation phases and amplitudes were optimized by using genetic algorithm (GA) in order to find out their optimum combination that yields flat-topped radiation patterns. The numerical results indicate that the optimized phases and amplitudes can form flat-topped patterns. To validate the practicability of flat-topped patterns, we also conducted beam-forming experiments using a phased array antenna at 5.8 GHz. We successfully demonstrated that the measured radiation pattern was consistent fully with that of simulation results. Three-dimensional simulations using finite-difference time-domain (FDTD) method were also executed to clarify the propagation and scattering behavior of electromagnetic waves, as shown in Figure 1.

References

[1] Y. Kubo, N. Shinohara, and T. Mitani, “Development of a kW Class Microwave Wireless Power Supply System to a Vehicle Roof”, IEEE MTT-S International Microwave Workshop Series on Innovative Wireless Power Transmission: Technologies, Systems, and Applications (IMWS-IWPT 2012), FRI-G-1, Proceedings pp.205-208, Kyoto, Japan, May 10-11, 2012.

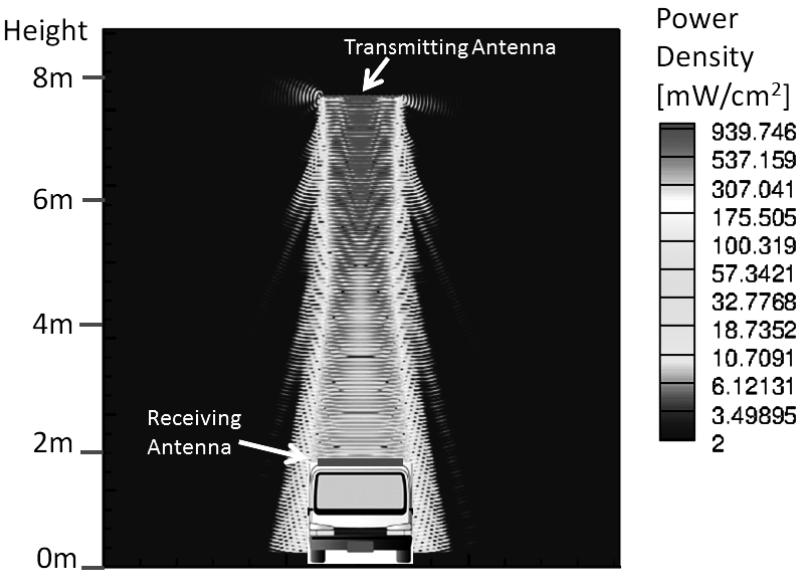

Figure 1. Three-dimensional electromagnetic simulation from the transmitting array antenna to the vehicle roof.

ABSTRACTS (MASTER THESIS)

Development of a scanning Raman lidar for observing the spatio-temporal distribution of water vapor

**(Graduate School of Informatics,
Laboratory of Atmospheric Sensing and Diagnosis, RISH, Kyoto University)**

Makoto Matsuda

Water vapor and aerosol particles are important atmospheric constituents that play a key role in the atmospheric processes such as thermodynamics, radiative forcing, cloud physics, and chemistry. Atmospheric constituents near the surface are highly variable spatially and temporally, because of the complex turbulent flow over the surface. It is required to innovative techniques for observing the distributions of atmospheric constituents with good spatio-temporal resolution. We have newly developed a scanning Raman lidar to measure the spatio-temporal distributions of the water vapor and aerosol particles near the surface, which is useful to study the detailed behavior of meteorological phenomena as well as interactions of aerosol particles with water vapor.

Considering the eye-safe operation in urban districts, we employed the UV laser of 355 nm. We developed a scanning mirror system which comprises with highly reflective mirrors and a rotational stage. By use of the program-controlled rotational stage, vertical scan into any zenith direction can be operated with a maximum speed of 1.8° /s. Differences between the temporal variations of water vapor mixing ratio by the scanning Raman lidar and those by the conventional lidar for observing a vertical point are less than 2.5 %. It is indicated that the developed system can measure water vapor correctly though the scanning system is attached.

We have demonstrated the potential of the scanning Raman lidar in the forest region at the Shigaraki MU observatory in August and October, 2012. We performed a vertical scan in a zenith sector of 48° with a constant step width of 1.5°. The temporal resolution of each pointing direction was 30 s. We found that water vapor mixing ratio within the surface boundary layer varied in a range of 13.5 - 16.5 g/kg. It is suggested that the spatial variations are highly sensitive under the different topography. This system can also apply to the study of the cloud microstructures as well as understanding the spatial variations of atmospheric boundary layer height.

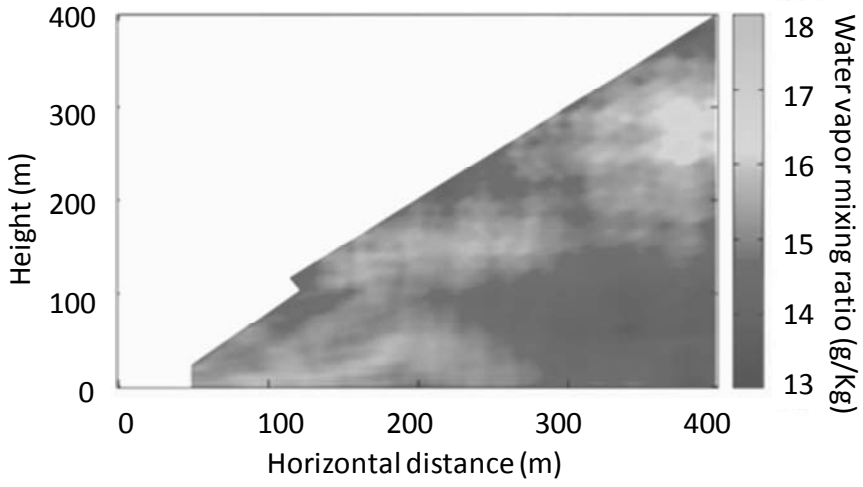

Figure 1. Distribution of water vapor mixing ratio in a vertical plane over Shigaraki at 22:17 JST on August 28, 2012.

ABSTRACTS (MASTER THESIS)

Crystallization of hinokiresinol synthase

**(Graduate School of Agriculture,
Laboratory of Metabolic Science of Forest Plants and Microorganisms,
RISH, Kyoto University)**

Daichi Mori

Wood constitutes about 90% of terrestrial biomass. Wood is composed of sapwood and heartwood, the latter of which occupies large part of large-diametered wood and contains secondary metabolites called heartwood constituents. Heartwood constituents affect the coloration and physical property of heartwood such as vibration characteristic and dimensional stability. Furthermore, heartwood constituents usually have various biological activities. The presence of heartwood constituents may contribute to the longevity of trees. To elucidate the mechanism of heartwood formation is important to improve the quality of wood biomass.

Norlignan is a class of heartwood constituents typically found in conifers such Cupressaceae and Araucariaceae. Norlignans are also found in monocotyledonous species. Previous research revealed that norlignans, *cis*- and *trans*-hinokiresinols, were enzymatically formed from *p*-coumaroyl CoA and *p*-coumaryl alcohol. Later, the two genes (*HRSα* and *HRSβ*) encoding *cis*-hinokiresinol synthase (HRS) were identified. Interestingly, recombinant proteins obtained by individual expression of *HRSα* and *HRSβ* catalyzed the formation of (*7S*)-*trans*-hinokiresinol at 20.6 and 9.0% enantiomer excess (% e.e.). By contrast, the equivalent mixture of recombinant HRSα and HRSβ catalyzed the formation of only (*7S*)-*cis*-hinokiresinol with more than 99% e.e. These results indicated that the subunit composition of HRS is able to control *cis/trans* isomerism and enantioselectivity in hinokiresinol formation (Figure). However, the reaction mechanism mediated by HRS and the stereochemical regulatory mechanism of the reaction by subunit composition have not been elucidated. As a first step towards the elucidation of these mechanisms, we established crystallization condition of recombinant HRSβ.

The author established a large-scaled purification of recombinant HRSs by the combination of immobilized metal ion affinity chromatography (IMAC) and anionic exchange chromatography. Yield of purified HRSs was about 0.5 mg L^{-1} culture medium for recombinant HRSα and about 5 mg L^{-1} culture medium for recombinant HRSβ and a recombinant protein (HRSαβ) coexpressed with *HRSα* and *HRSβ*. However, recombinant HRSs were found to be easily aggregated or denatured during storage in an unoptimized condition. Therefore, the optimized condition for the storage of HRSs was screened by thermal shift assay. As a result, the presence of polyols was found to stabilize recombinant HRSβ and HRSαβ, respectively.

Using the stabilized condition for storage of recombinant HRSs, we screened a crystallization condition for recombinant HRSs. Among recombinant HRSs, recombinant HRSβ was successfully crystallized at 293 K by the sitting-drop vapor-diffusion method. The crystals thus obtained were analyzed by X-ray diffraction experiments in SPring-8. X-ray diffraction was observed in two crystals. A crystal obtained in the reservoir solution supplemented with 0.01 mM *p*-coumaric acid diffracted to 3.85 Å resolution, and a crystal obtained in the reservoir solution supplemented with 0.1 mM *p*-coumaryl alcohol diffracted to 3.15 Å resolution. Further optimization of crystallization condition would be needed to obtain higher resolution of diffraction.

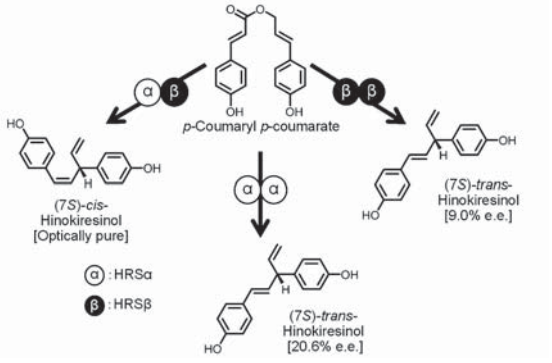

Figure. Hinokiresinol formation controlled by HRS subunit composition.

Acknowledgements

The author thanks Prof. Bunzo Mikami, Graduate School of Agriculture, Kyoto University for his supervising crystallization and X-ray crystallography.

ABSTRACTS (MASTER THESIS)

Biochemical analysis of coumarin-specific prenyltransferase activities in lemon peel

**(Graduate School of Agriculture,
Laboratory of Plant Gene Expression, RISH, Kyoto University)**

Ryosuke Munakata

Coumarins (α-benzopyrones) form a large group of plant polyphenols, and thus far about 1,500 coumarin derivatives have been isolated from plants. Coumarins occur ubiquitously in the plant kingdom, and coumarin derivatives exhibit a variety of biological functions such as chemoprevention against pathogens, herbivores, and abiotic stresses, implying physiological roles of coumarins for plants in the adaption to environmental stresses. Besides, some coumarin derivatives are also known to act beneficially on human health due to their therapeutic effects, e. g., inhibitory activities against various tumor cells and mycobacteria, which have been extensively studied in the medical and pharmaceutical fields for the treatments of human disorders.

In plant cells, almost coumarin molecules undergo some modifications, i. e., glycosylation, prenylation, hydroxylation, methylation, and prenylation. Prenylation contributes to the enhancement of biological activities of coumarins. As for prenyltransferases of coumarins, umbelliferone 6-dimethylallyltransferase activity and umbelliferone 7-*O*-dimethylallyltransferase activity were reported in *Ruta graveolens*, and *Ammi majus*, respectively. However, there is no report on coumarin-prenyltransferase activities in citrus species, regardless of their importance in basic and applied sciences. We employed lemon (Citrus limon) as a resource for the study on prenyltransferase specific for coumarins because a large amount of prenylated coumarins are accumulated in peels. Plant-derived prenyltransferases for aromatic metabolites have been studied for more than four decades.

We have detected both *O*- and *C*-prenyltransferase activities for coumarin substrates in the microsome fraction prepared from lemon peel (Munakata et al., 2012). Bergaptol was the most preferred substrate out of various coumarin derivatives tested whereas geranyl diphosphate (GPP) was exclusively accepted as prenyl donor substrate. Further enzymatic characterization of bergaptol 5-*O*-geranyltransferase activity revealed some unique properties. Our findings provide valuable information for the discovery of a yet unidentified coumarin-specific prenyltransferase gene.

References

[1] Munakata, R., Inoue, T., Koeduka, T., Sasaki, K., Tsurumaru, Y., Sugiyama, A., Uto, Y., Hori, H., Azuma, J., Yazaki, K., “Characterization of coumarin-specific prenyltransferase activities in *Citrus limon* peel”, *Biosci. Biotech. Biochem.* 76(7), 1389-1393, 2012.

ABSTRACTS (MASTER THESIS)

Study on a Magnetron-based Microwave Power Transmission System for a Mars Observation Airplane

**(Graduate School of Engineering,
Laboratory of Applied Radio Engineering for Humanosphere, RISH, Kyoto University)**

Akihito Nagahama

Magnetron-based microwave power transmission system was studied for realization of a microwave-driven Mars observation airplane as shown in Figure 1. Both high-speed accurate beam direction control and controllability of the transmitting power are required for the system. First, a transmission system was suggested, which consists of a phased array with “power-variable phase-controlled magnetrons (PVPCMs)," a "received voltage lock loop (RVLL)” and a beam direction control system. Based on the system configuration, required specifications of phased array elements were estimated. The half power width of beam pattern should be more than 39.1 degrees when PVPCMs can vary their power from the peak to the half value. Second, auto beam direction control experiments were implemented in order to evaluate beam direction control performance of an experimental system. From experimental results, it was revealed that there were position detection errors up to − 15 degrees Necessity of proper position detection methods as well as accuracy improvement was described. Next, frequency asynchronous phenomena in an injected magnetron under step-wise power control were studied. Measuring transfer functions of the magnetron, it was revealed that frequency asynchronous is caused by an overshoot characteristic under the step-wise power control. Countermeasures by modifying a PLL in the PVPCM and increasing the input power of injected signal were proposed. were suggested. Although most of frequency asynchronous phenomena were suppressed in a magnetron output range of 432 W to 684 W with the input power of 4.5 W, frequency asynchronous with spiky phase variation could not be suppressed. Finally, an experimental RVLL was developed for feasibility experiments through transfer function measurements. The received voltage at a rectenna array was converged on the target voltage in 70 ms. Adoptability of the RVLL for the stable received power control was confirmed.

References

[1] A. Nagahama, T. Mitani, N. Shinohara, K. Fukuda, K. Hiraoka and K. Yonemoto, “Auto Tracking and Power Control Experiments of a Magnetron-based Phased Array Power Transmitting System for a Mars Observation Airplane”, IEEE MTT-S International Microwave Workshop Series on Innovative Wireless Power Transmission: Technologies, Systems, and Applications (IMWS-IWPT 2012), THU-A-3, Proceedings pp.29-32, Kyoto, Japan, May 10-11, 2012.

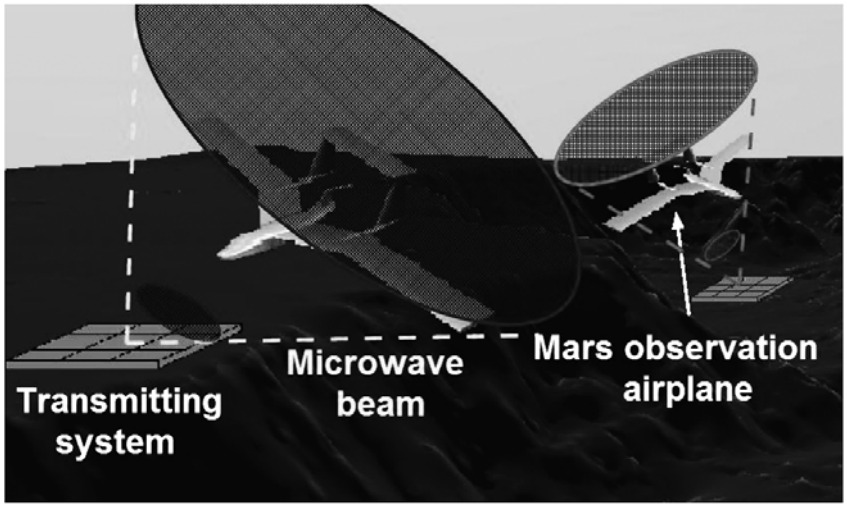

Figure 1. A conceptual image of a Mars observation system with microwave power supply.

ABSTRACTS (MASTER THESIS)

Optimal Design of High-Temperature Superconducting Coil for Magnetic Sail Spacecraft

(Graduate School of Engineering, Laboratory of Space Systems and Astronautics, RISH, Kyoto University)

Yoh Nagasaki

Magnetic sail is an innovative spacecraft propulsion system. The thrust of the sail is produced by the transfer of momentum from the solar wind, which is a plasma flow from the sun, to a strong magnetic field generated by a High Temperature Superconducting (HTS) coil installed in the spacecraft. Since a driving force of the magnetic sail is proportional to a magnetic moment (operational transport current × the area enclosed by the coil), the magnetic moment must be increased as large as possible. In this study, we perform an optimization study for the HTS coil in order to improve the thrust of the magnetic sail. We firstly developed an analysis method to predict the current transport performance and thermal behavior of HTS coils. We obtained the electric field versus current density as well as heat transfer characteristics of the Bi-2223/Ag tape from experiments using short length samples (30 mm length tape) at conduction cooling conditions. These characteristics of the HTS tape were modeled and analyzed by using the percolation depinning model and the two-dimensional heat balance equation. The percolation depinning model can describe the electric field versus current density of HTS tapes as a function of temperature and magnetic field vector. Next, we investigated the current transport and thermal characteristics of the Bi-2223/Ag double pancake coil. This scale-down model magnet was installed at a cold stage of a GM cryocooler. Only six pieces of aluminum sheets were attached symmetrically at both top and bottom surfaces of the magnet for cooling, taking into account the cooling constraint condition of the spacecraft system. We measured the temperature rises as well as its distribution of the magnet for various operation temperatures from 40 to 80 K, during current applications from 0 to 200 A. In addition, we analyzed the thermal behavior of the HTS magnet under the same conditions as the experiments, on the basis of the percolation depinning model and the three-dimensional heat balance equation. As a result, we showed that the analysis can successfully reproduce the experimental temperature traces for a wide range of operational temperature from 40 to 80 K, and that our analysis can estimate the exact quench currents of the HTS magnet. After developing an analysis method, we design an HTS coil to obtain a larger magnetic moment on the specific constraint conditions of a spacecraft system by using the developed analysis method. As a result, from a point of view of maximizing the magnetic moment for the spacecraft, the racetrack coil is the optimal configuration and the magnetic moment can be increased to 5.3 times larger than that of the former study. This study leads to the possibility of creating the world's first space propulsion system using an HTS coil.

References

[1] Y. Nagasaki, T. Nakamura, I. Funaki, Y. Ashida, and H. Yamakawa, "Conceptual Design of YBCO Coil With Large Magnetic Moment for Magnetic Sail Spacecraft," IEEE Trans. Appl. Supercond., 4603405, vol. 23, no. 3, 2013.

[2] Y. Nagasaki, T. Nakamura, I. Funaki, Y. Ashida, and H. Yamakawa, "Coupled-analysis of current transport performance and thermal behaviour of conduction-cooled Bi-2223/Ag double-pancake coil for magnetic sail spacecraft," Physica C, in press.

ABSTRACTS (MASTER THESIS)

Evaluation of strength performance of notched joint on Japanese traditional wooden structure

(Graduate School of Agriculture, Laboratory of Structural Function, RISH, Kyoto University)

Fumihiro Noda

Introduction

On renewing or retrofitting of traditional Japanese wooden structures, designers have to estimate the strength of whole structures to ensure the safety. Especially the earthquake proof property is the most important subject of structural design in earthquake prone country like Japan. Whole structure's strengths are greatly depends on the performance of each joints in the structure. Therefore designers want to calculate these joints correctly. But the evaluation method of strength of these important joint has not enough developed for traditional timber joints. Especially notched joints which is commonly seen in traditional joint has difficulty in prediction due to the influence of stress concentration around notch.

The purpose of this study is to provide a strength calculation formula, as much as precisely and easily, about the Japanese traditional wooden structure joint having a notch for designers or workers. We investigated "Kanawa-tsugi" and "Konehozo-siguti" in this research, and mention by focusing on "Kanawa-tsugi" in this summary.

Experiment

"Kanawa-tugi" is the longitudinal joint used in the connection of beam-to-beam or colum-to-column joint. It is known that the joint efficiency of Kanawa-tugi in terms of strength is one of the best among traditional joints. It is composed by same shaped member interlocked each other, and fixed by key driven at the center of the joint. In this study, the tensile test for the joint was carried out. The specimens with length of 240, 360 (2 types) and 480mm at joint part composed of 2 kinds of wood species (Japanese Cedar and Cypress) are used as shown in Fig.1. In order to verify the influence of load carrying capacity of notch, one type of specimen was composed without notch part and fixed just by horizontal dowels made of Shirakashi. 6 duplicates are made for each type of specimens. We conducted a static tensile loading examination and measured the relationship between tensile force and relative displacement of two members.

Results and discussion

Almost specimens showed brittle failure mode by shear in parallel to the grain direction originated from the corner of central notch. The strength of the joint become larger when the length of the joint is longer from 240mm to 260mm. However, tensile strength of the joint did not show proportional tendency when joint length become longer than 360mm. We assumed that couple moment concentrated around the notch and the moment influenced on the untimate shear strength of the joint. Thus we introduced a formula to predict the ultimate strength of the joint (Pub) considering this phenomenon. As a result, we could confirm that the estimated value (Pu=min[Pus,Pub]) is safer than test results. Then it is concluded that the formula is useful satisfactory.

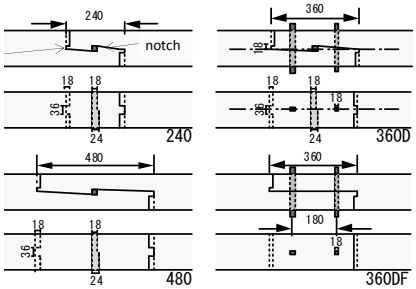

Fig.1 Examination body summary

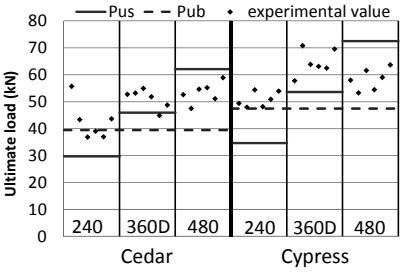

Fig.2 Test result and predicted value

ABSTRACTS (MASTER THESIS)

Evaluation of load carrying capacity on Japanese traditional timber joint with live oak fastener

**(Graduate School of Agriculture,
Laboratory of Structural Function, RISH, Kyoto University)**

Masashi Nomura

Introduction

Wood-to-wood joint is generally used on Japanese traditional timber buildings. Traditional timber buildings have been constructed based on empirical rules and craftsmanship of carpenters. In these days, scientific analysis of traditional timber joint requires a further progress. It is necessary to reveal a strength properties of the joints. This study discusses the three types of joint (Sya-chi-sen joint, Komi-sen joint and Hana-sen joint) for evaluation of their tensile performance. The final purpose is to propose a mechanical model. Furthermore, a material test was carried out in order to clarify the mechanical properties of live oak that have been used as a fastener.

Materials and Methods

Material test of live oak (test 1), tensile performance test of Sya-chi-sen joint (test 2) and tensile performance test of Komi-sen joint and Hana-sen joint (test 3) are discussed. Concerning test 1, its purpose was to investigate the influence of mechanical properties by the position among timber cross section, and to grasp the appropriate allowable strength. Test 2 joint specimens was composed of beam and column (Sugi), spline (Hinoki) and inclined shear key connector (live Oak). Joints of 12types was used by changing size of parts which were assumed to affect on joint strength. 3 specimens for each parameter was employed (6 specimens for control). As for test 3, The specimen is consisted of column of hinoki, spline of hinoki and dowel connector of live oak. Pull out force was applied until failure of the joint in Test 2 and 3.

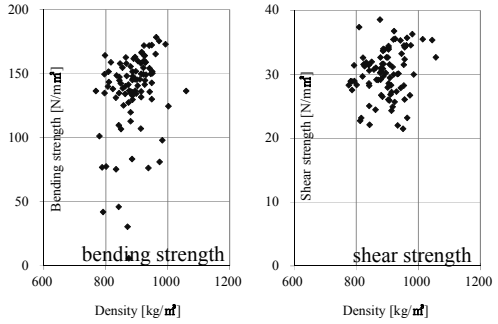

Figure 1. Results of test 1.

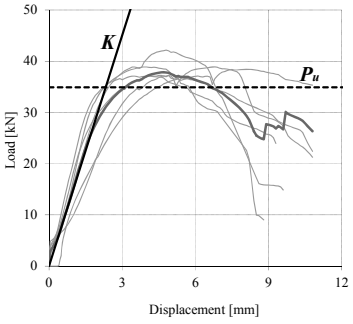

Figure 2. Results of test 2.

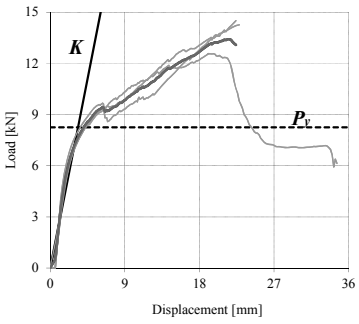

Figure 3. Results of test 3.

Results and Discussion

Figure 1, as examples, shows the relationship between the bending-shear strength and density of live oak. Consequently, it was found that result of each specimen distributed irrespective of annual ring orientation and the correlation to position was small. Furthermore, the influence of defect was remarkable on bending strength but not so significant on shear strength. Concerning test 2, many specimens caused split failure as a result of rotation of Sya-chi-sen. Thus equations to estimate the maximum strength (P_u) were proposed with consideration of splitting failure. Figure 2 shows the test result and calculated values of initial stiffness (K) and P_u. Calculated maximum strength was rather lower than test results, however, initial stiffness corresponded properly. As for test 3, bending- shear crack of key connector were observed as failure mode in most specimens. Meanwhile, in relationship between load and displacement, load succesively increased until maximum load even after yield point. As figure 3 shows, calculated characteristic values suggested by equations for dowel type fastner corresponded properly to test result.

ABSTRACTS (MASTER THESIS)

Study on the Variability Characteristics of Precipitable Water Vapor Associated with Heavy Rainfall Using a Non-hydrostatic Model

**(Graduate School of Science,
Laboratory of Atmospheric Sensing and Diagnosis, RISH, Kyoto University)**

Masanori Oigawa

Introduction

GPS Precipitable Water Vapor (PWV) is useful to monitor water vapor variations associated with heavy rainfall. The Geospatial Information Authority of Japan is operating a nationwide GPS network, called GPS Earth Observation Network System (GEONET) with a mean horizontal spacing of about 20 km. PWV from GEONET has already been used for operational mesoscale analysis of Japan Meteorological Agency (JMA). However, water vapor fluctuations ahead of the initiation of deep convection occur at meso-γ scale (2-20 km) (Shoji, 2013). Higher horizontal resolution (1-2 km) PWV observations have been performed by using a dense GPS network installed near Uji campus of Kyoto University (Sato et al., 2013). For the accurate forecast of local heavy rainfall, it is important to observe PWV at meso-γ scale and assimilate the high resolution PWV data into a cloud resolving model.

Method

In this study, an analysis was performed about meso-γ scale water vapor fluctuations associated with a heavy rainfall to verify the feasibility of high resolution PWV data assimilation, using JMA non-hydrostatic model (JMA-NHM) and PWV data observed by the hyper-dense GPS network in Uji. In order to reproduce small scale water vapor distributions, high resolution numerical simulations were performed using JMA-NHM with grid intervals of 250 m. The torrential rainfall event was reproduced which occurred on 14 August 2012 around the dense GPS network.

Result

In the 250 m forecast, PWV values started to increase 9 minutes before starting to rain within the area of about 10 × 5 km^2. At the same time, humid boundary layer grew thick in this area because of the wind convergence near the surface (Fig.1). Similarly, increasing of PWV value 10 minutes ahead of rainfall was also observed by the GPS receiver at Uji campus. These results suggest that PWV fluctuations cloud be a precursor of heavy rainfall and that the forecast accuracy of local heavy rainfall could be improved by assimilating high resolution PWV data into a cloud resolving model.

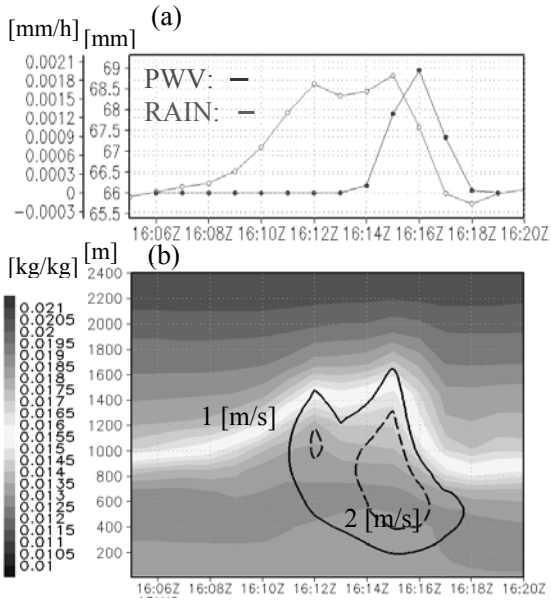

Figure 1. (a) Time variation of PWV and Rain at a certain point in NHM and (b) Time-height cross section of water vapor mixing ratio (shade) and vertical wind velocity (contour) at the same point in NHM.

References

[1] Shoji Y., "Retrieval of Water Vapor Inhomogeneity Using the Japanese Nationwide GPS Array and its Potential for Prediction of Convective Precipitation," *J. Meter. Soc. Japan*, 91, pp.43-62, 2013.

[2] Sato K., E. Realini, T. Tsuda, M. Oigawa, Y. Iwaki, Y. Shoji, H. Seko, "A High-Resolution Precipitable Water Vapor Monitoring System Using a Dense Network of GNSS Receivers," *Journal of Disaster Research*, 8(1), pp. 37-47, 2013.

ABSTRACTS (MASTER THESIS)

Study of strength of timber joints with inclined screws and its application on structure

**(Graduate School of Agriculture,
Laboratory of Structural Function, RISH, Kyoto University)**

Kazuhiro Osugi

Materials and Methods

The purpose of this study is to predict the ultimate load and the initial stiffness of timber-to-concrete joints using self-tapping threaded connectors driven into wood with inclined angles. Element test was carried out using 7types self –tapping screws with continuous threads. Test setup is shown in Figure1. Screws of 90mm in length were driven at the interface between the side (plywood 28mm) and middle (Japanese cedar 105mm square) wood member. 7types of inclination angle of screw against load direction were set (-45° to 45°). 0° is the control specimen in which screw was driven vertically to load direction. T type specimens is subjected to the tension force together with shear force due to the inclination angle. And on C type specimens screw was tapped with inclination anlge so that compression force is applied (see Figure2). To eliminate the influence of friction between members a Teflon sheet was placed at boundary of wood components.

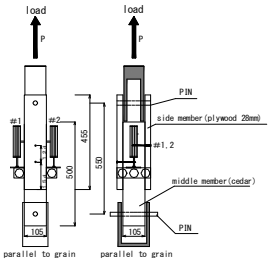

Figure 1. Tensile test setup

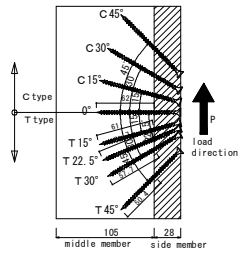

Figure 2. Inclination angle of screws

Results and Discussion

The load-deformation curves obtained in the tests are shown in Figure3 and Figure4. For the screws with an angle of T30° between the screw axis and the force direction, the load-carrying capacities was larger than the value for screws loaded perpendicular to the fastener axis. Due to the decrease of embedment length of the screws in the middle wood member with increasing angle, the load-carrying capacity for the timber-to-timber connections with an angle above T45°become smaller. Also a remarkable point is the steady rise of the initial stiffness with increasing angle between the screw axis and the grain direction in T type fasteners. The dependency of the connection stiffness on the angle between the screw axis and the force direction can be seen in Figure3. In comparison to the timber-to-timber connections with screws loaded perpendicular to their axis, the connection with T45°screws reached almost 20 times higher connection stiffness than that of usual 0° screws. On the other hand, C types did not show a remarkable improvement on load-carrying capacities or the initial stiffness due to side wood member moved apart from middle member according to loading from early timing. (see in Figure4)

As expected, the connection failure was caused by reaching the withdrawal and bending capacity of the screw and the timber embedding strength. The strength value is a total of resistance force derived from those components. Timber-to-timber connections with fasteners loaded perpendicular to their axis failed due to a combined embedding/ bending failure. With increasing angle between the screw axis and the grain direction, the ratio of withdrawal component against strength became greater.

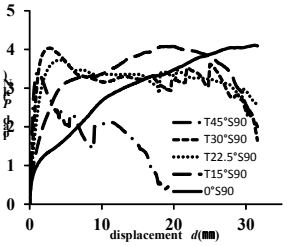

Figure 3. Load- deformation curves of T type specimens

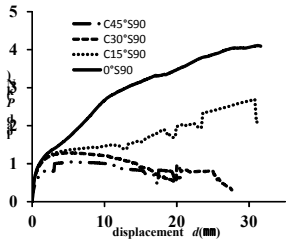

Figure 4. Load- deformation curves of C type specimens

ABSTRACTS (MASTER THESIS)

Analysis of two MATE-type transporters expressing in *Lotus japonicus*

**(Graduate School of Agriculture,
Laboratory of Plant Gene Expression, RISH, Kyoto University)**

Yoshihiro Ota

Nitrogen is an essential nutrient which circulates in the ecosystem by changing its chemical form. Rhizobia are soil-born bacteria that form nodules on the roots of leguminous plants such as soybean and *Lotus japonicus*. These symbiotic bacteria are involved in symbiotic nitrogen fixation which fixes atmospheric N_2. Upon the infection of rhizobia into legume roots, legume-*Rhizobium* symbioses is established, and in mature nodules many metabolites such as carbon source and amino acids and inorganic ions are transported between rhizobia and host plants; however, most of transporters involved in this process remain to be clarified.

In order to analyze transporter genes expressed in nodule comprehensively, LM (laser micro-dissection) coupled with microarray analysis was performed, where we found that yet uncharacterized Multidrug and toxic compound extrusion (MATE) transporter, LjMATE2 (chr2.LjT36E17.20.r2.d) and LjMATE3 (chr2.CM0008.1100.r2.d) belonging to were preferentially expressed in outer parts of nodule (uninfected cells).

MATE type transporter was first identified in bacteria as a transporter exporting broad range of xenobiotics. MATE type transporters have in general 9-12 putative transmembrane regions, and use electrochemical gradient to transport substrates in plant cells. Many plant MATE transporters identified to date show high substrate specificity for particular endogenous compounds such as alkaloids, flavonoids and citric acids. In this study, I have analyzed the expression profiles of both *LjMATE2* and *LjMATE3* to elucidate their functions in the mature nodules.

In order to analyze the tissue specific expression of *LjMATE2* and *LjMATE3*, reverse transcription polymerase chain reaction (RT-PCR) analysis was performed using cDNA from flowers, leaves, anthocyanin-accumulating stems, uninfected roots, infected roots and nodules of wild type *Lotus japonicus* (Gifu) , as well as the stems of wild type *L. japonicus* (Miyakojima) for comparison between anthocyanin accumulation in stems. The expression of *LjMATE2* was high in anthocyanin-accumulating stems, whereas *LjMATE3* expression was detected throughout the plant including nodules. LjMATE2 was also shown to be localized at the vacuolar membrane in plant cells, using the analysis of GFP-tagged protein.

To analyze the expression of *LjMATE3* in nodule more in detail, quantitative real-time PCR was also performed. The real-time PCR analysis revealed that *LjMATE3* expression was increased during the nodulation, and the expression level of *LjMATE3* in 26 day-old nodules was approximately five times higher than that of roots before infection. The expression of *LjMATE3* was also induced by glutathione treatment in the similar pattern as genes involved in flavonoid synthesis. Promoter: GUS transformants of *Lotus japonicus* showed that the expression of LjMATE3 in mature nodules was restricted to fibro vascular bundle of nodules.

From these analyses, it was suggested that LjMATE2 functions as anthocyanin transporter mainly in the stem, while LjMATE3 function could be a transporter involved in flavonoid accumulation in nodules.

ABSTRACTS (MASTER THESIS)

Analysis of two transporters, LjSWEET4 and LjALMT, in nodules of *Lotus japonicus*

**(Graduate School of Agriculture,
Laboratory of Plant Gene Expression, RISH, Kyoto University)**

Yuka Saida

Symbiotic nitrogen fixation in legume plants takes place in nodules, specialized organs formed in roots. In infected cells of nodules, *Rhizobium* exists in forms of bacteroids that are capable of reducing atmospheric N_2 to NH_3, thereby supplying the fixed nitrogen to the host plant. In turn, host legume plant cells provide photosynthetic metabolites mainly in forms of dicarboxylates. Inorganic compounds are also required for the function of bacteroid and are transported across the membrane in nodule. In this process, various types of transporters should be involved at different membrane systems in nodules; however, at the molecular level there remain little insights on the flow of carbon source from the plant cells to the symbiotic bacteria. In this study, I analyzed a putative sugar transporter expressed in nodules of *Lotus japonicus* in order to characterize the molecular mechanism of carbon source transport to bacteroids. To identify the genes possibly involved in sugar transporter in nodules, we focused on the gene homologs of a recently identified sugar transporter family (AtSWEET) in *Arabidopsis* and an aluminum-activated malate transporter (ALMT) family member. In this abstract, results on LjSWEET is described.

AtSWEET1 was shown to be an efflux transporter of monosaccharides such as glucose. In BLAST search on genomic database of *L. japonicus*, at least 13 homologs of *AtSWEET* exist in the genome of *L. japonicas*. We performed semi-quantitative reverse transcription polymerase chain reaction (RT-PCR) with cDNA samples of the roots, nodules and leaves. It was found that only *LjSWEET4* is highly expressed in the nodule.

Real-time quantitative PCR analysis revealed that the *LjSWEET4* expression level in the nodule was approximately 10 and 3 times higher than those of the leaves and the root tissue, respectively. We also performed time course expression analysis of *LjSWEET4* in the underground plants with real-time PCR. It was revealed that the expression of *LjSWEET4* slowly increased after infection of *Mesorhizobium loti* up to 3 weeks of infection.

We also investigated the cell-type specificity of the *LjSWEET4* expression using *L. japonicus* nodules transformed with β-glucuronidase (GUS) reporter gene under the control of *LjSWEET4* promoter, i.e., 2 kb upstream genomic region of *LjSWEET4*. Whole mount analysis of the transgenic plants showed strong and specific activity of GUS in the vascular systems both in roots and nodules. LjSWEET4-GFP fusion protein expressed in *Coptis japonica* protoplasts showed that LjSWEET4 was located at the plasma membrane. These results suggest that LjSWEET4 functions as a transporter in the movement of metabolites from the root to the infected zone of nodules.

ABSTRACTS (MASTER THESIS)

Biological and Chemical Characteristics of the Aged Wood with a Special Reference to the Radial Location

(Graduate School of Agriculture, Laboratory of Innovative Humano-Habitability, RISH, Kyoto University)

Rikiya Takesako

Introduction

It is well known that wood in service changes its mechanical and chemical properties. The major causes of these changes are biological deterioration, weathering and natural aging. Many studies have been carried out regarding the former two causes, but there are little studies about the nature of the aged wood. In addition, some beetles are known to prefer the aged wood as their host, and the volatile compounds seem to play a major role in detecting the host wood.

In this study, laboratory tests were conducted to know the biological performance of the aged wood, and its chemical characteristics were also surveyed.

Materials and Methods

Sapwood of two aged and one new timbers of *Pinus thunbergii* were used as samples. For the aged timbers, test specimens were taken from three sampling points (1^{st}: near to surface, 2^{nd}: middle part of sapwood, and 3^{rd}: near to heartwood) in the radial direction.

Termite and fungi tests were carried out according to the Japan Industrial Standard (JIS) K-1571(2010). Volatile compounds from the samples were captured by Monotrap®, and extractives were obtained with dichloromethane by the help of the ultrasonic treatment. They were served for the GC-MS analyses.

Results and Discussion

Mass losses due to biological attacks in the aged wood samples generally were higher than those in the new wood samples, and the higher values were obtained from the samples which are closer to the heartwood. These results suggest that the wood surface, being received the most severe aging effects, has the highest biological resistance against termite and fungi.

By the GC-MS analyses, longifolene (RT: 14.235 min) was detected in both the volatile and dichloromethane extract in all the samples. α-pinene (RT: 5.107 min) was present only in the new wood samples. On the contrary, longicamphenylone (RT: 14.205 min) was found only in the dichloromethane extract in the aged samples. These three chemicals have been reported as essential oil components of *P. thunbergii*. It has also been reported that longicamphenylone can be obtained by oxidization of longifolene. Therefore, it is likely that longicamphenylone which is produced during the natural aging from longifolene, plays an important role in biological resistance of the aged *P. thunbergii* wood.

From these results, it is probable that conversion of some chemical components into the higher bio-active compounds can have a role for the biological performance of the aged wood.

Acknowledgement

The author would like to express his greatest thanks to Dr. Nobuhiro Shimizu, Kyoto Gakuen University, for his helps in the GC-MS analyses. The author also thankful to Prof. Junji Sugiyama, RISH, Kyoto University, for identification of the aged wood samples.

ABSTRACTS (MASTER THESIS)

Development of Wood-based Molding bonded with Tannin and Sucrose

**(Graduate School of Agriculture,
Laboratory of Sustainable materials, RISH, Kyoto University)**

Akinori Takeyama

Introduction

Recently, synthetic adhesives derived from fossil resources are used in many wood-based materials. However, considering the finite fossil resources, it is desirable to replace natural-based adhesives based on non-fossil resources. Condensed tannin has been used as a main raw material for tannin-based adhesives. Conventional tannin-based adhesives are usually synthesized by reacted with compounds derived from fossil resources such as formaldehyde. It is beneficial to develop a tannin-based adhesive composed of only natural materials derived from bio-resources. In this research, sucrose was used as a raw material for a tannin based adhesive. The physical properties of wood-based molding bonded with the tannin adehsive were investigated.

Materials and Methods

Wood powder of *Acacia mangium*, tannin and sucrose were used in this research. Powder size of materials was 60 mesh pass (under 250μm). Dried raw materials were added to a beaker, and shaken sufficiently by hand. Mixture of powder was added to dies, and pressed to yield molded products by hot press. The mixture ratios of tannin and sucrose were 100:0, 75:25, 50:50, 25:75 and 0:100. The contents of adhesive were 0~40wt%. Three-point bending and repeated boiling tests were performed to evaluate physical and mechanical properties of the molded products.

Results and discussion

Figure 1 shows the relationship between the adhesive content and bending properties under the mixing ratio of 50:50 with tannin and sucrose. The bending properties were increased with increasing of adhesive content, and modulus of rupture (MOR) of 33.3wt% adhesive content was 39MPa. In addition, this molding had good water resistance. Consequently, there is a possibility that a mixture of tannin and sucrose can be used as a natural adhesive for wood-based molding.

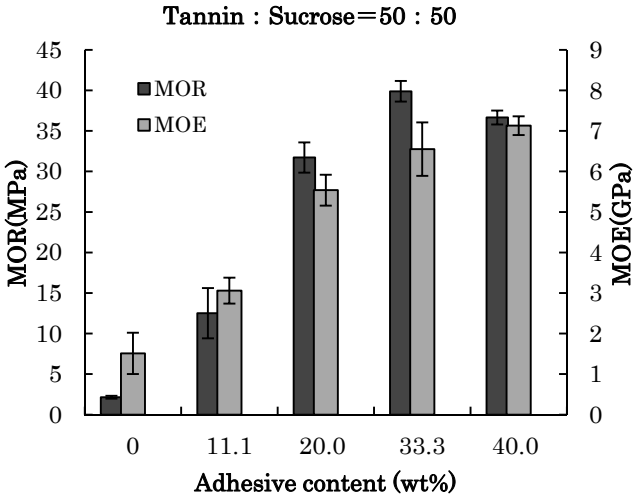

Fig1. Effects of adhesive content on bending properties
Molded at 200°C, 4MPa, for 10minutes

ABSTRACTS (MASTER THESIS)

Biochemical analysis of flavonoid secretion in soybean

**(Graduate School of Agriculture,
Laboratory of Plant Gene Expression, RISH, Kyoto University)**

Kazuaki Yamashita

Legume plants such as soybean (*Glycine max*), pea (*Pisum sativum*) and kidney bean (*Phaseolus vulgaris*) are cultivated as important grains in 12-15% agricultural land in the world. Legume plants establish symbiosis with soil bacteria collectively called rhizobium to fix the atmospheric nitrogen. The first event of this symbiotic process is the secretion of signaling molecules (e.g., flavonoids) from roots, which activate the transcription factor, nodD, of rhizboium leading to the nodule formation. Genistein, daidzein, and coumestrol have been so far identified as signaling molecules in soybean. The transport activity of isoflavonoid aglycon (e.g. genistein) has been analyzed using membrane vesicles of soybean roots, and ATP-dependent isoflavone-specific transport has been reported (Sugiyama et al., 2007).

Root exudates of soybean also contain flavonoid glycosides such as malonyldaidzin and malonylgenistin , whereas β-glucosidase for flavonoid malonyl glycoside occurs at apoplast, suggesting the existence of efflux mechanisms for flavonoid malonyl glycoside at plasma membrane of soybean roots. However, no transporter genes mediating the secretion of flavonoids, regardless of aglycons or glycosides, have been identified thus far. The aim of this study is the identification of flavonoid transporters in soybean roots in order to gain the molecular mechanism of signal molecule movements on the onset of symbiosis.

Analysis of root exudates during soybean growth was carried out, in which hydroponic medium was subjected to high performance liquid chromatography (HPLC) analysis. A large amount of flavonoid derivatives are highly secreted to the medium under the –N condition, in particular daidzein and 6’’-*O*-malonyldaidzin were detected as the main flavonoids, in which daidzein decreased and 6’’-*O*-malonyldaidzin increased during the growth of soybean.

To understand the transport mechanisms of 6’’-*O*-malonyldaidzin in soybean roots, transport activity measurement using plasma membrane vesicle and vacuole membrane vesicle from soybean root were performed, but no activities were found. These studies suggest that yet uncharacterized transport mechanisms may function in the secretion of malonylated flavonoids.

References

[1] Sugiyama, A., Shitan, N. and Yazaki, K., “Involvement of a soybean ATP-binding cassette-type transporter in the secretion of genistein, a signal flavonoid in legume-Rhizobium symbiosis.”, *Plant Physiology*, 144., 2000-2008, 2007.

ABSTRACTS (MASTER THESIS)

Test Particle Simulation of Relativistic Electron Microbursts Induced by EMIC Waves in the Earth's Radiation Belts

**(Graduate School of Engineering,
Laboratory of Computer Simulation for Humanospheric Sciences,
RISH, Kyoto University)**

Qinghua Zhao

We have performed test particle simulations to demonstrate that relativistic electron microbursts are induced by electromagnetic ion cyclotron (EMIC) triggered emissions. Pitch-angle scattering of relativistic electrons arising from the anomalous cyclotron resonance with left-hand polarized EMIC waves contributes to the sharp decrease of the relativistic electron flux in the outer radiation belt in the main phase of magnetic-storms. EMIC triggered emissions with frequencies typically increasing in time are generated in the equatorial region and propagate along the magnetic field line both northward and southward. First, by the simulation with simplified EMIC model, we check if electrons are scattered in pitch angles. We perform test particle simulations to reproduce the time histories of pitch angles, trajectories in the (θ-ξ) phase space, distribution of the resonant electrons assuming an EMIC wave with a varying frequency as observed by Cluster spacecraft. We find that the efficiency of pitch-angle scattering depends on the frequency sweep rate, the gradient of the magnetic field, and the wave amplitude. The most effective pitch-angle scattering takes place for the case of a rising-tone emission with an enhanced magnetic field gradient. Then we reproduce the EMIC triggered emission based on the chorus equations and wave equations. We trace a large number of electrons and record the numbers of electrons precipitated into the loss cone. Due to the short bounce time of the electrons compared to EMIC propagation time, the electrons after adiabatic bounce motion at the mirror points interact with another wave packet near the equator and are scattered into the loss cone. We find that EMIC triggered emissions are very effective in precipitating the relativistic electrons for a wide range of energy and pitch angles from the radiation belts, causing the relativistic microbursts.

NOTES

Cloning and expression analysis of a cDNA encoding an oxaloacetate acetylhydrolase from the brown-rot fungus *Fomitopsis palustris*

Hiromichi Hisamori[1], Tomoki Watanabe[1,2], Shiro Suzuki[1], Kumiko Okawa[1], Haruko Sakai[3], Tsuyoshi Yoshimura[4], Toshiaki Umezawa[1,5] and Takefumi Hattori[1,6,*]

[1] Laboratory of Metabolic Science of Forest Plants and Microorganisms, RISH, Kyoto University
[2] Present address: TAKARA BIO INC.
[3] Nara Forest Research Institute
[4] Laboratory of Innovative Humano-habitability, RISH, Kyoto University
[5] Institute of Sustainability Science, Kyoto University
[6] Present address: Institute of Socio-Arts and Sciences, The University of Tokushima
[*]Corresponding author. E-mail: thattori@ias.tokushima-u.ac.jp

ABSTRACT

The brown-rot fungus *Fomitopsis palustris* possess two oxalate-producing enzymes: oxaloacetate acetylhydrolase (*Fomitopsis palustris* oxaloacetate acetylhydrolase, FpOAH), which catalyzes hydrolysis of oxaloacetate, and cytochrome *c* dependent glyoxylate dehydrogenase (*Fomitopsis palustris* glyoxylate dehydrogenase, FpGLOXDH), which catalyzes dehydrogenation of glyoxylate. Oxaloacetate was regarded as the predominant precursor for oxalate, because greater FpOAH activity was detected than FpGLOXDH activity. In this study, a 1080-bp cDNA encoding FpOAH was cloned. Recombinant FpOAH showed oxaloacetate acetylhydrolase (OAH, EC 3.7.1.1) activity, which confirmed that the isolated cDNA encoded FpOAH. Expression of the gene encoding FpOAH was 22.0-140.8 times greater than that encoding FpGLOXDH, depending on culture times. The gene expression results support our proposed idea that FpOAH plays more significant role than FpGLOXDH in oxalate biosynthesis in *F. palustris*.

INTRODUCTION

Wood-rotting basidiomycetes cause severe damage to wooden structures. Oxalic acid produced from the wood-rotting fungi has several important roles in this degradation. For example, the acid hydrolyzes hemicelluloses, which increase the accessibility of decaying enzymes or low-molecular-weight decay agents to wood components [1]. During cellulose degradation by the Fenton reaction, a low concentration of oxalate promotes degradation [2] by increasing hydroxyl radical formation [3]; however, a higher concentration of the acid inhibits degradation [2] and radical formation [3]. Furthermore, oxalate forms Fe-oxalate complexes, which then diffuse into the wood cell wall, by which oxalate protects the hyphae of brown-rot fungi from attack by the Fenton reagent [4-6].

Therefore, to protect woody structures from the degradation caused by wood-rotting fungi, mechanisms of oxalate biosynthesis should be elucidated. We investigated oxalate biosynthesis in the brown-rot fungus *Fomitopsis palustris*, because the fungus accumulates large amounts of oxalic acid (33-78 mM) during liquid cultivation [7]. *F. palustris* has two metabolic pathways for oxalate biosynthesis. One is the hydrolysis of oxaloacetate catalyzed by oxaloacetate acetylhydrolase (*Fomitopsis palustris* oxaloacetate acetylhydrolase, FpOAH) [8]. The other is dehydrogenation of glyoxylate catalyzed by cytochrome *c* dependent glyoxylate dehydrogenase (*Fomitopsis palustris* glyoxylate dehydrogenase, FpGLOXDH) [9].

Oxaloacetate is regarded as the major precursor for oxalate, because greater FpOAH activity has been detected than FpGLOXDH activity [7]. However, oxalate production in *F. palustris* has not been investigated in terms of the expressions of genes involved in oxalate biosynthesis. Tang et al. [10] identified a putative gene encoding oxaloacetate acetylhydrolase (OAH, EC 3.7.1.1) in the genome of the brown-rot basidiomycetous fungus *Fibroporia radiculosa* (*Antrodia radiculosa*); however, the gene

NOTES

product has not been shown to be an OAH with activity. Thus, a gene encoding OAH (*OAH*) has not been identified from basidiomycetes, although several *OAHs* have been identified from ascomycetes, including *Aspergillus niger* [11], *Botrytis cinerea* [12] and *Penicillium chrysogenum* [13].

The present study reports the isolation of a cDNA encoding FpOAH and a comparison of the transcript abundances of the FpOAH and FpGLOXDH genes. The results suggest that FpOAH has a greater role in oxalate biosynthesis in the brown-rot fungus *F. palustris*.

MATERIALS AND METHOD

Cloning of a cDNA encoding FpOAH

Partial cDNA fragments were amplified by PCR, which was performed in a 20-µl reaction mixture containing 0.43 U Blend Taq polymerase (TOYOBO), 5 mM each of primers F1 and R1 (Fig. 1), and 10 ng of a cDNA library prepared previously using mRNA from *F. palustris* [14]. Primers F1 and R1 were designated using the nucleotide sequence of *oahA* (encoding oxaloacetate acetylhydrolase) from *A. niger* (AJ567910) and fgenesh1_pg.C_scaffold_1200340 encoding a putative isocitrate lyase / phosphorylmutase (JGI protein ID 7156) from *Phanerochaete chrysosporium*. The PCR cycle protocol was as follows: 94°C for 2 min; 35 cycles at 94°C for 1 min, 60°C for 1 min, and 72°C for 1 min; and 72°C for 3 min. To determine both ends of the cDNA sequence, 5'- and 3'-rapid amplification of cDNA ends (RACE) was conducted with the primers shown in Fig. 1 (for 5'-RACE, F2 and Gene specific Primer R2; for 3'-RACE, R3 and Gene specific Primer F3) using the Gene Racer kit (Invitrogen), according to the manufacturer's instructions. The amplified cDNA fragments were subcloned into the TA cloning vector using the pCR2 TOPO TA cloning kit (Invitrogen). A clone containing an insert of the expected size was sequenced. The open reading frame (ORF) of the cDNA was cloned with the PCR primers F4 and R4, containing *Nde* I and *Not* I restriction enzyme sites, respectively (Fig. 1). Using primers F4 and R4, and a cDNA library as a template[14], PCR was performed in a 50-µl reaction mixture containing 2.5 U Blend Taq polymerase, 10 µM each primer and 10 ng the template. The PCR cycle protocol was as follows: 94°C for 2 min; 30 cycles at 94°C for 1 min, 55°C for 1 min, and 72°C for 1 min; and 72°C for 10 min.

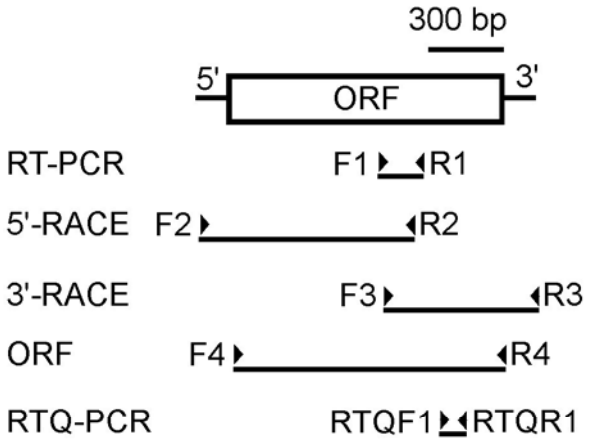

Primer	Sequence
F1	5' -AGCAGGTCGTCTCSCGCGAG-3'
R1	5' -CGATGAARCMMACRTCCGCKCC-3'
F2	5' -CGACTGGAGCACGAGGACACTGA-3'
R2	5' -GCGGCGAGCTTCAGGCGGGTGAC-3'
F3	5' -GCTGTCATTGCCCGCGACTCGATCC-3'
R3	5' -GTGTCAACGATACGCTACGTAACG-3'
F4	5' -CATATGCCGGGTTTCGAATTCACT-3'
R4	5' -GTGCGGCCGCGACCTGAGCAAAGGC -3'
RTQF1	5' -TCGTCAACGTCATCTCCGGT-3'
RTQR1	5' -GCACCATCGCAACGCAA-3'

Fig. 1 Locations and nucleotide sequences of PCR primers used for cloning the cDNA encoding the oxaloacetate acetylhydrolase of *Fomitopsis palustris* (*Fomitopsis palustris* oxaloacetate acetylhydrolase, FpOAH). Arrowheads represent the primers, and underlines between them indicate the cDNA fragments amplified with these primers.

Preparation and Purification of recombinant FpOAH

The ORF of the cDNA was subcloned into pET-23a vector (Novagen) at *Nde* I and *Not* I sites. The plasmid, hereafter named FpOAH-pET-23a, was transformed into *Escherichia coli* BL21 (DE3) competent cells (Novagen). The transformed cells were grown at 37°C with shaking at 250 rpm in LB broth

containing 50 μg/ml ampicillin. When the OD600 of the culture reached 0.4-0.6, isopropyl β-D-thiogalactopyranoside was added to the culture at 0.4 mM to induce recombinant protein expression. The culture was further incubated for 12.5 h at 20°C at 250 rpm. The cells were harvested by centrifugation (2000 ×*g*) for 10 min at 4°C. The cell pellet was suspended in lysis buffer [2 mM Tris-HCl (pH 7.5), 10 mM dithiothreitol, 1 mM phenylmethylsulfonyl fluoride]. The suspension was sonicated at amplitude 20 for 5 seconds with a Sonicator S-4000 (Misonix), and centrifuged at 4°C for 10 min at 10000 ×*g*. The supernatant was loaded onto a His-Bind resin (Novagen) column equilibrated with a binding buffer, according to the manufacturer's protocol. The column was washed with 6 ml of binding buffer and 8 ml of wash buffer, and then eluted with 5 ml of elute buffer. The fraction containing the target recombinant protein was passed through a Sephadex G-25 column. The desalted recombinant protein was assayed immediately.

Enzyme assay for recombinant FpOAH

FpOAH activity of the recombinant protein was determined by the method of Akamatsu et al. [15], with a slight modification. Briefly, the enzyme reaction mixture (1.0 ml), containing 40 mM imidazole buffer (pH 7.6), 1.0 mM oxaloacetate, 1.0 mM manganese chloride, and 100 μl crude enzyme solution, was incubated at 30°C for 2 h. Oxalate was then extracted from the reaction mixture with ethyl acetate. To quantify oxalate, electron-impact mode GC-MS was performed on a Shimadzu GC-MS QP-2010, column: CBP1-M25-025, 25m×0.22mm, column temperature: 80-240°C (8°C /min), carrier gas: He, linear velocity: 50 cm/sec. Selected ion monitoring was carried out for quantification of oxalate at *m/z* 261.10.

Analysis of the FpOAH cDNA

A BLASTp search was carried out on the JGI website (http://genome.jgi-psf.org/) using the protein sequence deduced from the cDNA as the query. A neighbor-joining tree was generated using the CLC sequence viewer program. Identity and similarity were calculated using BioEdit, in which similarity matrix is BLOSUM62.

F. palustris *growth conditions*

The culture was initiated and grown as previously reported, with a slight modification [7]. Briefly, mycelia on a slant or plate culture maintained at 4°C on potato dextrose agar (PDA) medium were inoculated onto a PDA plate using an inoculating loop. Fungal inocula were cut from a colony grown on the agar plate with a cork borer (6 mm in diameter). Five plugs of mycelia were grown in 200-ml Erlenmeyer flasks with 40 ml of liquid medium containing 0.8 % (w/v) peptone, 0.05 % (w/v) KH_2PO_4, 0.05 % K_2HPO_4, 0.03 % $MgSO_4 \cdot 7H_2O$, 5 ppm thiamine HCl and 2% (w/v) glucose.

Real-time quantitative PCR analysis of FpOAH *and* FpGLOXDH *transcription*

Total RNA was isolated at different time points from *F. palustris* mycelia using RNeasy Plant Mini Kit (Qiagen), according to the manufacturer's protocol. After DNase treatment with RQ1 RNase-Free DNase (Promega), total RNA (0.3 μg) was applied to first-strand cDNA synthesis using Superscript II reverse transcriptase (Invitrogen). Real-time quantitative PCR was performed using a 7300 Real Time system (Applied Biosystems). Power SYBR Green PCR Master Mix (Applied Biosystems) was used to detect amplicons. Quantification of the amplicons was based on standard curves prepared using pET-23a(+) plasmids harboring *FpOAH* and *FpGLOXDH* [16]. The gene specific primers, RTQF1 and RTQR1 (Fig. 1), were used to generate a 111bp amplicon for FpOAH transcripts. The gene specific primers, RTQF2 (5'-TGGTTCAAGAGCATCACGAAGAT-3') and RTQR2 (5'-CGAGAGAACGATTCCCTGCA-3'), were used to generate a 105bp amplicon for *FpGLOXDH* transcripts. The amount of transcripts was normalized by comparison with those of a 75-bp-amplicon derived from 28S rRNA (GenBank Accession number. AY 515333) using sense primer 5'-TGACACGGACTACCAGTGCTTT-3' and antisense primer 5'-CACCCATTTTGAGCTGCATTC-3' [17].

NOTES

RESULTS AND DISCUSSION

Characterization of the FpOAH cDNA

We isolated a cDNA (1080 bp, GenBank accession no. AB690578) encoding a deduced 38212-Da protein. To determine whether the cDNA encodes FpOAH, the OAH activity of the recombinant protein was assayed. GC-MS analyses showed that a significant amount of oxalate (9.25 μmol/ mg recombinant protein) was produced during a 2-h reaction. By contrast, no oxalate was detected from the control cultures (Table 1). The results clearly showed that the isolated cDNA encodes FpOAH.

Table 1. Quantification of oxalate produced in enzymatic reaction.

Assay system		Oxalate produced (μmol/mg recombinant enzyme·2h)
Complete		9.25
Control 1	(denatured enzyme) *1	0
Control 2	(without substrate)	0
Control 3	(without enzyme)	0

*1 The denatured enzyme was prepared by heating the sample at 100°C for 30 min.

Blastp analysis showed that the deduced FpOAH belonged to the isocitrate lyase/PEP mutase enzyme superfamily. Joosten et al. [17] proposed that the active site serine in isocitrate lyase/PEP mutase enzyme superfamily is conserved. As in the case of other enzymes of this family, the deduced FpOAH was found to have an active site serine (data not shown).

We characterized the deduced FpOAH in comparison with deduced OAHs from other microorganisms. *OAHs* have been cloned from ascomycetes: *oahA* (accession number AJ567910), *OAHA* (accession number AY590264), and PC22g28430 (accession number XM_002566325) from *A. niger* [11], *B. cinerea* [12] and *P. chrysogenum* [13], respectively. The deduced FpOAH shared 40%, 39%, and 39% identities and 55%, 54%, and 55% similarities with oahA, OAHA, and PC22g28430, respectively.

To determine whether homologous proteins of FpOAH are encoded in the genomes of other wood-rotting fungi that have been reported to produce oxalate [19-25], a BLASTp search was conducted against the genomes of these fungi listed in the JGI website. Deduced homologous proteins with the lowest e-values for each wood-rotting fungus were chosen. It is important to note that there had been no reports showing OAH activities of these proteins and they were not annotated as OAHs. All e-values of chosen proteins were 0.0. A neighbor-joining tree for these homologous deduced proteins from the wood-rotting fungi and oahA, OAHA and PC22g28430 is shown in Fig. 2. The results show that FpOAH and estExt_fgenesh1_pg.C_230033 from *Fomitopsis pinicola* are the most closely related proteins, which is not surprising as they both belong to the same genus. The deduced proteins from white- and brown-rot fungi listed in Fig. 2 were not strictly separated into different clades by their decay type, i.e. brown- or white-rot. Further discussion of the phylogenetic relationships of these FpOAH homologs should await determination of their OAH activities.

Changes in expressions of genes encoding oxalate-biosynthesis enzymes of F. palustris during cultivation

We compared the expressions of the two genes, *FpOAH* and *FpGLOXDH*. The amounts of *FpOAH* transcript were 22.0 times greater on day 4 (minimal magnitude) and 140.8 times greater on day 9 (maximal magnitude) compared with those of FpGLOXDH (Table 2). Munir et al. [7] strongly suggested that FpOAH is the major enzyme responsible for the production of oxalate, based on the greater activity of FpOAH compared with that of FpGLOXDH. The greater expression of *FpOAH* compared with FpGLOXDH supports this proposed idea [7].

NOTES

With regard to changes in the amounts of *FpOAH* transcripts during cultivation, significant amounts of *FpOAH* transcripts were detected on day 2 (37.2 copy number/pg total RNA). The amount of the transcript decreased gradually to 19.1 copy number/pg total RNA until day 6. This change was likely to be consistent with changes in the specific activity for FpOAH during a similar cultivation period [7]. However, the greatest amount of transcript, 103.7 copy number/pg total RNA, was observed on day 9, which was not consistent with the changes in specific activity of FpOAH [7]. Further research is needed to elucidate reasons underlying this contradiction.

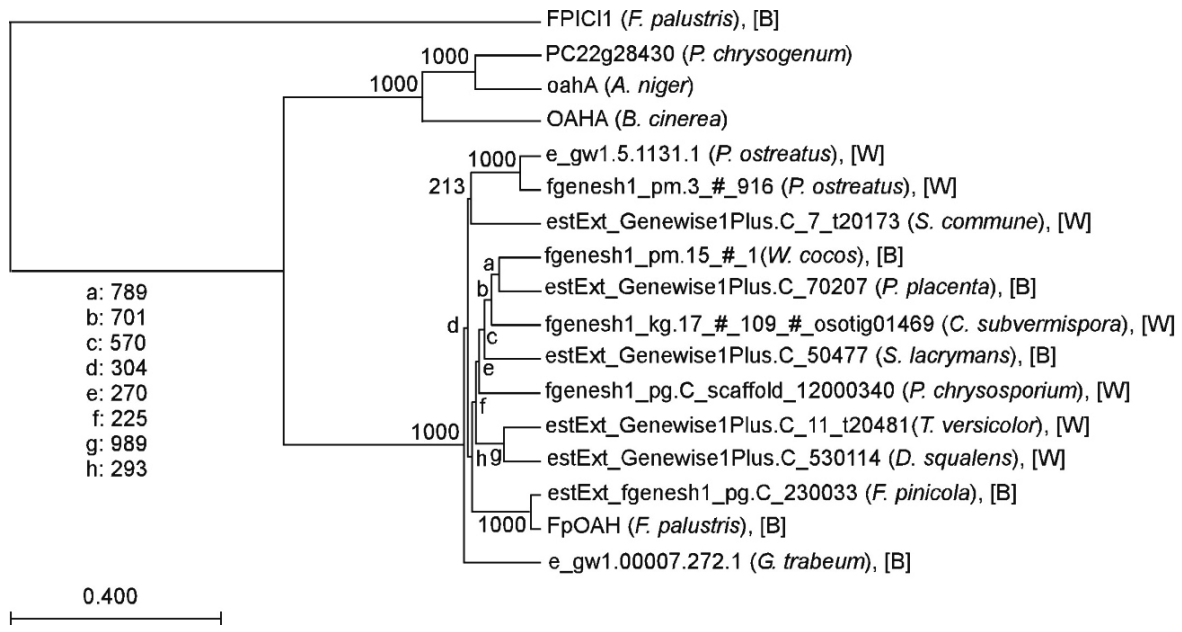

Fig. 2. Phylogenetic tree of FpOAH with identified OAHs from *A. niger*, *B. cinerea* and *P. chrysogenum*, and putative FpOAH homologs from wood-rotting fungi.

Numbers at the branch nodes are bootstrap values (per 1000 trials). The scale bar represents 0.400 substitutions per amino acid position. Deduced proteins from brown- and white-rot fungi are marked with [B] and [W], respectively. PC22g28430, an oxaloacetate acetylhydrolase of *P. chrysogenum* (NCBI accession no. XM_002566325); oahA, an oxaloacetate acetylhydrolase of *A. niger* (NCBI accession no. AJ567910); OAHA, an oxaloacetate acetylhydrolase of *B. cinerea* (NCBI accession no. AY590264); e_gw1.5.131.1, an FpOAH homolog from *Pleurotus ostreatus* v2.0 (JGI protein ID 29565; e_gw1.5.131.1); fgenesh1_pm.3_#_916, an FpOAH homolog from *P. ostreatus* v1.0 (JGI protein ID 95096; fgenesh1_pm.3_#_916); estExt_Genewise1Plus.C_7_t20173, an FpOAH homolog from *Schizophyllum commune* (JGI protein ID 105238; estExt_Genewise1Plus.C_7_t20173); fgenesh1_pm.15_#_1, an FpOAH homolog from *Wolfiporia cocos* (JGI protein ID 92053; fgenesh1_pm.15_#_1); estExt_Genewise1Plus.C_70207, an FpOAH homolog from *Postia placenta* (JGI protein ID 112832; estExt_Genewise1Plus.C_70207); fgenesh1_kg.17_#_109_#_isotig01469, an FpOAH homolog from *Ceriporiopsis subvermispora* (JGI protein ID 87490; fgenesh1_kg.17_#_109_#_isotig01469); estExt_Genewise1Plus.C_50477, an FpOAH homolog from *Serpula lacrymans* (JGI protein ID 105238; estExt_Genewise1Plus.C_50477); fgenesh1_pg.C_scaffold_12000340, an FpOAH homolog from *Phanerochaete chrysosporium* (JGI protein ID 7156; fgenesh1_pg.C_scaffold_12000340); estExt_Genewise1Plus.C_11_t20481, an FpOAH homolog from *Trametes versicolor* (JGI protein ID

NOTES

173629; estExt_Genewise1Plus.C_11_t20481); estExt_Genewise1Plus.C_530114, an FpOAH homolog from *Dichomitus squalens* (JGI protein ID 111644; estExt_Genewise1Plus.C_530114); estExt_fgenesh1_pg.C_230033, an FpOAH homolog from *F. pinicola* (JGI protein ID 155899; estExt_fgenesh1_pg.C_230033); FpOAH, an oxaloacetate acetylhydrolase of *F. palustris* (DDBJ, accession no. AB690578); e_gw1.00007.272.1, an FpOAH homolog from *Gloeophyllum trabeum* (JGI protein ID 42369; e_gw1.00007.272.1); FPICL1, one of the members of the ICL/PERM_KPHMT enzyme superfamily in *F. palustris* (DDBJ, accession no. AB079254 [27]) is shown as an outgroup.

F. palustris acquires energy for growth by oxidizing glucose, mainly to oxalate, through the tricarboxylic acid (TCA) and glyoxylate (GLOX) cycles [7, 26, 27]. The greater expression of *FpOAH* compared with *FpGLOXDH* supports the proposed idea that oxalate is biosynthesized mainly in the cytosol by FpOAH but not in the peroxisome by FpGLOXDH [7, 27]. To protect FpOAH from possible inhibition by oxalate, an oxalic acid resistance system, including FpTRP26 [17], and oxalate transport out of the cell, involving FpOAR [14], probably have important roles in maintaining carbon metabolism in *F. palustris.*

Table 1. Expressions of *FpOAH* and *FpGLOXDH* during growth.

Culture time (day)	2	4	6	9	12	15
FpOAH mRNA (copy number/pg total RNA)	37.2 ± 7.2	28.8 ± 4.4	19.1 ± 6.4	103.7 ± 2.5	26.7 ± 6.3	48.4 ± 11.2
FpGLOXDH mRNA (copy number/pg total RNA)	0.7 ± 0.2	1.3 ± 0.2	0.3 ± 0.1	0.7 ± 0.2	0.4 ± 0.1	1.6 ± 0.3

Values are means ± standard error, n=5, technical replicates=2

The insignificant expression of FpGLOXDH compared to FpOAH suggests that 1) leaking of glyoxylate from the GLOX cycle for oxalate production is not significant; and 2) inhibition of isocitrate lyase and malate synthase by oxalate [28, 29], two key enzymes GLOX cycle, might not be essential. Accordingly, the results support the proposed idea that the metabolic flow of the GLOX cycle is probably sufficient to support the TCA cycle.

By contrast, Tang et al. [10] recently suggested that the brown-rot fungi *F. radiculosa* and *P. placenta* produce oxalate mainly from glyoxylate by glyoxylate dehydrogenase (GLOXDH), based on the greater number of genes encoding GLOXDH than OAH in the two fungi. Therefore, there may be fungal species-dependent variation in oxalate biosynthesis in terms of which precursor, oxaloacetate or glyoxylate, is dominant for oxalate production in basidiomycetes. The characterization of the isolated cDNA encoding FpOAH contributes to the determination of oxalate biosynthesis in wood-rotting fungi.

Acknowledgments

This research was partly support by a Grant-in Aid for Scientific Research from the Japan Society for the Promotion of Science (no. 23580455) and by a grant-in-aid from the Development and Assessment of Sustainable Humanosphere (DASH) / Forest Biomass Analytical System (FBAS) (23DF-12).

References

[1] Green III, F., Larsen, M. J., Winandy, J. E., and Highley, T. L. (1991) “Role of oxalic acid in incipient brown-rot decay”, *Mater. Org.* 26:191-213.

NOTES

[2] Tanaka, N., Akamatsu, Y., Hattori, T., and Shimada, M. (1994) "Effect of oxalic acid on the oxidative break down of cellulose by the Fenton reaction", *Wood Res.* 81:8-10.

[3] Varela, E. and Tien, M. (2003) "Effect of pH and oxalate on hydroquinone-derived hydroxyl radical formation during brown rot wood degradation", *Appl. Environ. Microbiol.* 69: 6025-6031.

[4] Arantes, V., Qian, Y., Milagres, A. M. F., Jellison, J. and Goodell, B. (2009) "Effect of pH and oxalic acid on the reduction of Fe^{3+} by a biomimetic chelator and on Fe^{3+} desorption/adsorption onto wood: Implications for brown-rot decay", *International Biodeterioration and Biodegradation* 63:478-483.

[5] Hyde, S.M., and Wood, P.M. (1997) "A mechanism for production of hydroxyl radicals by the brown-rot fungus *Coniophora puteana*: Fe(III) reduction by cellobiose dehydrogenase and Fe(II) oxidation at a distance from the hyphae", *Microbiology* 143: 259-266.

[6] Shimada, M., Akamatsu, Y., Tokimatsu, T., Mii, K., and Hattori, T. (1997) "Possible biochemical roles of oxalic acid as a low molecular weight compound involved in brown-rot and white-rot wood decays", *J. Biotechnol*. 53:103-113.

[7] Munir, E., Yoon, J. J., Tokimatsu, T., Hattori, T., and Shimada, M. (2001) "A physiological role for oxalic acid biosynthesis in the wood-rotting basidiomycete *Fomitopsis palustris*", *Proc. Natl. Acad. Sci. USA* 98:11126-11130.

[8] Akamatsu, Y., Ohta, A., Takahashi, M., and Shimada, M. (1991) "Enzymatic formation of oxalate from oxaloacetate with cell-free-extracts of the brown-rot fungus *Tyromyces palustris* in relation to the biodegradation of cellulose", *Mokuzai Gakkaishi* 37:575-577.

[9] Tokimatsu, T., Nagai, Y., Hattori, T., and Shimada, M. (1998) "Purification and characteristics of a novel cytochrome *c* dependent glyoxylate dehydrogenase from a wood-destroying fungus *Tyromyces palustris*", *FEBS Letters* 437:117-121.

[10] Tang, J.D., Perkins, A.D., Sonstegard, T.S., Schroeder, S.G., Burgess, S.C. and Diehl, S.V. (2012) "Short-read sequencing for genomic analysis of the brown rot fungus *Fibroporia radiculosa*", *Appl. and Environ. Microbiol.* 78: 2272-2281.

[11] Pedersen, H., Hjort, C., Nielsen, J. (2000) "Cloning and characterization of *oah*, the gene encoding oxaloacetate hydrolase in *Aspergillus niger*", *Mol. Gen. Genet*. 263: 281-286.

[12] Han, Y., Joosten, H. J., Niu, W., Zhao, Z., Mariano, P. S., McCalman, M. T., van Kan, J. A. L. , Schaap, P. J. and Dunaway-mariano, D. (2007) "Oxaloacetate hydrolase, the C-C bond lyase of oxalate secreting fungi", *J. Biol. Chem.* 282: 9581-9590.

[13] Gombert, A. K., Veiga, T., Puig-Martinez, M., Lamboo, F., Nijland, J. G., Driessen, A.J.M., Pronk, J.T., and Daran, J. M. (2011) "Functional characterization of the oxaloacetase encoding gene and elimination of oxalate formation in the β-lactam producer *Penicillium chrysogenum*", *Fungal Genetics and Biology*, 48: 831-839.

[14] Watanabe, T., Shitan, N., Suzuki, S., Umezawa, T., Shimada, M., Yazaki, K. and Hattori, T. (2010) "Oxalate transporter from the brown-rot fungus *Fomitopsis palustris*", *Appl. and Environ. Microbiol*., 76: 7683-7690.

[15] Akamatsu, Y., Takahashi, M. and Shimada, M. (1992) "Cell-fee extraction and assay of oxaloacetase from the brown-rot fungus *Tyomyces palustris*", *Mokuzai Gakkaishi*, 38: 495-500.

[16] Hattori, T., Okawa, K., Fujimura, M., Mizoguchi, M., Watanabe, T., Tokimatsu, T., Inui, H., Baba, K., Suzuki, S., Umezawa, T., and Shimda, M. (2007) "Subcellular localization of the oxalic acid-producing enzyme, cytochrome *c*-dependent glyoxylate dehydrogenase in brown-rot fungus *Fomitopsis palustris*", *Cellullose Chemistry and Technology*, 41: 545-553.

NOTES

[17] Watanabe, T., Shitan, N., Umezawa, T., Yazaki, K., Shimada, M. and Hattori. T. (2007) "Involvement of FpTRP26, a thioredoxin-related protein, in oxalic acid-resistance of the brown-rot fungus *Fomitopsis palustris*", *FEBS Letters*, 581: 1788-1792.

[18] Joosten, H. J., Han, Y., Niu, W., Vervoort, J., Dunaway-Mariano, D., and Schaap, P. J. (2008) "Identification of fungal oxaloacetate hydrolyase within the isocitrate lyase/PEP mutase enzyme superfamily using a sequence marker-based method", *Proteins* 70: 157-166.

[19] Akamatsu, Y., and Shimada, M. (1994) "Partial purification and characterization of glyoxylate oxidase from the brown-rot basidiomycete *Tyromyces palustris*", *Phytochemistry* 37: 649-653.

[20] Dutton, M.V., Evans, C.S., Atkey, P.T., and Wood, D.A. (1993) "Oxalate production by basidiomycetes, including the white-rot species *Coriolus versicolor* and *Phanerochaete chrysosporium", Appl. Microbiol. Biotechnol*. 39: 5-10.

[21] Green III, F., and Clausen, C.A., (2005) "Copper tolerance of brown-rot fungi: oxalic acid production in southern pine treated with arsenic-free preservatives", *International Biodeterioration and Biodegradation*, 56: 75-79.

[22] Hastrup, A.C.S., Jensen, B., Clausen C., and Green, F. (2006) "The effect of CaCl2 on growth rate, wood decay and oxalic acid accumulation in *Serpula lacrymans* and related brown-rot fungi", *Holzforschung* 60: 339-345.

[23] Mäkelä, M., Galkin, S., Hatakka, A., and Lundell, T. (2002) "Production of organic acids and oxalate decarboxylase in lignin-degrading white rot fungi", *Enzyme and Microbial Technology* 30: 542-549.

[24] Takao, S. (1965) "Organic acid production by basidiomycetes", *Appl. Microbiol*. 13: 732-737.

[25] Watanabe, T., Hattori, T., Tengku, S., and Shimada, M. (2005) "Purification and characterization of NAD-dependent formate dehydrogenase from the white-rot fungus *Ceriporiopsis subvermispora* and a possible role of the enzyme in oxalate metabolism", *Enzyme and Microbial Technology* 37: 68-75.

[26] Munir, E., Yoon, J. J., Tokimatsu, T., Hattori, T. and Shimada, M. (2001) "New role for glyoxylate cycle enzymes in wood-rotting basidiomycetes in relation to biosynthesis of oxalic acid", J. Wood Sci. 47: 368-373.

[27] Sakai, S., Nishide, T., Munir, E., Baba, K., Inui, H., Nakano, Y., Hattori, T. and Shimada. M. (2006) "Subcellular localization of glyoxylate cycle key enzymes involved in oxalate biosynthesis of wood-destroying basidiomycete *Fomitopsis palustris* grown on glucose", *Microbiology*, 152: 1857-1866.

[28] Munir, E., Hattori, T., and Shimada, M. (2002) "Purification and characterization of isocitrate lyase from the wood-destroying basidiomycete *Fomitopsis palustris* grown on glucose", *Arch. Biochem. Biophys*., 399: 225-231.

[29] Munir, E., Hattori, T., and Shimada, M. (2002) "Purification and characterization of malate synthase from the glucose-grown wood-rotting basidiomycete *Fomitopsis palustris", Biosci. Biotechnol. Biochem.* 66: 576-581.

NOTES

Project in Sikkim (India), September 1st 2012 – April 30th 2013 as visiting Professor at RISH *Sugi* in the Sikkim Himalayas

(CRCAO, Centre de recherché sur les civilisations d'Asie orientale - CNRS UMR 8155/ Associated member)

Mechtild Mertz

During my mission in Sikkim from November 4 to December 1st, 2012 "**Wood Selection of Ancient Temple Structures in the Sikkim Himalayas"** I collected wood samples from different temples. From the first day on I was surprised to see trees looking like *sugi*, the Japanese cedar tree, growing along the roadside in the capital Gangtok and in the countryside. They are regarded as ornamental trees (figure 1). Thanks to the publications Rai and Rai (1994) as well as Cowan and Cowan (1929), I realized that the Japanese cedar has a long history in Sikkim and other parts of India.

Figure 1. Branch of a *sugi* tree, *Cryptomeria japonica*, near Namchi, South Sikkim, located in an altitude of 1,700 m.

The Japanese cedar was introduced to India in 1865 by Robert Fortune (1812-1880), a Scottish plant collector in China and Japan, and extensively planted since 1891. Fortune was trained at the Royal Botanic Garden, Edinburgh, before moving south to the (Royal) Horticultural Society Garden at Chiswick (London). Following the 1842 Treaty of Nanking (Nanjing) and the opening up of trade with China, Fortune was selected on the society's behalf to journey to China collecting plants. For three years from 1845 he visited the treaty ports along the coast purchasing material from gardens and nurseries. Subsequently he undertook two further expeditions on behalf of the Honourable East India Company collecting seed and tea plants which helped lay the foundation of the Indian tea industry. His fourth and last journey (1860–62) was mainly to Japan where he collected among other plants *Cryptomeria japonica* (Oxford Index). Hoping to introduce this tree also to Scotland or England, he named this tree a Japanese cedar, as the term "cedar" refers to a conifer tree yielding highly esteemed timber. The European climate was not suitable for it, but in Northern India, notably in Daarjeeling he found that the tree could well adapt to the climate, as well as to Sikkim, where this tree can be found all over, even as high as in an altitude of 2,900 m (Figure 2).

NOTES

Figure 2. A Japanese cedar tree next to the Mani Lakhang prayer-wheel temple in Lachen, Sikkim, at 2,900 m elevation.

This tree was introduced as a timber tree to make tea boxes in Darjeeling and Sikkim. In fact, both areas form the Sikkim Himalaya from a geographical, geological and botanical perspective (Rai and Rai, p. 9) and they yield excellent tea, although only Darjeeling-tea has worldwide renown. When traveling through South Sikkim, on my way from Gangtok to Namchi, I came across tea fields (Figure 3). And in Gangtok numerous tea shops offer various qualities of black tea from Sikkim and Darjeeling.

The cedar tree in Sikkim is growing fast, even faster than that in Japan, and easily reaches a height of 30 m. Its wood is described as soft, light and fragrant. It is also insect-proof. The tree can grow in altitudes from 900-2,100 m, but it thrives best from 1,200-1,800 m (Cowan and Cowan, p. 143).

I was told by local people that the custom of making tea boxes from the *dhupi* tree, the local Nepalese name of *sugi*, was abandoned, because the tea was permeated by the smell of the wood. Back in Kyoto, I interviewed the owner of the Araki-Ikkyūen tea shop in the Nishijin area to understand, whether Japanese tea boxes are eventually made of *sugi*. In fact, the Japanese also use, and still today, *sugi* for tea boxes.

NOTES

However, in Japan the inside of the box is lined by a layer of tin, to keep the tea dry, and so that the smell of the wood cannot permeate the tea leaves.

Figure 3. On a trip from Gangtok to Namchi (South Sikkim) I came across this tea field, just under flowering Himalayan cherry trees (in November!), *Prunus cerasoides*, and *dhupi* trees, *Cryptomeria japonica*. *Dhupi* is the Nepalese name for *sugi*.

Figure 4. A tea box made of *sugi*, belonging to the Araki-Ikkyūen tea shop, Omiya-Kuramaguchi (Kamigyo-ku), Kyoto.

Figure 5. Inside of the tea box, lined with zinc

NOTES

It was really surprising to witness the history, impact and ramification of various aspects of Japanese tea-making process in the Sikkim Himalayas.

	Scientific	English	Nepali
Names	*Cryptomeria japonica*	Japanese cedar	dhupi tarpin

REFERENCES

[1] Cowan A.M. and Cowan J.M. *The Trees of Northern Bengal: Including Shrubs, Woody Climbers, Bamboos, Palms and Tree Ferns.* Bengal: Secretariat Book Depot, 178 p., 1929.

[2] Oxford Index. Oxford University Press

http://oxfordindex.oup.com/view/10.1093/oi/authority.20110803095830205 [accessed April 25, 2013]

[3] Rai T. and Rai L. *Trees of the Sikkim Himalaya*. New Delhi: Indus Publishing Company. 120 p., 1994.